

Design, Synthesis and Evaluation of Liquid-like Nanoparticle Organic Hybrid Materials (NOHMs) for Carbon Dioxide Capture

Kun-Yi Lin

Submitted in partial fulfillment of the
requirements for the degree of
Doctor of Philosophy
in the Graduate School of Arts and Science

COLUMBIA UNIVERSITY

2012

© 2012

Kun-Yi Lin

All Rights Reserved

ABSTRACT

Design, Synthesis and Evaluation of Liquid-like Nanoparticle Organic Hybrid Materials (NOHMs) for Carbon Dioxide Capture

Kun-Yi Lin

Given the rapid increase in atmospheric concentration of CO₂, the development of efficient CO₂ capture technologies is critical for the future of carbon-based energy. Currently, the most commonly employed approach to capture CO₂ is amine scrubbing in which amine-based solvents react with gaseous CO₂ to form carbamate. Although the amine-based solvents such as monoethanolamine (MEA) exhibit high CO₂ capture capacity, their high volatility results in corrosive fumes and energy-intensive regeneration process. Therefore, there is an urgent need to develop alternative CO₂ capture media that can be efficient and environmentally sustainable.

To achieve this goal, a new class of CO₂ capture media named Nanoparticle Organic Hybrid Materials (NOHMs) has been formulated. A unit of NOHMs consists of a surface-functionalized nanoparticle as a core to which selected polymers are tethered to form a canopy. Such a configuration prevents loss of polymers and enables NOHMs to exhibit near zero vapor pressure. As the canopy is tethered to the core, it has been theorized that CO₂ can be captured not only by the enthalpic effect via reactions with functional groups along the polymeric canopy but also by the entropic means via introduction of small gaseous molecules such as CO₂ to reduce the free energy of the frustrated canopy.

This study represents the first attempt to investigate CO₂ capture using NOHMs. In this dissertation, NOHMs were designed, synthesized and evaluated for CO₂ capture properties. Characterization of NOHMs was conducted by employing various spectroscopic tools, such as ATR FT-IR, Raman and NMR, to confirm successful synthesis of NOHMs. Thermal stability

and nanoscale configuration of NOHMs were measured using TGA and TEM, respectively. NOHMs with various chemical and structural parameters, including bonding types, functional groups, chain lengths, core sizes, and core fractions, were prepared. The effects of these parameters on CO₂ capture relevant properties such as thermal stability, thermally-induced swelling, CO₂-induced swelling, CO₂ packing behavior and CO₂ capture capacity were explored in detail.

In comparison to the unbound polymers, NOHMs exhibited enhanced thermal stability. Such an enhancement allows NOHMs to be used in a wide-range of operational temperatures. While an unbound polymer degraded 80 wt% after a 100-cycle temperature swing, there was no significant loss in its corresponding NOHMs. Elevated temperatures also caused NOHMs to swell but the degree of thermally-induced swelling of NOHMs was less than that of the unbound polymers due to restriction on movement of the tethered polymer chains.

CO₂ capture capacity studies revealed that NOHMs can capture 0.1 – 0.4 mmol/g-solvent depending on partial pressure of CO₂ and temperatures. The CO₂ capture mechanism was also revealed as a Lewis acid-base interaction between CO₂ and ether groups which were the most common functional groups of the polymers selected for the NOHMs synthesis (e.g. NOHM-I-HPE, NOHM-I-tPE and NOHM-I-PEG). The effect of functional groups on CO₂ capture was far more significant. When amines were incorporated in NOHMs (e.g. 2.2 mmol/g-solvent in NOHM-I-PEI), as expected, the presence of amines enhanced CO₂ capture capacity.

While the enthalpic effect was pronounced, the entropic effect from NOHMs' unique structural nature would allow CO₂ to be captured more effectively. In order to explore the entropic effect, NOHMs were synthesized to minimize the enthalpic effect for the most of

structural studies, such as studies of CO₂-induced swelling and interaction of CO₂ with the canopy.

For the CO₂-induced swelling behavior, NOHMs exhibited notably less swelling than the unbound polymers at a given CO₂ capture capacity. NOHMs comprised of shorter polymer chains exhibited even less swelling than NOHMs having longer polymer chains at a given CO₂ capture capacity. This may be due to conformational differences between NOHMs and the unbound polymers which allow more CO₂ molecules to pack within polymer chains. Such conformational differences were further pronounced by lowering the grafting densities in NOHMs. These differences were attributed to specific structural configuration of a NOHMs' canopy in which polymer chains were tethered onto inorganic nanoparticle cores causing more "rigid" arrangements than in a bulk polymer.

In order to facilitate the implementation of NOHMs for CO₂ capture, several aspects were also investigated, including impact of SO₂, viscosity of NOHMs and CO₂ diffusivity in NOHMs. It was found that no significant amount of SO₂ was captured in NOHMs at low concentration (200 ppm of SO₂ in N₂), while a considerable amount of SO₂ was captured by NOHMs at 3010 ppm of SO₂ in N₂. As N₂ is almost insoluble in NOHMs, NOHMs showed a high selectivity toward SO₂ capture over N₂ capture. This behavior enables NOHMs to be a potential candidate for SO₂ removal. About 10 – 30% of CO₂ capture capacity was reduced after NOHMs exposed to SO₂ due to unavailability of some capture sites in NOHMs, which were occupied by SO₂. The result of the simultaneous removal of CO₂ and SO₂ showed that at low SO₂ concentration, NOHMs did not exhibit a noticeable selectivity toward SO₂ over CO₂. CO₂ capture capacity and CO₂-induced swelling were also measured with a mixture of CO₂/SO₂ to explore the effect of SO₂ on CO₂-induced swelling and packing behaviors of NOHMs. Similar swelling behaviors

were observed under pressurization with CO₂/SO₂ and pure CO₂ at low pressures. However, swelling behaviors of two cases deviated at higher pressures. This may be attributed to the distinct packing patterns in NOHMs under the pressurization with CO₂/SO₂ compared to the pressurization with pure CO₂.

The viscosity and CO₂ diffusivity in NOHMs with various structural parameters were also measured. The effect of core size was not pronounced on viscosity and CO₂ diffusivity as the core fraction was fixed. In contrast, a higher core fraction in NOHMs resulted in a significantly higher viscosity and a lower CO₂ diffusivity. The effect of temperature was also notable on CO₂ diffusion in NOHMs. However, a higher temperature can have a negative impact on the CO₂ capture capacity of NOHMs. To obtain an improved CO₂ diffusivity for CO₂ capture, the optimal operation temperature ranging from 40 to 70 °C was determined.

Finally, if the viscosity of NOHMs could be appropriately lowered by manipulating core sizes and core fractions at an optimal operation temperature, fluid NOHMs could be used in a spraying tower to capture CO₂. For relatively viscous NOHMs, such as amine functionalized NOHMs, a supported liquid membrane system could be used by coating or filling NOHMs inside the membrane to increase contact area for CO₂ capture. NOHMs could also be even functionalized to serve as dual-purpose smart materials for CO₂ capture and photocatalytic conversion of CO₂ to alcohols. A significantly amount of energy could be saved from solvent regeneration and the product would improve the process economics.

In summary, NOHMs were designed and synthesized to investigate the effects of chemical and structural parameters on key factors affecting CO₂ capture, including thermal stability, thermally-induced swelling, CO₂-induced swelling, CO₂ packing behavior, selectivity, viscosity and CO₂ diffusivity. The fundamental knowledge gained in this study not only became a basis

for the optimal design of NOHMs for CO₂ capture but also provided important information on how to design nanoscale hybrid materials for other advanced environmental and energy technologies.

Table of Contents

CHAPTER 1

INTRODUCTION	1
--------------------	---

CHAPTER 2

BACKGROUND AND MOTIVATION	7
2.1 Solvents for CO ₂ Capture	7
2.1.1 CO ₂ Capture using Conventional Ionic Liquids	8
2.1.2 CO ₂ Capture using Task-Specific Ionic Liquids	12
2.1.3 CO ₂ Capture using Binding Organic Liquids and Reversible Ionic Liquids.....	15
2.2 Nanoparticle Organic Hybrid Materials (NOHMs)	16
2.3 Research Objectives	17

CHAPTER 3

DESIGN AND SYNTHESIS OF NANOPARTICLE ORGANIC HYBRID MATERIALS (NOHMs)	28
3.1 Synthesis and Characterization of NOHMs	29
3.1.1 Classification of NOHMs	29
3.1.2 Synthesis Methods	29
3.1.3 Physical and Chemical Characterizations of NOHMs	30
3.2 Structural Analysis of NOHMs	31
3.3 POSS-based Nanoparticle Organic Hybrid Materials	36
3.3.1 Synthesis of POSS-based NOHMs	37
3.3.2 Characterization of POSS-based NOHMs	38

CHAPTER 4

EFFECTS OF CHEMICAL AND STRUCTURAL PARAMETERS ON THERMAL STABILITY OF NOHMs	57
4.1 Introduction	58
4.2 Experimental	59
4.2.1 Synthesis of NOHMs and Ionized PEG	59
4.2.2 Thermal Stability Analysis and Thermally-Induced Swelling	59
4.3 Results and Discussion	60
4.3.1 Characterization of NOHMs and Ionized PEG	60

4.3.2 Effects of Chemical and Structural Parameters on Thermal Stability.....	61
4.3.3 Effect of the Surface-Modified Nanoparticles.....	62
4.3.4 Long-Term Thermal Stability.....	66
4.3.5 Thermally-Induced Swelling of NOHMs	67
4.4 Conclusions	68
CHAPTER 5	
EFFECTS OF STRUCTURAL PARAMETERS ON CO ₂ CAPTURE CAPACITY, CO ₂ - INDUCED AND PACKING BEHAVIORS OF NOHMs	79
5.1 Introduction	80
5.2 Experimental	81
5.2.1 Synthesis of NOHMs and Ionized PEG	81
5.2.2 CO ₂ Capture Capacity and CO ₂ -induced Swelling Behavior	82
5.2.3 Raman Spectroscopy	82
5.3 Results and discussion.....	83
5.3.1 Effect of Chain Length on CO ₂ Capture Capacity	83
5.3.2 Effect of Chain Length on CO ₂ -induced Swelling	84
5.3.3 Effect of Grafting Density on CO ₂ Capture Capacity	87
5.4 Conclusions	97
CHAPTER 6	
EFFECTS OF BONDING TYPES AND FUNCTIONAL GROUPS OF NOHMs ON CO ₂ CAPTURE	117
6.1 Introduction	118
6.2 Experimental	118
6.2.1 Chemicals	118
6.2.2 Synthesis of NOHMs via Ionic Bond (NOHM-I-HPE, NOHM-I-tPE and NOHM-I-PEI)	119
6.2.3 CO ₂ Capture using NOHMs	120
6.3 Results and Discussion.....	121
6.3.1 Characterization of NOHMs.....	121
6.3.2 Thermal Stabilities of NOHMs.....	121
6.3.3 Effects of Temperature and Pressure on CO ₂ Capture using NOHMs.....	123
6.3.4 Absorption Selectivity of Gases in NOHMs	124

6.3.5 Recyclability of NOHMs during CO ₂ Capture and Solvent Regeneration Cycles.....	125
6.4 Conclusions	127
6.3.6 Effects of Ether and Amine Groups on CO ₂ Capture using NOHMs	126
CHAPTER 7	
EFFECT OF SULFUR DIOXIDE (SO ₂) ON CO ₂ CAPTURE USING NOHMs.....	142
7.1 Introduction	143
7.2 Experimental	143
7.2.1 Preparation of NOHMs.....	143
7.2.2 Characterization.....	144
7.2.3 CO ₂ Capture using NOHMs	144
7.2.4 Breakthrough experiments of CO ₂ and SO ₂	145
7.2.5 Attenuated Total Reflectance (ATR) FT-IR Spectroscopy	145
7.3 Results and Discussion.....	146
7.3.1 Characterization of Synthesized NOHMs	146
7.3.2 Sorption of N ₂ , Pre-humidified N ₂ , SO ₂ and CO ₂ in NOHMs.....	146
7.3.3 Effect of SO ₂ Exposure on CO ₂ Capture Capacity of NOHMs.....	147
7.3.4 Effect of SO ₂ on CO ₂ -induced Swelling and Packing Behaviors.....	150
7.4 Conclusions	152
CHAPTER 8	
VISCOSITY AND CO ₂ DIFFUSIVITY IN NOHMs AND POTENTIAL REACTOR DESIGN	164
8.1 Introduction	165
8.2 Experimental	165
8.2.1 NOHMs Preparation	165
8.2.2 Viscosity Measurement	166
8.2.3 CO ₂ Diffusivity and CO ₂ Capture Capacity using the ATR FT-IR	166
8.3 Results and Discussion.....	167
8.3.1 Characterization of NOHMs.....	167
8.3.2 Effect of Core Size on Viscosity	168
8.3.3 Effect of Core Size on CO ₂ Diffusivity	169
8.3.4 Effect of Core Fraction on Viscosity and CO ₂ Diffusivity.....	172

8.3.5 Effect of Temperature on CO ₂ Diffusivity	173
8.4 Potential Reactor Designs	174
8.5 Conclusions	176
CHAPTER 9	
CONCLUSIONS AND RECOMMENDATIONS	191
APPENDIX.....	196

List of Figures

Figure 2-1 CO ₂ capture capacities of liquid solvents at 0.1MPa and 25 °C.	19
Figure 2-2 Structures of cations and anions of conventional ILs.	20
Figure 2-3 Reaction schematics of CO ₂ with TSILs of (a) [pabim][BF ₄] and (b) [P ₆₆₆₁₄][Pro] and [P ₆₆₆₁₄][Met].	21
Figure 2-4 Proposed hydrogen bonding of cation with anion for salts made from DBU, TMG and Barton's base with ROH and CO ₂	22
Figure 2-5 (a) Structures of RevILs: (3-aminopropyl)-trimethoxysilane (TMSA), (3-aminopropyl)-triethylsilane (TETSA), (3-aminopropyl)-triethoxysilane (TESA), and (3-aminopropyl)-tripropylsilane (TPSA), and (b) Reversible reaction of RevILs with carbon dioxide where R = methyl or ethyl.	23
Figure 3-1 Classification of Nanoparticle Organic Hybrid Materials (NOHMs) and the list of five samples: NOHM-I-HPE (linker = sulfonic acid, polymer = polyetheramine); NOHM-I-PEI (no linker, polymer = polyethylenimine); NOHM-I-tPE (no linker, polymer = tertiary amine polyether); NOHM-C-HPE and NOHM-C-MPE (linker = glycidyl ether, polymer = polyetheramine).	43
Figure 3-2 Schematic diagram showing NOHMs synthesis.	44
Figure 3-3 Photo (a) and Transmission Electron Microscopy image (b) of a typical NOHMs sample (NOHM-I-tPE).	45
Figure 3-4 (a) 2D ¹ H- ¹³ C edited HSQC NMR spectra of NOHM-I-PE600 in DMSO- <i>d</i> ₆ at 25 °C. Red contour exhibits carbons of CH or CH ₃ (up) whereas blue exhibits CH ₂ (down). Peaks in the range $\delta_H = 3.70 - 2.86$ ppm of horizontal ¹ H spectra are assigned to CH and CH ₂ protons of counterion species. Cross marks indicate the shifted peaks of Polyetheramine M-600. (b) ATR FT-IR spectrum of NOHM-I-PE600 in the range of bending modes of NH ₃ ⁺	46
Figure 3-5 Schematic diagram of an in-situ CO ₂ capture and diffusivity measurement apparatus. (1) FT-IR spectrometer, (2) ATR optic and high pressure fluid cell, (3) gas line inlet, (4) gas line outlet, (5) CO ₂ pressure cylinder, (6) Data acquisition, (7) Temperature controller, (8) Venting line, (9) Diamond crystal, (10) Mirrors, (11) Infrared light source.	47
Figure 3-6 ATR FT-IR spectra of NOHM-I-PE2070 with various partial pressures of CO ₂ ranging from 0 to 5.5 MPa at 25 °C.	48
Figure 3-7 ATR FT-IR Spectra of ν_2 bands of NOHM-I-PE2070 pressurized by CO ₂ at 25 °C. (a) CO ₂ in vapor phase (up) and adsorbed CO ₂ in NOHM-I-PE2070 (down). The dotted lines indicate the curve fit spectra. (b) Peak behavior of ν_2 band of CO ₂ as a function of pressure.	49
Figure 3-8 CO ₂ capture capacity of NOHM-I-PE2070 vs. (a) P _{CO2} and (b) degree of swelling at 25 °C.	50

Figure 3-9 Thermogravimetric curves in oxygen atmosphere of: (a) POSS-based NOHMs with ionic bonding and the corresponding unbound polymers, and (b) POSS-based NOHMs with covalent bonding and the corresponding unbound polymers.	51
Figure 3-10 Examples of ^1H NMR spectra of the POSS, (a) the polymeric canopy and a POSS-based NOHMs with ionic bonding at 27 °C and (b) a POSS-based NOHMs with covalent bonding at 27 °C. Samples were prepared in CDCl_3	52
Figure 3-11 ATR FT-IR spectra at 25 °C of: (a) POSS-I-PC460 and its corresponding unbound polymer, (b) POSS-I-PC740 and its corresponding polymer.	53
Figure 3-12 DSC traces of: (a) POSS-I-PC460 and its unbound polymer, (b) POSS-I-PC740 and its corresponding unbound polymer, and (c) POSS-I-PS1260 and its corresponding unbound polymer.	54
Figure 4-1 Scheme of the synthesis of PEG-based NOHMs	70
Figure 4-2 ATR FT-IR spectra of PEG1K, Ionized PEG1K and NOHM-I-PEG1K-E.	70
Figure 4-3 Thermal stability of Ionized PEGs with various molecular weights and the corresponding PEGs in oxygen environment with a ramping rate 5 °C/min.	71
Figure 4-4 Thermal stability of NOHMs with various chain lengths and the corresponding PEGs in oxygen environment with a ramping rate 5 °C/min.	72
Figure 4-5 Thermal stabilities of NOHMs with the same core fraction and various chain lengths in oxygen environment with a ramping rate 5 °C/min.	73
Figure 4-6 Thermal stability of, PEG1K, PEG1K / NP-25, Ionized PEG1K and NOHM-I-PEG1K-E in oxygen environment with a ramping rate 5 °C/min.	74
Figure 4-7 Cyclic thermal stability of NOHM-I-PEG1K-E and PEG1K (temperature swing from 20 °C to 120 °C/140 °C with a ramping rate 5 °C/min and isothermal for 5 minutes, each cycle is 25/29 minutes, respectively)	75
Figure 4-8 Thermally-induced swelling of NOHMs with various chain lengths (conducted at $P_{\text{CO}_2} = 0$ MPa).....	76
Figure 5-1 CO_2 solubility in NOHMs with various chain length at 60 °C and $P_{\text{CO}_2} = 0.4 - 5.5$ MPa.	100
Figure 5-2 CO_2 capture capacity and CO_2 -induced swelling of NOHM-I-HPE with various molecular weights of PEGs and the corresponding pure PEGs.	101
Figure 5-3 Ratios of delta swelling of mPEG to NOHM-I-PEGs at 60 °C and $P_{\text{CO}_2} = 0.8 - 5.5$ MPa. (Amount of swelling percentage caused by 0.2 mmol/g CO_2 capture capacity is defined as a delta swelling)	102
Figure 5-4 A typical Raman spectrum of NOHM-I-HPE	103
Figure 5-5 Raman spectra in the $\nu_a(\text{CH}_2)$ and $\nu_s(\text{CH}_2)$ regions for PEGs and NOHM-I-PEGs..	104
Figure 5-6 Ratios of Raman spectral intensity of $\nu_a(\text{CH}_2)$ to $\nu_s(\text{CH}_2)$ for PEGs and NOHM-I-PEGs at various molecular weights.	105
Figure 5-7 Confirmation of ionic bonding between the linker and Jeffamine 2070 provided by ^1H NMR spectra of: (a) NOHM-I-HPE-3.8, (b) NOHM-I-HPE-2.5, (c) NOHM-I-HPE-	

	2.0 and (d) NOHM-I-HPE-1.0 at 27 °C. All samples were prepared in D ₂ O. The symbol ■ indicates the location of the H _c peak in the unbound Jeffamine 2070. ...	106
Figure 5-8	¹³ C NMR spectra of NOHM-I-HPE-3.8 in D ₂ O: (a) before and (b) after exposure to CO ₂ (~ 0.7 MPa) at 27 °C.	107
Figure 5-9	2D ROESY NMR spectra of: (a) NOHM-I-HPE-3.8, (b) NOHM-I-HPE-2.5, (c) NOHM-I-HPE-2.0 and (d) NOHM-I-HPE-1.0 in D ₂ O at 27 °C. Numbers on each graph indicate the integrated intensities. The red contours correspond to diagonal and TOCSY (Total Correlation Spectroscopy, off-diagonal) peaks, while the blue contours exhibit ROEs.	108
Figure 5-10	Raman spectra of NOHMs with various grafting densities (3.8, 2.5, 2.0 and 1.0 chains/nm ²): (a) full spectra, and (b) CH ₂ stretching region at 25 °C.	109
Figure 5-11	Effect of grafting density on the ν_{s,CH_2} shift and the intensity (I) ratios of symmetric to asymmetric stretching of CH ₂ in NOHMs and unbound polymer.	110
Figure 5-12	ATR FT-IR spectra of: (a) NOHMs with various grafting densities (3.8, 2.5, 2.0 and 1.0 chains/nm ²) before exposure to CO ₂ , and (b) NOHM-I-HPE-3.8 before and after exposure to CO ₂ (5.5 MPa, 25 °C).	111
Figure 5-13	ATR FT-IR spectra of ν_2 bending modes of CO ₂ absorbed in NOHMs with various grafting densities (3.8, 2.5, 2.0 and 1.0 chains/nm ²): (a) NOHM-I-HPE-3.8, (b) NOHM-I-HPE-2.5, (c) NOHM-I-HPE-2.0 and (d) NOHM-I-HPE-1.0 at 25 °C.	112
Figure 5-14	Area (A) ratios of in-plane ($\nu_{2,in-plane}$) to out-of-plane ($\nu_{2,out-of-plane}$) bending modes of CO ₂ absorbed in NOHMs with different grafting densities (3.8, 2.5, 2.0 and 1 chains/nm ²) and in Jeffamine 2070 as a function of: (a) CO ₂ pressure, and (b) CO ₂ capture capacity at 25 °C.	113
Figure 5-15	CO ₂ -induced swelling (S) behaviors of NOHMs (grafting densities = 3.8, 2.5, 2.0 and 1 chains/nm ²) and Jeffamine 2070 at 25 °C (a) as a function of CO ₂ pressure, and (b) CO ₂ capture capacity.	114
Figure 6-1	A Schematic diagram for a dual-chamber reactor for gas sorption with pressure range 0.1 -0.34 MPa and temperature range 25 – 80°C.	128
Figure 6-2	ATR FT-IR spectra of synthesized NOHMs (a) NOHM-I-HPE, (b) NOHM-C-HPE	129
Figure 6-3	¹³ C NMR of NOHM-I-HPE loaded with ¹³ CO ₂ . (NOHM-I-HPE in DMSO-d ₆ was placed in a high pressure NMR tube at P ¹³ _{CO2} = 0.5 MPa).	130
Figure 6-4	Thermal stabilities of NOHMs and their corresponding polymers determined by thermogravimetric analyses. (a) NOHM-I-HPE, (b) NOHM-C-HPE and NOHM-C-MPE, (c) NOHM-I-tPE and (d) NOHM-I-PEI. Mass (%) was calculated based on only the mass of the organic portion of NOHMs.	131
Figure 6-5	Effect of bonding types used in the synthesis of NOHMs on CO ₂ capture capacity as a function of partial pressure of CO ₂ at 25 °C.	132
Figure 6-6	Effect of bonding types used in the synthesis of NOHMs on CO ₂ capture capacity as a function of temperature at P _{CO2} = 0.32 MPa.	133

Figure 6-7 Sorption kinetics of CO ₂ and other gases in NOHM-I-HPE (T = 25 °C, P _{CO2} = 0.34 MPa, P _{N2O} = 0.34 MPa, P _{O2} = 0.34 MPa and P _{N2} = 0.34 MPa).....	134
Figure 6-8 Sorption kinetics of CO ₂ and other gases in NOHM-C-HPE (T = 25 °C, P _{CO2} = 0.34 MPa, P _{N2O} = 0.34 MPa, P _{O2} = 0.34 MPa and P _{N2} = 0.34 MPa).....	135
Figure 6-9 Multi-cycle CO ₂ capture using NOHM-I-HPE (Capture conditions: T = 25 °C and P _{CO2} = 0.34 MPa; Regeneration conditions: T = 25 °C and P _{vacuum} = 0.00025 MPa).	136
Figure 6-10 Multi-cycle CO ₂ capture using NOHM-C-HPE (Capture conditions: T = 25 °C and P _{CO2} = 0.34 MPa; Regeneration conditions: T = 25 °C and P _{vacuum} = 0.00025 MPa).	137
Figure 6-11 Multi-cycle CO ₂ capture using NOHM-C-HPE (Capture conditions: T = 25 °C and P _{CO2} = 0.34 MPa; Regeneration conditions: T = 120 °C with N ₂ purge).	138
Figure 6-12 Effect of ether groups on CO ₂ capture capacity of NOHMs at 25 °C.....	139
Figure 6-13 Effect of amine groups on CO ₂ capture capacity of NOHMs (P _{CO2} = 0.34 MPa and T = 30 °C)	140
Figure 7-1 NOHMs' (a) configuration and two NOHMs examples: (b) NOHM-I-HPE, (c) NOHM-C-HPE and (d) NOHM-C-HPE photo.	154
Figure 7-2 Absorption of N ₂ (P = 0.1 MPa), pre-humidified N ₂ (P = 0.1 MPa), 200 ppm SO ₂ in N ₂ (P = 0.1 MPa) and 3000 ppm SO ₂ in N ₂ (P = 0.3 MPa) in NOHM-I-HPE at 25 °C.	155
Figure 7-3 CO ₂ capture capacities of SO ₂ -exposed and pristine NOHMs (NOHM-I-HPE and NOHM-C-HPE) at P _{CO2} = 0.2MPa and 25 °C.....	156
Figure 7-4 Derivative weight changes of NOHM-I-HPE after exposure to SO ₂ and CO ₂ . (ramping rate: 5 °C/min in oxygen environment).....	157
Figure 7-5 Raman spectra of NOHM-I-HPE before and after SO ₂ exposure (P = 0.3 MPa) at 25 °C.	158
Figure 7-6 Breakthrough curves for the removal of CO ₂ and SO ₂ using NOHMs at 25 °C (CO ₂ inlet = 14% and SO ₂ inlet = 200 ppm in N ₂)	159
Figure 7-7 Effect of SO ₂ on CO ₂ -induced swelling of (a) NOHM-I-HPE and (b) NOHM-C-HPE	160
Figure 7-8 ATR FT-IR spectra of ν_2 bands of CO ₂ and deconvoluted ν_2 bands of CO ₂ absorbed in NOHM-I-HPE at 0.41 MPa of CO ₂ /SO ₂	161
Figure 7-9 Effect of SO ₂ on area ratios of in-plane ($V_{2,in-plane}$) to out-of-plane ($V_{2,out-of-plane}$) bending modes of CO ₂ absorbed in (a) NOHM-I-HPE and (b) NOHM-C-HPE. ...	162
Figure 8-1 Schematic diagram of NOHM-I-HPE.	179
Figure 8-2 Viscosity of NOHM-I-HPE of 7, 12, and 22 core with a fixed core fraction 15 wt% at various temperatures.....	180
Figure 8-3 A/A _{eq} of CO ₂ diffusion into NOHM-I-HPE as a function of time at various temperatures. (P _{CO2} = 0.1 MPa).....	181

Figure 8-4	Effect of core size on viscosity at 40 °C and CO ₂ diffusivity in NOHM-I-HPE of 7, 12 and 22 nm core with a fixed core fraction (15 wt%) at 25 °C	182
Figure 8-5	Scheme for CO ₂ diffusion pathway in NOHMs and CO ₂ diffusion pathway diameter	183
Figure 8-6	Effect of core fraction on viscosity at 40 °C and CO ₂ diffusivity in NOHM-I-HPE of 7 nm core with core fraction 15, 20, 25, 30 and 40 wt% at 25 °C.....	184
Figure 8-7	Effect of core fraction on viscosity at 40 °C and CO ₂ diffusivity in NOHM-I-HPE of 12 nm core with core fraction 15, 20 and 30 wt% at 25 °C.....	185
Figure 8-8	Viscosity and CO ₂ diffusivity in NOHM-I-HPE with 12 core and core fraction 15 wt% at various temperatures.....	186
Figure 8-9	Schematic diagram of a spraying tower for CO ₂ capture using Liquid-like NOHMs	187
Figure 8-10	Schematic diagram of a supported liquid membrane for NOHMs	188
Figure 8-11	Schematic diagram of a combined technology for CO ₂ capture and conversion to alcohols using photochemical NOHMs.....	189

List of Tables

Table 3-1 List of POSS-based NOHMs samples with their chemical composition and schematic representation of their overall structure.	42
Table 4- 1 List of NOHMs and polymers	69
Table 5-1 List of NOHMs samples with their compositions and grafting densities determined by thermogravimetric analyses.	99
Table 8-1 Comparison of estimated $^eD_{e,CO_2}$ and measured $^mD_{e,CO_2}$ of NOHMs with various structural parameters at 25 °C.	178
Table A1. Abbreviations of selected cations in Ionic Liquids.....	196
Table A2. Abbreviations of selected anions in Ionic Liquids.....	197

Acknowledgement

Firstly, I want to thank my advisor Prof. Alissa Park for all the support and guidance. As an advisor, she gives me not only directions on research but also so much help to my personal life. I also want to thank my committee members, Prof. Klaus Lackner, Prof. Paul Duby, Prof. Raimondo Betti and Prof. Lynden Archer. Prof. Lackner has always inspired me by his questions and advices since I took my qualify exam. Prof. Duby gives me many suggestions for the dissertation and my career. It is really my pleasure to work with him in his Aquatic Chemistry class. I want to thank Prof. Betti for his generosity to be my committee member. I also sincerely appreciate Prof. Archer's advices and comments. It is really an honor to have him as my committee member.

I would also like to thank people whom I work with in my research project. It is a pleasure to work with Dr. Camille Petit. She is always willing to offer helps to my research and experiments. I also want to thank Dr. Youngjune Park, Aaron Garg, Nanayan Subramanian, Justin Chow, Greeshma Erukonda and Timothy Sharobem for their helps in experiments and my dissertation.

I am so grateful for the support from my wife, Ching-Chun (Diane) Chou. Without her comfort and love, I would not be able to face difficulties in research and life every single day and complete the dissertation. I also want to thank my parents and sisters for their supports and encouragements to let me do what I want to do. In the end, I want to give thanks to God for His love and grace which enable me to finish my PhD and move forward.

To my wife, Ching-Chun Chou, for her love and support

CHAPTER 1

INTRODUCTION

Carbon dioxide, CO₂, is one of the greenhouse gases and its atmospheric concentration has increased at an annual rate of about 2 ppm, and thus, the development of efficient CO₂ capture technologies is essential for the future of carbon-based energy. The most commonly employed approach for CO₂ capture is using amine-based solvents that react with gaseous CO₂ to form carbamates (George and Weiss 2001; George and Weiss 2002; da Silva and Svendsen 2004; Gabrielsen et al., 2005). Among the amine-based solvents, monoethanolamine (MEA) is one of the most favored solvents for CO₂ capture due to its high CO₂ capture capacity (i.e., ~3.0 mmol of CO₂ / g of 30wt% MEA solvent) (Shen and Li, 1992) and fast reaction kinetics. Unfortunately, there are some drawbacks that delay the implementation of MEA-based capture in large scale. MEA has high volatility, and its corrosive fume is a concern for the process design and operation. As a result, the concentration of MEA in water has to be limited to 15 – 30 wt% to reduce corrosive fume and this makes the design and the operation of the CO₂ capture and the solvent regeneration processes complicated and costly (Liu et al., 1999; Zhang et al., 2006).

In answer to these concerns associated with MEA, a number of innovative materials including amine functionalized solid mesoporous sorbents (Knowles et al., 2005; Millward and Yaghi 2005; Harlick and Sayari 2006; Chaffee et al., 2007; Bastin et al., 2008; Hicks et al., 2008; Serna-Guerrero et al., 2008; Qi et al., 2011), liquid solvents (i.e., ionic liquids) (Anthony et al., 2002; Aki et al., 2004; Anthony et al., 2004; Anthony et al., 2005) and organic solvents such as aminoalkylsilane (Blasucci et al., 2010; Blasucci et al., 2010)) are being developed to capture CO₂. Ionic liquids are particularly intriguing since they generally exhibit negligible vapor

Chapter 1

pressure even at elevated temperatures. Ionic liquids can be synthesized with task-specific functional groups (e.g., amine groups for CO₂ capture), and they can also possess interesting features such as reversible and phase change behaviors (Heldebrant et al., 2008). The current drawbacks of ionic liquids as CO₂ capture media include their complex synthesis and purification steps, and high cost.

Considering these limitations of CO₂ capture solvents, a new class of CO₂ capture medium named Nanoparticle Organic Hybrid Materials (NOHMs) has been formulated. Depending on the selection of organic materials, NOHMs can be synthesized in various forms: liquid-like solvent, solid sorbent or gel-like materials. By grafting polymer onto inorganic nanostructures, polymeric chains are anchored to improve the thermal stability, and the resulting NOHMs exhibit near zero vapor pressure at temperatures below their thermal decomposition temperatures. The NOHMs are relatively simple and easy to prepare, and they possess high degree of tunability since both the nanoparticle cores and the polymeric chains can be selected from a wide variety of commercially available materials. Therefore, NOHMs have a great potential for various industrial applications including CO₂ capture.

This dissertation is prepared as a collection of four published articles as well as four manuscripts in preparation. However, the structure of the dissertation does not strictly follow the published papers to provide a coherent flow to the dissertation.

Reference

- Aki, S. N. V. K., Mellein, B. R., Saurer, E. M. and Brennecke, J. F., "High-Pressure Phase Behavior of Carbon Dioxide with Imidazolium-Based Ionic Liquids", *J. Phys. Chem. B*, 108, 20355-20365, 2004.
- Anthony, J. L., Aki, S. N. V. K., Maginn, E. J. and Brennecke, J. F., "Feasibility of using ionic liquids for carbon dioxide capture", *Int. J. Environmental Technology and Management*, 4, 105-115, 2004.
- Anthony, J. L., Anderson, J. L., Maginn, E. J. and Brennecke, J. F., "Anion Effects on Gas Solubility in Ionic Liquids", *J. Phys. Chem. B*, 109, 6366-6374, 2005.
- Anthony, J. L., Maginn, E. J. and Brennecke, J. F., "Thermodynamic Properties and Solubilities of Gases in 1-*n*-butyl-3-methylimidazolium hexafluorophosphate", *J. Phys. Chem. B*, 106, 7315-7320 2002.
- Bastin, L., B rcia, P. S., Hurtado, E. J., Silva, J. A. C., Rodrigues, A. E. and Chen, B., "A Microporous Metal-Organic Framework for Separation of CO₂/N₂ and CO₂/CH₄ by Fixed-Bed Adsorption", *J. Phys. Chem. C*, 112, 1575-1581, 2008.
- Blasucci, V., Hart, R., Mestre, V. L., Hahne, D. J., Burlager, M., Huttenhower, H., Thio, B. J. R., Pollet, P., Liotta, C. L. and Eckert, C. A., "Single component, reversible ionic liquids for energy applications", *Fuel*, 89, 1315-1319, 2010.
- Blasucci, V. M., Hart, R., Pollet, P., Liotta, C. L. and Eckert, C. A., "Reversible ionic liquids designed for facile separations", *Fluid Phase Equilibria*, 294, 1-6, 2010.
- Bourlinos, A. B., Chowdhury, S. R., Herrera, R., Chalkias, N., Jiang, D. D., Zhang, Q., Archer, L. A. and Giannelis, E. P., "Functionalized Nanostructures with Liquid-Like Behavior: Expanding the Gallery of Available Nanostructures", *adv. Funct. Mater.*, 15, 1285-1290, 2005.
- Bourlinos, A. B., Herrera, R., Chalkias, N., Jiang, D. D., Zhang, Q., Archer, L. A. and Giannelis, E. P., "Surface-Functionalized Nanoparticles with Liquid-Like Behavior", *Adv. Mater.*, 17, 234-237, 2005.
- Chaffee, A. L., Knowles, G. P., Liang, Z., Zhang, J., Xiao, P. and Webley, P. A., "CO₂ capture by adsorption: Materials and process development", *International Journal of Greenhouse Gas Control*, 1, 11-18, 2007.
- da Silva, E. F. and Svendsen, H. F., "Ab Initio Study of the Reaction of Carbamate Formation from CO₂ and Alkanolamines", *Ind. Eng. Chem. Res.*, 43, 3413-3418, 2004.
- Gabrielsen, J., Michelsen, M. L., Stenby, E. H. and Kontogeorgis, G. M., "A Model for Estimating CO₂ Solubility in Aqueous Alkanolamines", *Ind. Eng. Chem. Res.*, 44, 3348-3354, 2005.
- George, M. and Weiss, R. G., "Chemically Reversible Organogels: Aliphatic Amines as "Latent" Gelators with Carbon Dioxide", *J. Am. Chem. Soc.*, 123, 10393-10394, 2001.
- George, M. and Weiss, R. G., "Chemically Reversible Organogels via "Latent" Gelators. Aliphatic Amines with Carbon Dioxide and Their Ammonium Carbamates", *Langmuir* 2003, 18, 7124-7135, 2002.

Chapter 1

- Harlick, P. J. E. and Sayari, A., "Applications of Pore-Expanded Mesoporous Silicas. 3. Triamine Silane Grafting for Enhanced CO₂ Adsorption", *Ind. Eng. Chem. Res.*, 45, 3248–3255, 2006.
- Heldebrant, D. J., Yonker, C. R., Jessop, P. G. and Phan, L., "Organic liquid CO₂ capture agents with high gravimetric CO₂ capacity", *Energy Environ. Sci.*, 1, 487–493, 2008.
- Hicks, J. C., Drese, J. H., Fauth, D. J., Gray, M. L., Qi, G. and Jones, C. W., "Designing Adsorbents for CO₂ Capture from Flue Gas-Hyperbranched Aminosilicas Capable of Capturing CO₂ Reversibly", *J. Am. Chem. Soc.*, 130, 2902–2903, 2008.
- Knowles, G. P., Graham, J. V., Delaney, S. W. and Chaffee, A. L., "Aminopropyl-functionalized mesoporous silicas as CO₂ adsorbents", *Fuel Processing Technology*, 86, 1435-1448, 2005.
- Liu, Y. D., Zhang, L. Z. and Watanasiri, S., "Representing vapor-liquid equilibrium for an aqueous MEA-CO₂ system using the electrolyte nonrandom-two-liquid model", *Ind. Eng. Chem. Res.*, 38, 2080-2090, 1999.
- Millward, A. R. and Yaghi, O. M., "Metal–Organic Frameworks with Exceptionally High Capacity for Storage of Carbon Dioxide at Room Temperature", *J. Am. Chem. Soc.*, 127, 17998–17999, 2005.
- Qi, G., Wang, Y., Estevez, L., Duan, X., Anako, N., Park, A.-H. A., Li, W., Jones, C. W. and Giannelis, E. P., "High efficiency nanocomposite sorbents for CO₂ capture based on amine-functionalized mesoporous capsules", *Energy & Environmental Science*, 4, 444-452, 2011.
- Rodriguez, R., Herrera, R., Archer, L. A. and Giannelis, E. P., "Nanoscale Ionic Materials", *Adv. Mater.*, 20, 4353-4358, 2008.
- Serna-Guerrero, R., Da'na, E. and Sayari, A., "New Insights into the Interactions of CO₂ with Amine-Functionalized Silica", *Industrial & Engineering Chemistry Research*, 47, 9406-9412, 2008.
- Zhang, J., Zhang, S., Dong, K., Zhang, Y., Shen, Y. and Lv, X., "Supported Absorption of CO₂ by Tetrabutylphosphonium Amino Acid Ionic Liquids", *Chem. Eur. J.*, 12, 4021-4026, 2006.

CHAPTER 2

BACKGROUND AND MOTIVATION

2.1 Solvents for CO₂ Capture

Several alternative materials have been proposed to substitute amine scrubbing, including solid sorbents (Chue et al., 1995; Choi et al., 2009), membranes (Kim et al., 2004; Bounaceur et al., 2006), and liquid sorbents (Bates 2002; Anthony 2004; Anthony 2005). In particular, the recent investigation of novel liquid materials, such as Ionic Liquids (ILs), CO₂ Binding Organic Liquids (CO₂BOLs) have expanded the selection of alternative solvents for amine-based reagents. The CO₂ capture capacities of the selected liquid materials are shown in Figure 2-1.

ILs are composed of cations and anions, and their melting points are below 100 °C, whereas typical molten salts exist in solid phase even at hundreds of degrees. Recently, ILs have gained great attention because of their promising CO₂ capture capacities with thermal stability and non-volatility (Cadena et al., 2004). Compared to the amine-based reagents which utilize strong chemical interactions with CO₂ by forming carbamate in dry conditions ($-\Delta H = \sim 30$ KJ/mol) (McCann, Maeder et al. 2011) and carbonate or bicarbonate in the presence of water ($-\Delta H = \sim 80$ to ~ 130 KJ/mol) (Kim and Svendsen 2011), ILs interact with CO₂ via relatively weak interactions ($-\Delta H = \sim 15$ KJ/mol) (Cadena et al., 2004), and thus less energy is required for regeneration of ILs. Versatile tunability of physicochemical properties of ILs via various combinations of anions and cations and their structural modifications allow ILs to be employed in a wide variety of applications.

CO₂BOLs, liquid mixtures of organic alcohols and amidine/guanidine bases, are also promising candidate materials for CO₂ capture (Heldebrant et al., 2008). CO₂BOLs can react

with CO₂ to form a pair of cation and anion and the reaction is reversible as CO₂ is removed. Based on this characteristic, a series of reversible ILs have also been developed to capture CO₂ as “double-action” solvents. In a first step, the materials capture CO₂ which leads to the formation of ILs. These resulting ILs can also subsequently capture CO₂ (Blasucci et al., 2009).

Various cations and anions have been combined to form various types of ILs, and typical example, consisting of nitrogen- or phosphorous-containing organic cations, are shown in Figure 2-2. Asymmetry of the cations accounts for the low melting points of ILs and the anions are responsible for ILs' physical properties. In addition to their negligible vapor pressure ($\sim 1 \times 10^{-10}$ Pa) (Paulechka et al., 2003), ILs also have several advantageous properties as solvents over molecular solvents, including high thermal stability over a very wide temperature range, up to 200 °C (Headley and Ni 2007).

As a result, ILs have been proposed for CO₂ capture and many other applications. To date, ILs for CO₂ capture can basically be classified into three major categories based on their CO₂ capture mechanisms: (i) conventional ILs, (ii) Task-Specific ILs (TSILs), and (iii) Reversible ILs (RevILs).

2.1.1 CO₂ Capture using Conventional Ionic Liquids

Conventional ILs that do not contain any functional groups (e.g. amines) also exhibit promising CO₂ capture capacity and selectivity. A detailed study of solubilities of various gases, including water vapor, Ar, CO, CO₂, CH₄, C₂H₄, C₂H₆, H₂, N₂, and O₂ in [bmim][PF₆] (See Appendix for full chemical names), was conducted by Anthony et al (Anthony, Maginn et al. 2002). Besides water vapor, CO₂ exhibits highest solubility in [bmim][PF₆], followed by CH₄, C₂H₄, and C₂H₆. It has been indicated that the large quadrupole moment of CO₂ makes it highly

soluble in [bmim][PF₆]. Anderson et al. also found that even common ILs, such as [hmim][Tf₂N], have excellent selectivity for CO₂ relative to N₂ and other components in flue-gas streams based on physical absorption (Anderson et al., 2007). Blanchard et al. determined the solubility of CO₂ in a series of imidazolium-based ILs in the pressure region of 1 to 100 bar, and their results show the solubility follows in sequence of [bmim][PF₆] > [omim][PF₆] > [omim][BF₄] > [N-bupy][BF₄] > [bmim][NO₃] > [emim][EtSO₄] (Blanchard et al., 2001). Interestingly, imidazolium-based ILs exhibit relatively high CO₂ capture capacity (~0.3 mmol/g) (Anthony et al., 2002).

The solvating mechanisms of ILs for CO₂ are not fully understood, but several plausible explanations have been put forth. Kazarian et al. found spectroscopic evidence of a Lewis acid–base intermolecular interaction between anions and CO₂ using Attenuated Total Reflectance (ATR) Fourier-transform infrared (FT-IR) spectroscopy (Kazarian et al., 2000). Because the anion acts as a basic site for CO₂, such a weak Lewis acid–base interaction between anion and CO₂ offers favorable affinity to capture CO₂. Cadena et al. investigated the effect of anions in alkylimidazolium-based ILs for CO₂ capture via experimental and molecular simulation studies, and they revealed that the anions play a critical role in interacting with CO₂ (Cadena et al., 2004). Anthony et al. also investigated the effect of anions, focusing on three anions: [BF₄][−], [PF₆][−], and [Tf₂N][−], with [bmim]⁺ as a counter ion, and they observed that [bmim][Tf₂N] exhibits relatively high capacity for CO₂ while [bmim][BF₄] and [bmim][PF₆] have lower affinity for capturing CO₂ (Anthony 2005).

Another detailed study on the effect of anions on CO₂ capture was conducted by focusing on the influence of fluorination on CO₂ solubility in ILs (Kroon et al., 2004) because strong C–F bonds are capable of causing an increase in rigidity and a decrease in polarity. These unique

properties can result in a high gas solubility. (Almantariotis, Gefflaut et al. 2010) The fluorinated anions, such as $[\text{BF}_4]^-$, $[\text{PF}_6]^-$, $[\text{Tf}_2\text{N}]^-$, $[\text{TfO}]^-$, and $[\text{methide}]^-$, with $[\text{bmim}]^+$ were compared with non-fluorinated anions of $[\text{DCA}]^-$ and $[\text{NO}_3]^-$, and the results indicate that ILs with fluorinated anions show relatively high CO_2 solubilities. In particular, ILs that have anions with fluoroalkyl groups, such as $[\text{TfO}]^-$, $[\text{Tf}_2\text{N}]^-$, and $[\text{methide}]^-$, showed the highest CO_2 solubilities. They also reported that the order of solubility in different types of anions was observed as $[\text{NO}_3]^- < [\text{DCA}]^- < [\text{BF}_4]^- \approx [\text{PF}_6]^- < [\text{TfO}]^- < [\text{methide}]^- < [\text{Tf}_2\text{N}]^-$, where $[\text{TfO}]^-$, $[\text{methide}]^-$, and $[\text{Tf}_2\text{N}]^-$ contain one, two, and three CF_3 groups, respectively. It has been known that fluorination can improve the “ CO_2 -philicity” (Raveendran and Wallen 2003). Therefore, fluorination of the alkyl chains in cations, as well as anions, has also been investigated to increase CO_2 capture capacity. In addition, the effects of anions with sulfate and phosphonium groups on CO_2 solubility were investigated. Comparable CO_2 capture capacity was exhibited to imidazolium-based ILs (Zhang et al., 2004).

Although many studies have proven that CO_2 solubility is highly dependent on their anions, the effect of cations on CO_2 solubility in ILs was also investigated (Aki 2004). With $[\text{Tf}_2\text{N}]^-$ as an anion, three different imidazolium-based cations were chosen to investigate the effect of cation on CO_2 solubility in ILs, including $[\text{hmim}]^+$, $[\text{omim}]^+$, and $[\text{bmim}]^+$. It was also found that longer alkyl chains noticeably increase CO_2 solubility (Blanchard et al., 2001). It has been known that ILs usually exhibit low volume expansion compared to general organic solvents (Jacquemin et al., 2007). Cadena et al. reported that both cations and anions could be arranged to form relatively rigid structures by coulombic interactions, and thus those molecular arrangements could generate a large amount of ‘free volume’ to accommodate CO_2 (Cadena et al., 2004).

Introducing ether groups into cations has been also suggested to increase CO₂ solubility in ILs as the presence of ether groups may render ILs more flexible and increase free volume (Beckman 2004). An additional benefit is that oxygen present in the ether groups is also able to interact with CO₂ via dipole–quadrupole interaction (Ghosal et al., 1996). ILs with ether groups in cations, [ECOENG500][MeSO₄], were compared against [hmim][Tf₂N] for CO₂ solubility (Crosthwaite et al., 2005). It was found that [ECOENG500][MeSO₄] had comparable CO₂ solubility to [hmim][Tf₂N] in all tested partial pressures of CO₂. Since [ECOENG500][MeSO₄] consists of long-chain polyethylene glycol (PEG), it is believed that a relatively large amount of free volume could be provided from PEG, therefore increasing CO₂ solubility. In addition to [ECOENG500][MeSO₄], other ILs with ether groups have also been found to absorb high amount of CO₂, such as [N₄₄₄₄][doc] (Muldoon et al., 2007). Carbonyl groups and long branched alkyl groups existing in [N₄₄₄₄][doc] also help to explain its high CO₂ solubility, which is even higher than fluorinated ILs at high partial pressure of CO₂. However, the extremely high viscosity of [N₄₄₄₄][doc], 12,100 cP at 25 °C, is one of the challenges for its practical application.

Other functional groups such as carbonyl and ester in ILs have also been investigated. [b₂Nic][Tf₂N], a pyridinium-based IL with a butyl ester group, was studied by Muldoon et al. to investigate the effect of ester groups on CO₂ solubility (Muldoon et al., 2007). Results indicated that [b₂Nic][Tf₂N] has noticeably higher CO₂ solubility than [hmim][Tf₂N] under high partial pressure of CO₂, which is a result of minor interactions between CO₂ and ester groups. Since conventional ILs have no particular functional groups, such as amines, regeneration of used ILs is relatively easily accomplished by a mild heat treatment (~ 70 – 80 °C), inert gas bubbling or pressure swing followed by vacuum (Hou and Baltus 2007). Although there is a relatively larger solubility of CO₂ in conventional ILs than in conventional organic solvents, such as heptanes,

cyclohexane, benzene, and ethanol (Anthony et al., 2002), the CO₂ capture capacity of the conventional ILs is still limited, and thus further modifications are required.

2.1.2 CO₂ Capture using Task-Specific Ionic Liquids

Since conventional ILs have limited CO₂ solubilities due to their relatively weak physical and secondary chemical interaction toward CO₂, novel types of ILs with task-specific functional groups that can interact strongly with CO₂ are desired. Recently, TSILs have been synthesized by introducing amine groups, which can capture rapidly and efficiently. Bates et al. synthesized the first type of TSILs, [pabim][BF₄], shown in Figure 2-3 (Bates 2002). They successfully introduced the primary amines on cations, and it allowed for the formation of an ammonium carbamate salt which reacted with CO₂, in the same way as in a conventional amine scrubbing fluid. The molar equilibrium ratio of CO₂ to [pabim][BF₄] was 1:2. They also showed that the weight gain associated with CO₂ captured in the [pabim][BF₄] is 7.4%, while only 0.0881% was found in [hmim][PF₆]. The existence of the primary amine boosted the CO₂ solubility in TSILs, while increased CO₂ solubilities in [pabim][BF₄] were also found at higher partial pressure of CO₂. This suggested that CO₂ dissolution in [pabim][BF₄] was through chemical and physical sorption.

The previous examples of TSILs all led to the use of a CO₂ : ILs molar ratio of 1:2. However, Gurkan et al. recently reported the preparation of new amine-based TSILs resulting in an equimolar ratio between the two entities (Gurkan et al., 2010). Such a behavior significantly enhances the CO₂-capture capacity of ILs. High solubility was achieved by introducing the amine functionality on the anionic component and not on the cationic one as in case of ‘regular’ TSILs. Specifically, the ILs used by Gurkan et al. consisted of [P₆₆₆₁₄]⁺ and [Met][−] or [Pro][−]

(Figure 2-3). In the presence of CO₂, the amino group of the ILs reacts with CO₂ and forms carbamic acid.

Besides employing the primary amine, nitrile groups recently was included in TSILs to try to improve the CO₂ selectivity and permeance by varying CO₂ solubility and viscosity. Mahurin et al. prepared a series of nitrile-containing ILs for supported IL membranes (SILMs) (Mahurin et al., 2010). These nitrile-containing ILs showed high CO₂ solubilities and selectivities over nitrogen. Among them, 1-ethyl-3-methylimidazolium tetracyanoborate, [emim][B(CN)₄] exhibited the highest CO₂ solubility (~0.13 mmol/g) as well as permeance, even outweighing [emim][Tf₂N].

Pyrrolide-containing TSIL represents another type of nitrogen-based TSIL. This material has been recently developed by Gurkan et al. (Gurkan et al., 2010). The ILs described in their study contain [P₆₆₆₁₄]⁺ and 2-cyanopyrrolide, [2-CNpyr]⁻. The pyrrolide side reacts with CO₂ to form the derived carboxylate (1:1 ratio). The repartition of charges in the resulting compound is thus similar to that of the initial IL. Recently, Goodrich et al. also reported amine-functionalized anion-tethered ionic liquids composed of [P₆₆₆₁₄]⁺ and glycinate [Gly]⁻, alante [Ala]⁻, sarcosinate [Sar]⁻, valinate [Val]⁻, leucinate [Leu]⁻, and isoleucinate [Ile]⁻ (Goodrich et al., 2010). In particular, [P₆₆₆₁₄][Gly], [P₆₆₆₁₄][Ile], [P₆₆₆₁₄][Sar], and [P₆₆₆₁₄][Ala] reached more than 0.5 mol of CO₂ per mole of IL at P_{CO2} < 0.1 MPa.

Wang et al. studied the solubility of CO₂ in a triethylbutylammonium acetate TSIL ([N₂₂₂₄][CH₃COO]) and its derived hydrated complexes (Wang et al., 2011). In dried TSIL, the capture mechanism mainly involves Lewis acid-based interactions, in the case of the hydrated complexes, CO₂, H₂O and the acetate component react to form the bicarbonate ion and acetic

acid. The mole fractions reported at room temperature and a pressure of 0.1MPa range from 0.05 to 0.39.

Although amine-functionalized TSILs had significantly higher CO₂ capture capacities, relatively high viscosity was also found in neat TSILs. Furthermore, even higher viscosity was observed in TSILs in complexation with CO₂, forming a gel-like ionic soft material (Soutullo et al., 2007). A molecular simulation study determined that the high viscosity in neat TSILs is from a strong interaction of hydrogen bonding between anions of TSILs and the primary amine tethered to cations of TSILs (Yu et al., 2007). Another simulation study conducted by Gutowski and Maginn clarified the mechanism of the dramatically increased viscosity in TSILs (Gutowski and Maginn 2008). Their studies suggested that the increased viscosity in the complexation of TSIL and CO₂ was due to the formation of a powerful and extensive hydrogen bonding network.

In order to manage the viscosity issue, Bara et al. dissolved a TSIL into a conventional RTIL, [hmim][Tf₂N], to lower the overall viscosity for gas separation units (Bara et al., 2009). Following the same principle, a mixture of alkanolamines with RTIL, which is less viscous, was also proposed to dramatically lower viscosity while increasing CO₂ capture capacity (Camper et al., 2008). These studies show promising potential to integrate ILs and other solvents to address the viscosity issue, and similar approaches to reduce the viscosity of TSIL have also been reported (Gurkan et al., 2010).

Regeneration of TSILs requires slightly more stringent conditions than RTILs (e.g. longer heat treatment in vacuum) since chemical interactions are involved in the capture process (Li et al., 2008). In general, these treatments enable the complete recycling of the ILs with little or negligible loss of capture capacity and material.

2.1.3 CO₂ Capture using Binding Organic Liquids and Reversible Ionic Liquids

Recently, a new class of CO₂ binding organic liquids, CO₂BOLs, was developed as a more efficient media to capture CO₂ than aqueous alkanolamines (Heldebrant et al., 2008). CO₂BOLs are organic liquids consisting of an alcohol and a strong amidine or guanidine base that can capture CO₂ chemically by forming amidinium or guanidinium alkylcarbonate (Liu et al., 2006). The schematic reactions of CO₂BOLs are shown in Figure 2-4. One of the most interesting features of CO₂BOLs is their low binding energy for CO₂, which allows them to be regenerated without significant energy consumption. Heldebrant et al. reported the free energies of CO₂BOLs for CO₂ capture and they found that the binding energies for CO₂ in the materials are notably small (Heldebrant et al., 2008). For example, the free energy of CO₂ binding in CO₂BOLs for DBU and Barton's base is ~ -9 kJ/mol and for TMG is ~ 2 kJ/mol. Since CO₂BOLs are liquid mixtures, no additional solvent is required. Thus, relatively high CO₂ capture capacity can be reached (up to 19 wt% and 147g/L for neat CO₂BOLs systems) (Heldebrant et al., 2009). Because the CO₂ binding energy of CO₂BOLs is small, a relatively low temperature swing process can be applied to regenerate them. A temperature swing process (up to 90 °C) was applied to explore their regeneration properties and in a 5-cycle test no visible loss of activity and selectivity of the CO₂BOLs were found.

Although the above mentioned literature on CO₂BOL is promising, regeneration process in presence of water presents an issue. If water is present in the system, the product becomes thermodynamically-favorable bicarbonate instead of an alkylcarbonate, therefore losing a certain amount of CO₂BOLs. Heldebrant et al. studied the robustness and recyclability of alkanolguanidines, alkanolamidines and mixtures of these two types of CO₂BOLs (Heldebrant et al., 2011). Regeneration of the materials was tested for 10 cycles via heat treatment at 75 °C

under a nitrogen atmosphere, in dry conditions or in the presence of 10 mol% water vapor. In both cases, the CO₂ uptake was not significantly decreased.

Considering this switchable chemistry, another new class of materials, referred to as RevILs, was developed by Blasucci et al (Blasucci et al., 2009). The switchable chemistry creates liquid materials reversible from a molecular liquid to an IL. The RevILs are distinguished from ILs or CO₂BOLs because they are composed of single component and are neutral. By adding an external compound (e.g. CO₂), the single type of molecular liquid of silylated amine molecules can be ionized to form ILs (Figure 2-5). The RevILs can also be easily switched back to molecular liquids by purging with an inert gas to remove CO₂, or heating up to 50 °C. The double-action solvents carry out CO₂ capture by reacting with CO₂ to form RevILs, and then using the RevILs for secondary CO₂ capture. A series of silylated amines were employed to form RevILs for CO₂ capture, including TMSA, TESA, TEtSA, and TPSA. The RevILs formed from these silylated amines all exhibit high CO₂ capture capacity, up to 20.2 mmol CO₂/g amine. (Blasucci et al., 2010) Studies reporting the potential regeneration of RevILs remain scarce. Blasucci et al. showed that heat treatment at 100 °C was sufficient to release all the captured CO₂ in TEtSAC, but the duration of the treatment as well as the need for vacuum was not specified.

2.2 Nanoparticle Organic Hybrid Materials (NOHMs)

NOHMs are organic–inorganic hybrid materials that consist of inorganic nanoparticles as cores and organic polymer chains as canopies. By selecting different materials of cores and polymers, NOHMs behave as glassy solids, gel or even free flowing liquids (Bourlinos 2005; Nugent et al., 2010). Earlier versions of the liquid-like Nanoparticle Organic Hybrid Materials (NOHMs) were referred to as NIMs (Nanoscale Ionic Materials), and were synthesized through the attachment of

a sulfonate terminated polymer onto a tertiary-amine functionalized nanoparticle (Bourlinos 2005; Bourlinos 2005; Bourlinos et al., 2005; Bourlinos et al., 2006). The second generation of NIMs was developed by switching the functional groups while using the same reaction schemes. More precisely, mono-amine terminated polyetheramine was grafted onto the sulfonate group functionalized nanoparticles, allowing a wider variety of polymer chains to be used as counter ions (Rodriguez 2008; Rodriguez et al., 2010).

Liquid-like NOHMs that exist in the absence of any solvent can exhibit several advantages compared to conventional colloidal suspensions (Rodriguez 2008). Firstly, the tethered polymers are ionically or covalently linked to the nanoparticles, whereas the suspension medium and the colloidal particles are physically discrete substances in the conventional colloidal systems. As a result, NOHMs exhibit different thermodynamic and scattering properties from the conventional colloidal systems. As a highly tunable hybrid material, NOHMs can be designed toward a specific application by selecting suitable cores and polymer chains. Finally, since the polymer chains are tethered by the cores via covalent bonding or ionic bonding to form a canopy, solvent loss in NOHMs can be prevented and NOHMs exhibit near zero vapor pressure. Moreover, as the canopy surrounding the core, CO₂ can be captured not only by the enthalpic effect via reactions with functional groups along the polymeric canopy but also by the entropic means via introduction of small gaseous molecules such as CO₂ to reduce the free energy of the frustrated canopy. These characteristics enable NOHMs to be a potential candidate for CO₂ capture.

2.3 Research Objectives

This dissertation represents the first attempt to investigate NOHMs for CO₂ capture. A broader definition of NOHMs was established as a new class of novel materials which were classified

based on their representative phases and synthesis methods. Both structural and chemical changes during their synthesis as well as CO₂ capture and solvent regeneration processes were explored. The key research questions that were addressed by this study include:

- Can the entropic effect be controlled by changing structures?
- Is there any in NOHMs? If so, what would be the effect of this structural difference between the unbound polymers and the tethered polymer chains on the CO₂ capture mechanisms and CO₂ capture capacities as well as the physical and chemical properties of NOHMs?
- Compared to their corresponding unbound polymers, would NOHMs have better thermal stability, which is important for the long term recyclability?
- Are there preferred functional groups for CO₂ capture? Can these task-specific functional groups be easily incorporated into the polymer chains? What would be the effect of these functional groups on the selectivity and recyclability of NOHMs?
- What other aspects should be considered in order to facilitate the implementation of using NOHMs for CO₂ capture?
- What other interesting physical and chemical properties of NOHMs that can be applied to energy and environmental technologies?

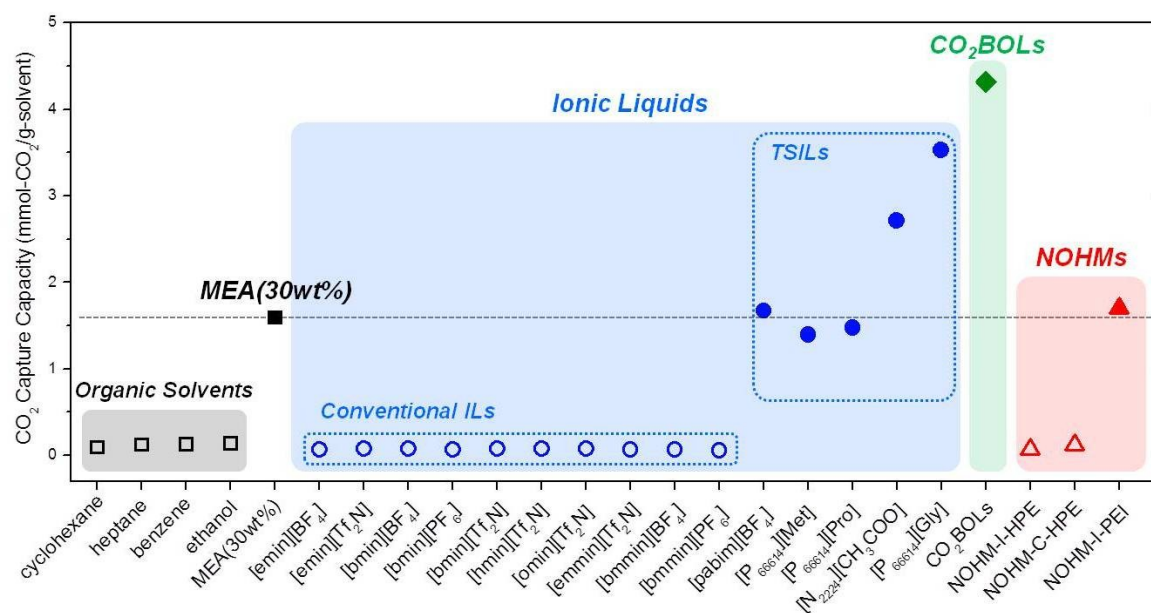


Figure 2-1 CO₂ capture capacities of liquid solvents at 0.1MPa and 25 °C.

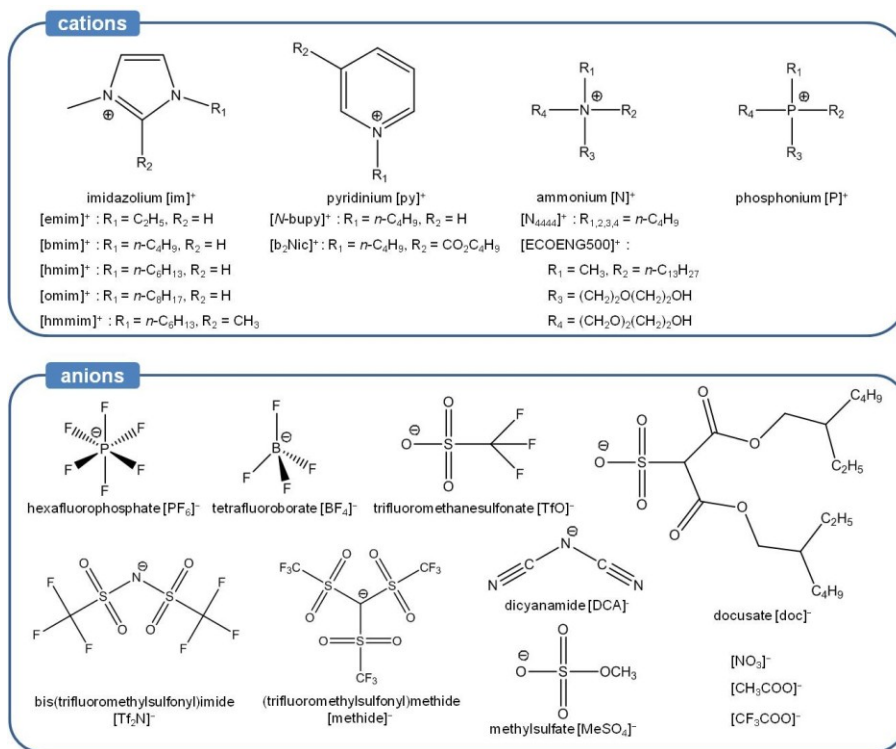


Figure 2-2 Structures of cations and anions of conventional ILs.

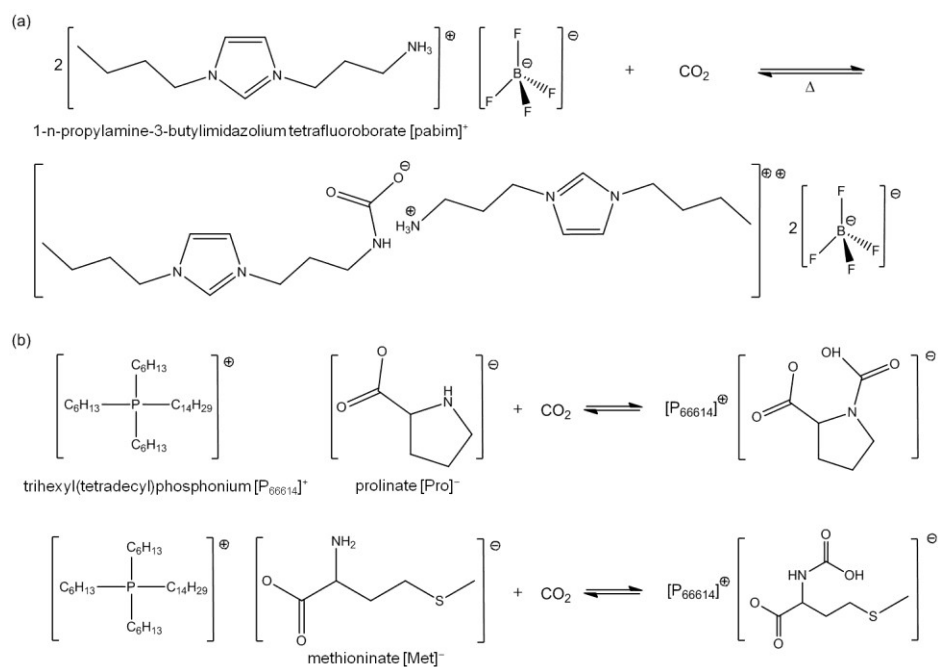


Figure 2-3 Reaction schematics of CO₂ with TSILs of (a) [pabim][BF₄] and (b) [P₆₆₆₁₄][Pro] and [P₆₆₆₁₄][Met].

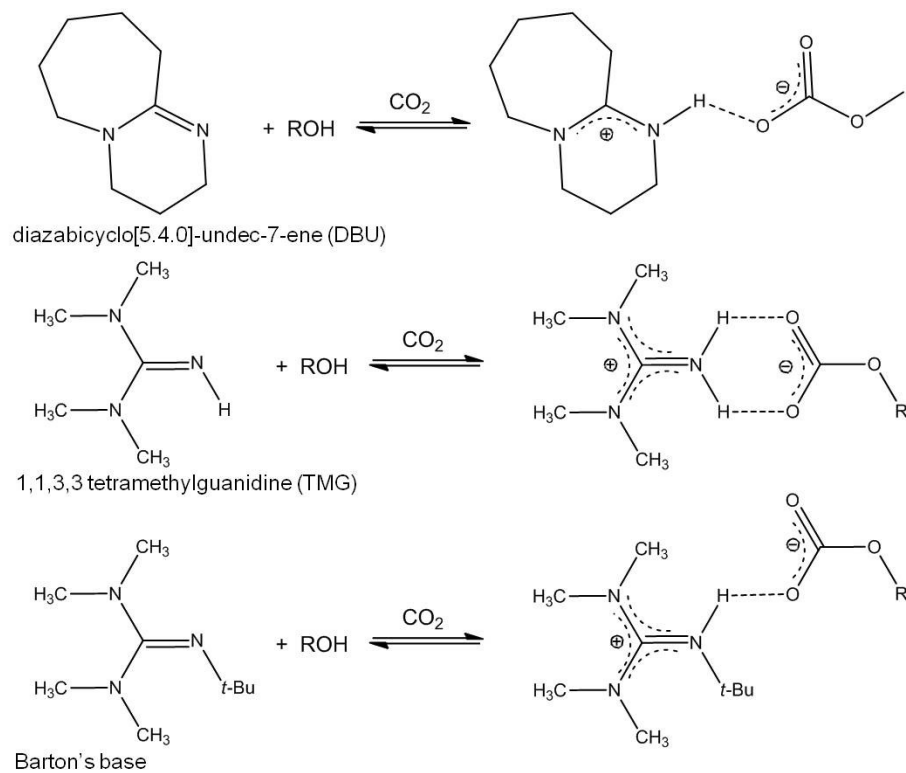


Figure 2-4 Proposed hydrogen bonding of cation with anion for salts made from DBU, TMG and Barton's base with ROH and CO₂.

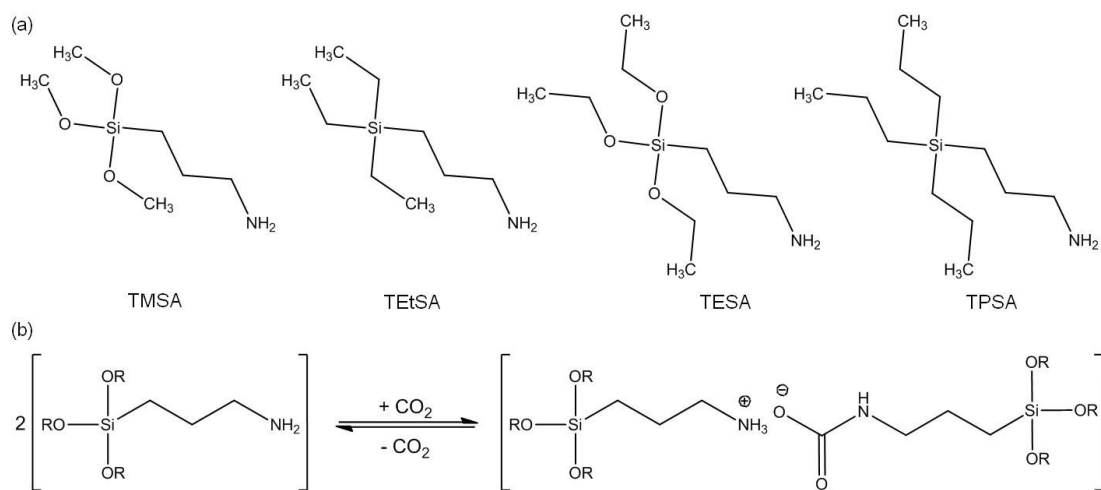


Figure 2-5 (a) Structures of RevILs: (3-aminopropyl)-trimethoxysilane (TMSA), (3-aminopropyl)-triethylsilane (TtEtSA), (3-aminopropyl)-triethoxysilane (TESA), and (3-aminopropyl)-tripropylsilane (TPSA), and (b) Reversible reaction of RevILs with carbon dioxide where R = methyl or ethyl.

Reference

- Agarwal, P., Qi, H. and Archer, L. A., "The Ages in a Self-Suspended Nanoparticle Liquid.", *Nano Lett.*, 10, 111-115, 2010.
- Aki, S. N. V. K. M., B. R.; Saurer, E. M.; Brennecke, J. F. , "High-Pressure Phase Behavior of Carbon Dioxide with Imidazolium-Based Ionic Liquids", *J. Phys. Chem. B*, 108, 20355-20365, 2004.
- Almantariotis, D., T. Gefflaut, et al., " Effect of Fluorination and Size of the Alkyl Side-Chain on the Solubility of Carbon Dioxide in 1-Alkyl-3-methylimidazolium Bis(trifluoromethylsulfonyl)amide Ionic Liquids" *J. Phys. Chem. B* 114(10), 3608–3617, 2010.
- Anderson, J. L., Dixon, J. K. and Brennecke, J. F., "Solubility of CO₂, CH₄, C₂H₆, C₂H₄, O₂, and N₂ in 1-Hexyl-3-methylpyridinium Bis(trifluoromethylsulfonyl)imide: Comparison to Other Ionic Liquids", *Accounts of Chemical Research*, 40, 1208-1216, 2007.
- Anthony, J. L., Maginn, E. J. and Brennecke, J. F., "Solubilities and Thermodynamic Properties of Gases in the Ionic Liquid 1-n-Butyl-3-methylimidazolium Hexafluorophosphate", *The Journal of Physical Chemistry B*, 106, 7315-7320, 2002.
- Anthony, J. L. A., J. L.; Maginn, E. J.; Brennecke, J. F. , "Anion Effects on Gas Solubility in Ionic Liquids", *J. Phys. Chem. B*, 109, 6366–6374, 2005.
- Anthony, J. L. A., S. N.V.K.; Maginn, E. J.; Brennecke, J. F. , "Feasibility of using ionic liquids for carbon dioxide capture", *Int. J. Environmental Technology and Management*, 4, 105-115, 2004.
- Bara, J. E., Camper, D. E., Gin, D. L. and Noble, R. D., "Room-Temperature Ionic Liquids and Composite Materials: Platform Technologies for CO₂ Capture", *Accounts of Chemical Research*, 43, 152-159, 2009.
- Bates, E. D. M., R. D.; Ntai, I.; Davis, J. H. Jr., "CO₂ Capture by a Task-Specific Ionic Liquid", *J. Am. Chem. Soc.*, 124, 926–927, 2002.
- Beckman, E. J., "A challenge for green chemistry: designing molecules that readily dissolve in carbon dioxide", *Chemical Communications*, 1885-1888, 2004.
- Blanchard, L. A., Gu, Z. and Brennecke, J. F., "High-Pressure Phase Behavior of Ionic Liquid/CO₂ Systems", *The Journal of Physical Chemistry B*, 105, 2437-2444, 2001.
- Blasucci, V., Dilek, C., Huttenhower, H., John, E., Llopis-Mestre, V., Pollet, P., Eckert, C. A. and Liotta, C. L., "One-component, switchable ionic liquids derived from siloxylated amines", *Chemical Communications*, 116-118, 2009.
- Blasucci, V., Hart, R., Mestre, V. L., Hahne, D. J., Burlager, M., Huttenhower, H., Thio, B. J. R., Pollet, P., Liotta, C. L. and Eckert, C. A., "Single component, reversible ionic liquids for energy applications", *Fuel*, 89, 1315-1319, 2010.
- Bounaceur, R., Lape, N., Roizard, D., Vallieres, C. and Favre, E., "Membrane processes for post-combustion carbon dioxide capture: A parametric study", *Energy*, 31, 2556-2570, 2006.
- Bourlinos, A. B., Chowdhury, S. R., Jiang, D. D., An, Y.-U., Zhang, Q., Archer, L. A. and Giannelis, E. P., "Layered Organosilicate Nanoparticles with Liquidlike Behavior", *Small*, 1, 80-82, 2005.

- Bourlinos, A. B., Chowdhury, S. R., Herrera, R., Chalkias, N., Jiang, D. D., Zhang, Q., Archer, L. A., Giannelis, E. P., "Functionalized Nanostructures with Liquid-Like Behavior: Expanding the Gallery of Available Nanostructures", *Adv. Funct. Mater.*, 15, 1285-1290, 2005.
- Bourlinos, A. B., Herrera, R., Chalkias, N., Jiang, D. D., Zhang, Q., Archer, L. A., Giannelis, E. P., "Surface-Functionalized Nanoparticles with Liquid-Like Behavior", *Adv. Mater.*, 17, 2005.
- Bourlinos, A. B., Stassinopoulos, A., Anglos, D., Herrera, R., Anastasiadis, S., Petridis, D. and Giannelis, E. P., "Functionalized ZnO Nanoparticles with Liquidlike Behavior and their Photoluminescence Properties", *Small*, 2, 513–516, 2006.
- Bourlinos, A. B. H., R.; Chalkias, N.; Jiang, D. D.; Zhang, Q.; Archer, L. A.; Giannelis, E. P., "Surface-Functionalized Nanoparticles with Liquid-Like Behavior", *Adv. Mater.*, 17, 2005.
- Cadena, C., Anthony, J. L., Shah, J. K., Morrow, T. I., Brennecke, J. F. and Maginn, E. J., "Why Is CO₂ So Soluble in Imidazolium-Based Ionic Liquids?", *Journal of the American Chemical Society*, 126, 5300-5308, 2004.
- Camper, D., Bara, J. E., Gin, D. L. and Noble, R. D., "Room-Temperature Ionic Liquid–Amine Solutions: Tunable Solvents for Efficient and Reversible Capture of CO₂", *Industrial & Engineering Chemistry Research*, 47, 8496-8498, 2008.
- Choi, S., Drese, J. H. and Jones, C. W., "Adsorbent Materials for Carbon Dioxide Capture from Large Anthropogenic Point Sources", *ChemSusChem*, 2, 796-854, 2009.
- Chue, K. T., Kim, J. N., Yoo, Y. J., Cho, S. H. and Yang, R. T., "Comparison of Activated Carbon and Zeolite 13X for CO₂ Recovery from Flue Gas by Pressure Swing Adsorption", *Industrial & Engineering Chemistry Research*, 34, 591-598, 1995.
- Crosthwaite, J. M., Muldoon, M. J., Dixon, J. K., Anderson, J. L. and Brennecke, J. F., "Phase transition and decomposition temperatures, heat capacities and viscosities of pyridinium ionic liquids", *The Journal of Chemical Thermodynamics*, 37, 559-568, 2005.
- Ghosal, K., Chern, R. T., Freeman, B. D., Daly, W. H. and Negulescu, I. I., "Effect of Basic Substituents on Gas Sorption and Permeation in Polysulfone", *Macromolecules*, 29, 4360-4369, 1996.
- Goodrich, B. F., de la Fuente, J. C., Gurkan, B. E., Zadigian, D. J., Price, E. A., Huang, Y. and Brennecke, J. F., "Experimental Measurements of Amine-Functionalized Anion-Tethered Ionic Liquids with Carbon Dioxide", *Industrial & Engineering Chemistry Research*, 50, 111-118, 2010.
- Gurkan, B. E., de la Fuente, J. C., Mindrup, E. M., Ficke, L. E., Goodrich, B. F., Price, E. A., Schneider, W. F. and Brennecke, J. F., "Equimolar CO₂ Absorption by Anion-Functionalized Ionic Liquids", *Journal of the American Chemical Society*, 132, 2116-2117, 2010.
- Gutowski, K. E. and Maginn, E. J., "Amine-Functionalized Task-Specific Ionic Liquids: A Mechanistic Explanation for the Dramatic Increase in Viscosity upon Complexation with

- CO₂ from Molecular Simulation", *Journal of the American Chemical Society*, 130, 14690-14704, 2008.
- Headley, A. D. and Ni, B., "Chiral imidazolium ionic liquids: their synthesis and influence on the outcome of organic reactions", *Aldrichimica Acta* 40, 107-117, 2007.
- Heldebrant, D. J., Koech, P. K., Rainbolt, J. E., Zheng, F., Smurthwaite, T., Freeman, C. J., Oss, M. and Leito, I., "Performance of single-component CO₂-binding organic liquids (CO₂BOLs) for post combustion CO₂ capture", *Chemical Engineering Journal*, 171, 794-800, 2011.
- Heldebrant, D. J., Yonker, C. R., Jessop, P. G. and Phan, L., "Organic liquid CO₂ capture agents with high gravimetric CO₂ capacity", *Energy & Environmental Science*, 1, 487-493, 2008.
- Heldebrant, D. J., Yonker, C. R., Jessop, P. G. and Phan, L., "CO₂ -binding organic liquids (CO₂ BOLs) for post-combustion CO₂ capture", *Energy Procedia*, 1, 1187-1195, 2009.
- Hou, Y. and Baltus, R. E., "Experimental Measurement of the Solubility and Diffusivity of CO₂ in Room-Temperature Ionic Liquids Using a Transient Thin-Liquid-Film Method", *Industrial & Engineering Chemistry Research*, 46, 8166-8175, 2007.
- Jacquemin, J., Husson, P., Mayer, V. and Cibulka, I., "High-Pressure Volumetric Properties of Imidazolium-Based Ionic Liquids: Effect of the Anion", *Journal of Chemical & Engineering Data*, 52, 2204-2211, 2007.
- Kazarian, S. G., Briscoe, B. J. and Welton, T., "Combining ionic liquids and supercritical fluids: ATR-IR study of CO₂ dissolved in two ionic liquids at high pressures", *Chemical Communications*, 2047-2048, 2000.
- Kim, I. and Svendsen, H. F., "Comparative study of the heats of absorption of post-combustion CO₂ absorbents", *International Journal of Greenhouse Gas Control*, 5, 390-395, 2011.
- Kim, T.-J., Li, B. and Hägg, M.-B., "Novel fixed-site-carrier polyvinylamine membrane for carbon dioxide capture", *Journal of Polymer Science Part B: Polymer Physics*, 42, 4326-4336, 2004.
- Kroon, M. C., Shariati, A., Costantini, M., van Spronsen, J., Witkamp, G.-J., Sheldon, R. A. and Peters, C. J., "High-Pressure Phase Behavior of Systems with Ionic Liquids: Part V. The Binary System Carbon Dioxide + 1-Butyl-3-methylimidazolium Tetrafluoroborate", *Journal of Chemical & Engineering Data*, 50, 173-176, 2004.
- Li, X., Hou, M., Zhang, Z., Han, B., Yang, G., Wang, X. and Zou, L., "Absorption of CO₂ by ionic liquid/polyethylene glycol mixture and the thermodynamic parameters", *Green Chemistry*, 10, 879-884, 2008.
- Lin, K.-Y. A. and Park, A.-H. A., "Effects of Bonding Types and Functional Groups on CO₂ Capture using Novel Multiphase Systems of Liquid-like Nanoparticle Organic Hybrid Materials", *Environmental Science & Technology*, 45, 6633-6639, 2011.
- Liu, Y., Jessop, P. G., Cunningham, M., Eckert, C. A. and Liotta, C. L., "Switchable Surfactants", *Science*, 313, 958-960, 2006.

- MacDowell, N., Florin, N., Buchard, A., Hallett, J., Galindo, A., Jackson, G., Adjiman, C. S., Williams, C. K., Shah, N. and Fennell, P., "An overview of CO₂ capture technologies", *Energy Environ Sci* 3, 1645–1669 2010.
- Mahurin, S. M., Lee, J. S., Baker, G. A., Luo, H. and Dai, S., "Performance of nitrile-containing anions in task-specific ionic liquids for improved CO₂/N₂ separation", *J Membr Sci* 353, 177-183, 2010.
- Muldoon, M. J., Aki, S. N. V. K., Anderson, J. L., Dixon, J. K. and Brennecke, J. F., "Improving Carbon Dioxide Solubility in Ionic Liquids", *The Journal of Physical Chemistry B*, 111, 9001-9009, 2007.
- Nugent, J. L., Moganty, S. S. and Archer, L. A., "Nanoscale Organic Hybrid Electrolytes", *Advanced Materials*, 22, 3677-3680, 2010.
- Paulechka, Y. U., Kabo, G. J., Blokhin, A. V. and Vydrov, O. A. " Thermodynamic Properties of 1-Butyl-3-methylimidazolium Hexafluorophosphate in the Ideal Gas State." *J. Chem. Eng. Data*, 48(3), 457-462, 2003.
- Raveendran, P. and Wallen, S. L., "Exploring CO₂-Philicity: Effects of Stepwise Fluorination", *The Journal of Physical Chemistry B*, 107, 1473-1477, 2003.
- Rinker, E. B., Ashour, S. S. and Sandall, O. C., "Absorption of carbon dioxide into aqueous blends of diethanolamine and methyldiethanolamine", *Ind Eng Chem Res* 39, 4346–4356 2000.
- Rochelle, G. T., "Amine Scrubbing for CO₂ Capture", *Science* 325, 1652–1654, 2009.
- Rodriguez, R., Herrera, R., Bourlinos, A. B., Li, R., Amassian, A., Archer, L. A. and Giannelis, E. P., "The synthesis and properties of nanoscale ionic materials", *Applied Organometallic Chemistry*, 24, 581–589, 2010.
- Rodriguez, R., Herrera, R., Archer, L. A., Giannelis, E. P., "Nanoscale Ionic Materials", *Adv. Mater.*, 20, 4353-4358, 2008.
- Soutullo, M. D., Odom, C. I., Wicker, B. F., Henderson, C. N., Stenson, A. C. and Davis, J. H., "Reversible CO₂ Capture by Unexpected Plastic-, Resin-, and Gel-like Ionic Soft Materials Discovered during the Combi-Click Generation of a TSIL Library", *Chemistry of Materials*, 19, 3581-3583, 2007.
- Wang, G., Hou, W., Xiao, F., Geng, J., Wu, Y. and Zhang, Z., "Low-Viscosity Triethylbutylammonium Acetate as a Task-Specific Ionic Liquid for Reversible CO₂ Absorption", *Journal of Chemical & Engineering Data*, 56, 1125-1133, 2011.
- Yu, G., Zhang, S., Zhou, G., Liu, X. and Chen, X., "Structure, interaction and property of amino-functionalized imidazolium ILs by molecular dynamics simulation and Ab initio calculation", *AIChE Journal*, 53, 3210-3221, 2007.
- Zhang, S., Chen, Y., Ren, R. X. F., Zhang, Y., Zhang, J. and Zhang, X., "Solubility of CO₂ in Sulfonate Ionic Liquids at High Pressure", *Journal of Chemical & Engineering Data*, 50, 230-233, 2004.

CHAPTER 3

DESIGN AND SYNTHESIS OF NANOPARTICLE ORGANIC HYBRID MATERIALS (NOHMs)

This chapter is based on the following publications:

Y. Park, J. Decatur, **K.-Y. A. Lin** and A.-H. A. Park, “Structure Characterization and Specific Intermolecular Interaction of Liquid-like Nanoparticle Organic Hybrid Materials for Carbon Dioxide Capture”, *Physical Chemistry Chemical Physics*, 13, 18115-18122, 2011.

Y. Park, D. Shin, Y. N. Jang and A.-H. A. Park, “Carbon Dioxide Capture Capacity and Swelling Measurements of Liquid-like Nanoparticle Organic Hybrid Materials via Attenuated Total Reflectance Fourier Transform Infrared Spectroscopy”, *Journal of Chemical & Engineering Data*, 57 (1), 40-45, 2011.

The manuscript in preparation:

C. Petit, **K.-Y. A. Lin** and A.-H. A. Park, “Design and Synthesis of POSS-based Hybrid Nanomaterials via Ionic Bonding and Their Interactions with Carbon Dioxide”, 2012.

3.1 Synthesis and Characterization of NOHMs

3.1.1 Classification of NOHMs

NOHMs can be classified based on their representative phase and synthesis methods as well as the existence of task-specific functional groups. As shown in Figure 3-1, NOHMs are first classified based on the representative phase (i.e. liquid-like vs solid hybrids). In this dissertation, mainly the liquid-like NOHMs are synthesized and evaluated for CO₂ capture. Specifically, the nomenclature of NOHMs is designed so that it denotes “NOHM-bonding type-description of polymeric chain including the existence of functional groups.” For example, the second term, “I” and “C”, represents ionic and covalent bonds, respectively. Five examples of NOHMs are listed in Figure 3-1. NOHM-I-HPE represents NOHMs prepared via ionic bonding with a HPE polymer, which indicates PolyEther with high amount of ether groups. On the other hand, NOHM-C-HPE represents a NOHMs prepared via covalent bonding with the HPE polymer. MPE indicate polyether with moderate amount of ether groups, while “t” denotes “tertiary” amine groups.

3.1.2 Synthesis Methods

According to the classification shown in Figure 3-1, NOHMs can be prepared through several approaches. However, the strategy for the preparation of NOHMs is similar in each case. First, nanoparticles are modified with certain functional groups. The functionalization can be obtained by adding a linker (e.g. coupling agents, also called as corona) on the surface of the nanoparticles. Then, a layer of polymer is grafted on the nanoparticles through ionic/covalent bonding. The polymer and the linker (if used) together are referred as the “Canopy”. The molecular weights of polymers, physical property of polymers and sizes of nanoparticles are design parameters

required to make liquid-like NOHMs. Generally, when the size of the nanoparticles is within 7 nm - 22 nm (diameter), the molecular weight of the polymer (e.g. polyethylene glycol) should be at least 1000 g/mol to ensure the liquid-like state of the resulting NOHMs.

Figure 3-2 shows the procedure to synthesize NOHMs through ionic bonding. A nanoparticle is functionalized with a linker, a silane with sulfonic acid, thereby introducing sulfonate groups onto the nanoparticle surface. An amine-terminated polymer is grafted onto the modified nanoparticle through an acid-base reaction.

3.1.3 Physical and Chemical Characterizations of NOHMs

In NOHMs, the polymer is grafted onto the nanoparticles through the reaction between the functional group of nanoparticles and the functional group of the polymer through ionic or covalent bonding. Thus, the bond formation (ionic or covalent) can be confirmed by the conversion of functional groups.

Such a conversion of the functional groups can be observed via molecular spectroscopy instruments, including Fourier Transfer Infrared (FTIR) Spectrometer, a Raman Spectrometer, and a Nuclear Magnetic Resonance (NMR). Specifically, an Attenuated Total Reflectance (ATR) accessory will be used to determine the conversion of functional groups. ATR can enable NOHMs to be examined directly in the liquid state without further preparation. Raman Spectrometry also can provide supplementary information to FTIR, since Raman can measure vibrational, rotational, and other low-frequency modes in a system. NMR is also used to verify the conversion of functional groups as well as the structural information.

Additionally, the successful synthesis of NOHMs also results in polymers wrapping the nanoparticles. The layer of polymer can avoid the agglomeration of nanoparticles and make

nanoparticles self-suspended in the polymer medium. In order to observe such a pattern, Transmission Electron Microscopy (TEM) will be used to analyze the nanoscale configuration of NOHMs. For TEM measurement, NOHMs samples are required to be transparent to let the light beam pass through (Figure 3-3).

3.2 Structural Analysis of NOHMs

In order to verify the structure of NOHMs, 2D NMR spectra were obtained. Figure 3-4 shows a 2D ^1H - ^{13}C edited HSQC (Heteronuclear Single Quantum Coherence) NMR spectra of pure Polyetheramine with MW 600 (M-600) and its corresponding NOHMs. The edited HSQC experiments correlate the chemical shift of a proton with the chemical shift of a directly bonded carbon. The phase indicates its multiplicity. Methine and methyl peaks are shown in red while the methylene peaks are shown in blue. Together with ^1H - ^1H COSY, the proton and carbon peaks were assigned as shown in Figure 3-4(a). There were several differences between the spectra of Polyetheramine M-600 and NOHM-I-PE600. In Polyetheramine M-600 spectra, two distinct doublets assigned to two methyl groups, H6 ($\delta = 1.05$ ppm, $J = 6.3$ Hz) and H9 ($\delta = 0.91$ ppm, $J = 6.4$ Hz) were observed. However, in NOHM-I-PE600, the proton and carbon shifts of these methyls became very similar to $\delta_{\text{H}} = 1.05$ ppm. This downfield shift of H9 suggests formation of ionic bond between the surface-modified SiO_2 core and primary amine of polyetheramine due to the oxygens in the sulfonate group deshielding the adjacent protons. Compared to Polyetheramine M-600, NOHM-I-PE600 spectra showed significant differences. The proton shifts of both (H7, C7) methylene and (H8, C8) methine, which are adjacent to nitrogen, were shifted downfield. It is speculated that the proximity of ionic bonding has induced the large shifts. FT-IR

spectroscopy in Figure 3-4(b) was also used to infer if an ionic bond was formed and to observe the asymmetric (δ_a) and symmetric bends (δ_s) of $-\text{NH}_3^+$ of NOHM-I-PE600 at 1630 cm^{-1} and 1530 cm^{-1} , respectively. Although additional studies may require to verify the formation of ionic bonding, the polymer chain did not detach from the core in the presence of solvents such as water.

The conformational behavior of the canopy in NOHMs was investigated by 2D ROESY (Rotating-frame Overhauser Effect Spectroscopy) NMR experiments providing information regarding interchain and intrachain interactions within the polymeric canopy. The heteronuclear NMR spectroscopic technique using 2D ROESY employs a second frequency dimension based on the Nuclear Overhauser Enhancement (NOE) effect in which correlations are seen between nuclei that are spatially proximate within a molecule. The Polyetheramine with MW 2000 (Jeffamine M-2070, called PE2070 or HPE abbreviately) exhibits below or near entanglement limit ($M_e = 1600 - 2200\text{ g/mol}$ for PEO; $M_e = 1287\text{ g/mol}$ for PPO) (Jespersen et al., 2010). Thus in the neat Polyetheramine M-2070, certain amounts of chain coiling may occur. In NOHMs, however, it is possible that the corona and their associated counterion species are stretched out due to the steric considerations – the tethered canopy must fill the space between nano-sized cores.

When the polyetheramine chains are coiled, ROEs (Rotating-frame Overhauser Effects) may potentially be observed between protons on opposite ends of the chains, such as between protons H1 and H8 or H9. The ROESY experiments theoretically should be able to confirm this behavior (Huang et al., 2002). In NOHMs, such ROEs should be absent or be of small intensity. In practice, observing ROEs in polyetheramines of NOHMs is very difficult due to severe proton overlap in the standard ROESY spectra. HSQC-ROE methods were then

attempted, which provided the requisite spectra, but suffered from poor signal-to-noise ratio. The conformational details of NOHMs packing may be important for understanding the mechanisms of CO₂ capture and such details will be subjected to future investigations.

In order to identify the CO₂ capture mechanism in NOHMs, FT-IR spectra were obtained by employing ATR technique. ATR FT-IR spectroscopy (shown in Figure 3-5), which provides a small path length of incident infrared beam, is a promising technique to investigate the intermolecular interaction of specimens in highly absorbent media. For the measurements, NOHMs samples were prepared in thin layers on the diamond crystal and the sample cell was pressurized with CO₂. As shown in Figure 3-6, two distinct peaks of asymmetric stretching (ν_3 at 2335 cm⁻¹) and bending mode ($\nu_2 \sim 659$ cm⁻¹) of NOHMs-absorbed CO₂ were found. Aside from the CO₂ bands, the rest of the peaks showed trends of decreasing intensity with increasing CO₂ pressure. This trend may be caused by the increased in NOHMs' volume as it absorbs more CO₂ (Munoz et al., 2009; Rainbolt et al., 2011). In the C–O stretching bend, a noticeable peak shift to a higher frequency was observed while ν_3 did not show a significant peak shift. The continuous peak shift of stretching modes to a higher wavenumber as more CO₂ gas is introduced to the system indicates the decreased interaction of the canopy chains with their environment due to the liquid phase density decrease (Aaron and Tsouris 2005; Barzagli et al., 2010).

Figure 3-7 (a) exhibits the ν_2 bending mode of CO₂ absorbed in NOHM-I-PE2070. The peaks shape significantly differs from that of pure CO₂ in vapor phase which shows as a sharp single peak at 668 cm⁻¹. This illustrates the occurrence of specific intermolecular interaction between CO₂ and NOHM-I-PE2070. It is known that specific functional groups such as a carbonyl group, can act as an electron-donor for CO₂ by Lewis acid-base

interaction (Wang et al., 2011). Similarly, specific functional groups on NOHMs, such as ether, can be the basic sites for CO₂ by Lewis acid-base interactions (Belmabkhout et al., 2009). Thus, the double degeneracy of ν_2 bends could be removed. Finally two deconvoluted peaks of 661 cm⁻¹ (out-plane mode) and 650 cm⁻¹ (in-plane mode) of CO₂ were observed.

In addition, it has been found that the anions also play a significant role in allowing ionic liquids (ILs) to have a high solubility of CO₂ (Belmabkhout and Sayari 2009). Investigation by Kazarian et al. on the molecular interactions between CO₂ and several types of anions on ILs reported the occurrences of weak Lewis interaction between anions and CO₂ (Qi et al., 2011). With these findings, it can be inferred that the anionic sites between counterion species and corona could form weak Lewis interactions with CO₂.

On the other hand, slight change of shape of the ν_2 band peaks were noticed as the pressure was increased. In Figure 3-7(b) the overall shift of the doublet toward the higher frequency region can be seen. It also suggests that with the increase in pressure, the mobility of polymer chains increase and disrupt the CO₂ alignment at the ether-absorbing site (Wang et al., 2011).

CO₂ capture capacity of NOHMs was obtained from the ATR FT-IR spectra. In order to calculate the CO₂ capture capacity, the Beer–Lambert law which expresses the relationship between the absorbance (A), the absorptivity (ϵ), the concentration (c), and the infrared path length (d) was used. For transmission measurement, the path length is identical to the thickness of the specimen. In ATR FT-IR spectroscopy, however, the internal reflection at the interface between a crystal and the specimen causes an evanescent electric field which undergoes exponential decay in its intensity, and thus effective thickness of the evanescent wave (d_e) should be considered. The Beer–Lambert law is described as

$$A = \varepsilon \cdot c \cdot d_e \quad (3-1)$$

where the d_e is the arithmetical mean between the effective path length for perpendicular ($d_{e\perp}$) and parallel ($d_{e\parallel}$) polarization. In order to calculate d_e , the refractive index of NOHM-I-PE2070 ($n_D = 1.52$) was measured by employing an ellipsometry and a refractometer. The absorbance of CO₂ was quantified by measuring the intensity of the ν_3 band, and its molar absorptivity at high-pressure was $1.0 \times 10^6 \text{ cm}^2/\text{mol}$. The degree of swelling (S) of NOHMs was calculated by

$$S = \frac{A^0}{A} \cdot \frac{d_e}{d_e^0} - 1 \quad (3-2)$$

where A^0 , d_e^0 , A , and d_e are the absorbance and the effective path length with and without CO₂ pressure, respectively. In order to measure the degree of swelling, absorbance of C–O stretching band around 1100 cm^{-1} was selected by assuming that the absorptivity is not significantly affected by the concentration of CO₂ in different pressures, and thus the change of effective thickness was considered negligible (Aaron and Tsouris 2005). The absorbance before and after exposure to CO₂ was integrated in the interval from 1000 cm^{-1} to 1200 cm^{-1} .

Figure 3-8(a) exhibits CO₂ capture capacity of canopy in NOHM-I-PE2070 as a function of pressure. Since the silica nanoparticles used in the synthesis of NOHMs were nonporous (Meeks, Rankin et al. 2010), the CO₂ capture capacity was only calculated based on the organic content of NOHMs (i.e., the canopy). Compared to the CO₂ capacity of pure Polyetheramine M-2070, the CO₂ capture capacity of NOHMs is higher by 5 ~ 10%. It is speculated that the enhanced CO₂ capture capacity is a result of NOHMs' unique structure; the more orderly structure of NOHMs compared to that of pure polymer could offer unoccupied spaces and thus introducing CO₂ molecules could reduce the free energy.

Figure 3-8(b) shows the CO₂ capture capacity of NOHMs and its pure corona species as a function of swelling during CO₂ capture. In case of NOHM-I-PE2070, less volume change was observed than for pure counterion species at the same CO₂ capture capacity. It can be explained that because the corona matrix of NOHMs is more frustrated structure than pure polymeric counterion species, a smaller swelling ratio was observed.

3.3 POSS-based Nanoparticle Organic Hybrid Materials

Beside regular nanoparticles (5-50 nm), Polyhedral oligomeric silsesquioxane (POSS) units appear as interesting candidates for NOHMs' synthesis due to their extremely small size. POSS represents a nanometer-size silica-based compound with the formula (RSiO_{3/2})₈, where R can be a hydrogen atom, or any polar or non-polar organic molecule (Li et al., 2001; Cordes et al., 2010). POSS exhibits a rigid cage-like structure which usually consists of a 1-nm cube with silicon atoms on the corners linked to organic arms (or hydrogen atoms) (Li et al., 2001; Cordes et al., 2010). It is common to refer to POSS as the smallest silica nanoparticle. Owing to the hybrid nature of POSS, these materials can serve to design NOHMs with favorable properties. Indeed, considering the inorganic portion (silica), enhanced thermal stability is expected as suggested by previous studies on POSS/polymer composites (Chang et al., 2007; Subianto et al., 2009; Tanaka et al., 2010). Moreover, via proper selection of the organic arms, it is possible to graft polymer chains on POSS, thereby forming new NOHMs structures. Finally, the small inorganic cages in POSS should minimize the unused portion of NOHMs for CO₂ capture. In fact, since the POSS cages are void and their size exceeds that of CO₂ molecule (3.3 Å) (Li et al., 2009), it is expected that they can accommodate molecules of this gas. Recently solid membranes consisting of

POSS/polymer composites have been reported for their use in CO₂ removal and CO₂/N₂ and CO₂/H₂ separations.

3.3.1 Synthesis of POSS-based NOHMs

Three POSS-based NOHMs with ionic bonding were synthesized. First, a 11 wt% aqueous solution of octaammonium POSS (Hybrid Plastics) was prepared. An ion exchange resin (DowexTM A OH, Sigma-Aldrich) was then employed to remove the chloride ions from the POSS units and neutralize the amine groups. Next, three different polymers, namely, two glycolic acid ethoxylate lauryl ether (Sigma Aldrich, MW 460 and 740) and one poly(ethylene glycol) 4-nonylphenyl 3-sulfopropyl ether potassium salt (Sigma Aldrich, MW 1260), were diluted with deionized water to obtain three 10 wt% polymeric solutions. In the case of the latter polymer, an ion exchange resin (DowexTM HCR W2, Sigma-Aldrich) was then employed to remove the potassium ions and protonate the sulfonate groups. Each polymer solution was added dropwise to a portion of the POSS solution while monitoring the pH. Addition was stopped when reaching the equivalence point indicating the neutralization of the POSS amine groups by the acidic groups (carboxylic or sulfonic) of the polymers. Finally, the samples were dried, first in air at ambient temperature to evaporate most of the water, and then under reduced pressure at 40 °C for about 48 hours.

NOHMs samples are referred to as POSS-I-PC_{*n*} or POSS-I-PS_{*n*}, where *n* corresponds to the molecular weight of the polymer (*n* = 460, 740 or 1260). “I” stands for “Ionic” and indicates the type of bonding between the POSS unit and the polymer chains, while “PC” and “PS” refer to polymer (“P”) with carboxylic (“C”) and sulfonic (“S”) end groups, respectively. From this point on, the octaammonium POSS will be referred to as POSS (N), and the polymers as PC460,

PC740 and PS1260, following the same nomenclature as described above. The schematic structures of the synthesized NOHMs and the parent materials are shown in Table 3-1.

Two POSS-based NOHMs with covalent bonding were synthesized. 0.5 g of the POSS Octa(dimethylsiloxo)silsesquioxane (Hybrid Plastics) was dissolved in anhydrous toluene in a 100 mL round-bottom flask under a flow of argon. 1.1 g of polyethylene glycol monoallyl ether (Clariant GmbH, MW 250) was added to the POSS solution. Karstedt's catalyst [Pt(dvs)] (2 mL of 2 mmol solution in toluene, Gelest) was added, and temperature of the mixture was increased temperature to 35 °C and stirred for 48 hours. Completion of the hydrosilylation reaction was verified by observing the disappearance of the Si-H proton shift (4.72 ppm) by ^1H NMR. The mixture then was concentrated under reduced pressure to remove the solvent. Another POSS-based NOHMs was used with the same method and with diethylene glycol monovinyl ether was incorporated to form the canopy (Sigma-Aldrich, MW 130).

NOHMs samples are referred to as POSS-C-PEG n , where n corresponds to the molecular weight of the polymer ($n = 130$ or 250). "C" stands for "Covalent" and indicates the type of bonding between the POSS unit and the polymer chains, while "PEG" refers to polyethylene glycol. In the following, the octasilane POSS will be referred to as POSS (SiH), and the polymers as PEG130 and PEG250. The schematic structures of the synthesized NOHMs and the parent materials are shown in Table 3-1.

3.3.2 Characterization of POSS-based NOHMs

Thermal stability is an important aspect of CO₂ absorption processes since regeneration of the absorbent is usually achieved via temperature swing. Considering this aspect as well as the objective of this study to investigate the potential of POSS-based NOHMs for CO₂ removal,

thermogravimetric analyses were performed. The results are presented in Figure 3-9. As previously hypothesized, the presence of the POSS units visibly enhanced the thermostability of the hybrid materials compared to that of the pure polymers. This improvement was more pronounced for the covalently bonded POSS-based NOHMs. As explained in a previous study, this effect must be related to the shorter polymer chain size of the POSS-C-PEG n materials (Lin et al., 2011). Despite the greater enhancement in thermostability for the POSS-C-PEG n materials with regards to the corresponding unbound polymers, the POSS-based NOHMs with ionic bonding overall exhibited a slightly higher temperature of decomposition (as measured at the point of 50% mass loss). Overall, the thermostability enhancement was not compromised by the reduction of size, and sometimes of content, of the inorganic core when using POSS instead of regular silica nanoparticles.

Before discussing in more detail the properties of the POSS-based NOHMs, it is important to confirm the successful synthesis of these materials. Towards this end, structural characterization was performed using ^1H NMR and/or ATR FT-IR spectroscopy. The ^1H NMR spectra of POSS-I-PC740 and its corresponding parent materials are presented in Figure 3-10, as representative examples of the POSS-based NOHMs that are in the ionic bonding category. POSS (N) spectrum exhibits three peaks related to the H atoms from the three CH_2 on the organic arms of the POSS (see Table 3-1). The one at 0.80 ppm corresponds to H atoms from CH_2 next to the Si atom while that at 3 ppm corresponds to H atoms from CH_2 next to the amine group.

The main features of the spectrum of PC740 are the two peaks at 1.25 ppm and 3.65 ppm which are related to the H atoms on the purely alkane part of the polymer and the polyethylene oxide portion, respectively. On the spectrum of POSS-I-PC740, the features of both POSS (N) and PC740 are found, confirming the presence of the two unaltered components. The ^1H NMR

spectrum of POSS(SiH) has two peaks at 0.35 ppm and 4.75 ppm related to the H atoms from the CH₃ groups and the H atom directly linked to Si atoms, respectively. The ¹H NMR spectrum of POSS-C-PEG250 exhibits the peaks of both POSS (SiH) and PEG250. However the peak at 4.75 ppm from the POSS is missing which confirms that the allyl PEG250 covalently bonded the POSS unit by replacing the H atoms initially linked to the Si atoms.

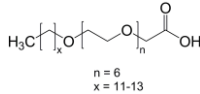
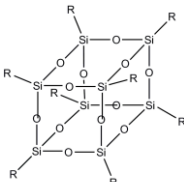
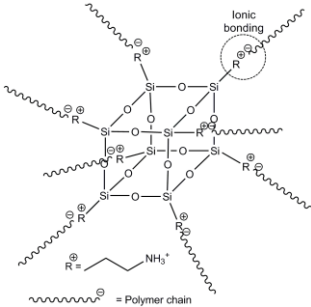
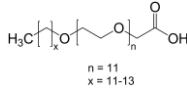
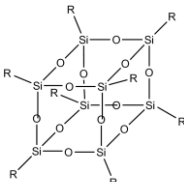
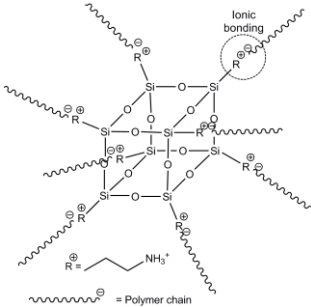
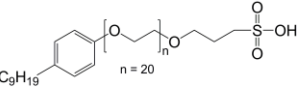
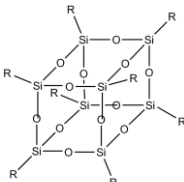
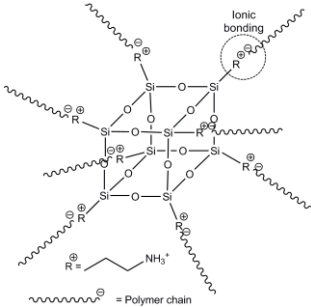
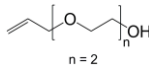
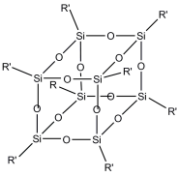
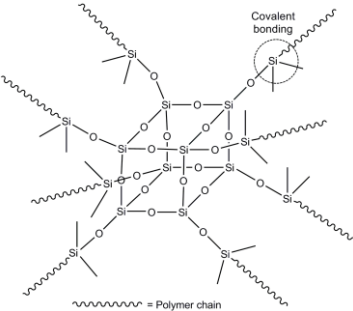
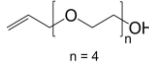
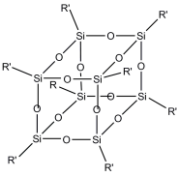
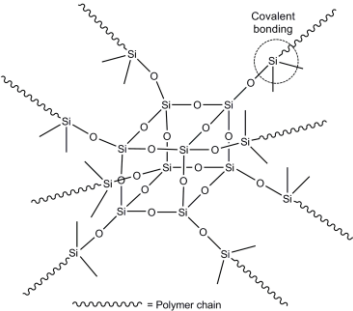
Evidences for the reaction between the POSS and the polymers in the POSS-based NOHMs with ionic bonding are provided by FT-IR spectroscopy (Figure 3-11). The spectra of all the pure polymers were very similar, and the main vibration bands included: C–O stretching (1090 cm⁻¹), CH₂ symmetric and asymmetric stretching (2860 cm⁻¹ and 2930 cm⁻¹), and O–H stretching from water (3450 cm⁻¹) (Lide 1993). As expected, the spectra of NOHMs exhibited similar features to those of the pure polymers. However, some differences existed and indicated the presence of POSS (i.e., silica). For instance, the band at ~ 1090 cm⁻¹ was broader due to the overlap with the Si-O-Si stretching band, and S=O vibration for POSS-I-PS1260 (Chen and Iroh 1999; Smith 1999). Moreover, the C=O stretching band from the carboxyl groups appeared at 1740 cm⁻¹ in the spectra of PC460 and PC760, indicating that these functional groups were in their acidic form (Cabaniss et al., 1998). In POSS-I-PC460 and POSS-I-PC740, this band was shifted to 1580 cm⁻¹, indicating that the carboxyl groups were now in their basic form (Cabaniss et al., 1998). This observation confirms the acid-base reaction and the formation of ionic bonding between the amine groups of the POSS and the carboxylic groups of the polymers. For POSS-I-PS1260, such observation was unfortunately not possible since the vibration of the sulfonate groups overlaps with those of C-O and Si-O-Si (Wang et al., 2011).

The DSC traces, reported in Figure 3-12, provide information on both the physical state of the materials synthesized as well as the change in the polymer chains mobility induced by the

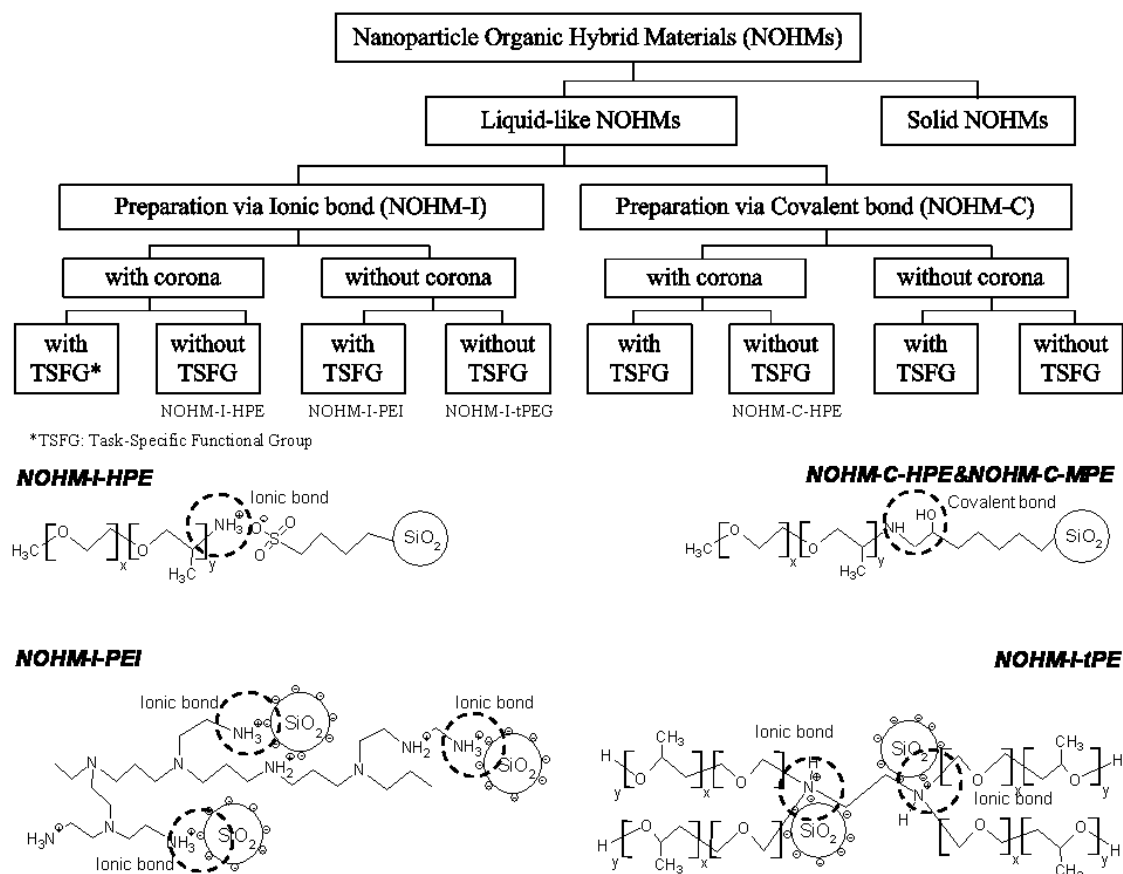
introduction of POSS. As seen from Figure 3-12, the POSS-based NOHMs were liquid at or below room temperature. Compared to the corresponding polymers, no significant difference was noticed. Nevertheless, POSS-I-PS1260 melted at a slightly higher temperature than PS1260. For POSS-I-PC740 and POSS-I-PS1260, the glass transition temperature (T_g) was also similar to that of PC740 and PS1260, respectively. This indicates that the POSS units did not significantly change the chain mobility of the canopy near the glass transition point (Rodriguez et al., 2010). On the contrary, no glass transition was observed for POSS-I-PC460.

POSS-based NOHMs represents a new series of NOHMs which exhibit promising potential for CO₂ capture and even other applications. This dissertation is focused on investigating chemical and structural parameters of NOHMs on CO₂ capture properties. Nanoparticle-based NOHMs appear to be a suitable system to study since various core sizes, core fractions, and polymeric chain lengths could be easily manipulated to prepare NOHMs with a variety of chemical and structural parameters.

Table 3-1 List of POSS-based NOHMs samples with their chemical composition and schematic representation of their overall structure.

Sample*	Polymeric canopy	Inorganic core	Overall schematic structure
POSS-I-PC460	 <p>PC460 $n = 6$ $x = 11-13$</p>	 <p>R = $\text{CH}_2\text{CH}_2\text{NH}_3^+$</p> <p>POSS (N)</p>	 <p>~ = Polymer chain</p>
POSS-I-PC740	 <p>PC740 $n = 11$ $x = 11-13$</p>	 <p>R = $\text{CH}_2\text{CH}_2\text{NH}_3^+$</p> <p>POSS (N)</p>	 <p>~ = Polymer chain</p>
POSS-I-PS1260	 <p>PS1260 $n = 20$</p>	 <p>R = $\text{CH}_2\text{CH}_2\text{NH}_3^+$</p> <p>POSS (N)</p>	 <p>~ = Polymer chain</p>
POSS-C-PEG130	 <p>PEG130 $n = 2$</p>	 <p>R' = O-SiH_3</p> <p>POSS (SiH)</p>	 <p>~ = Polymer chain</p>
POSS-C-PEG250	 <p>PEG250 $n = 4$</p>	 <p>R' = O-SiH_3</p> <p>POSS (SiH)</p>	 <p>~ = Polymer chain</p>

* I: Ionic, PC: Polymer with Carboxylic end group, PS: Polymer with Sulfonic end group, PEG: Polyethylene Glycol.



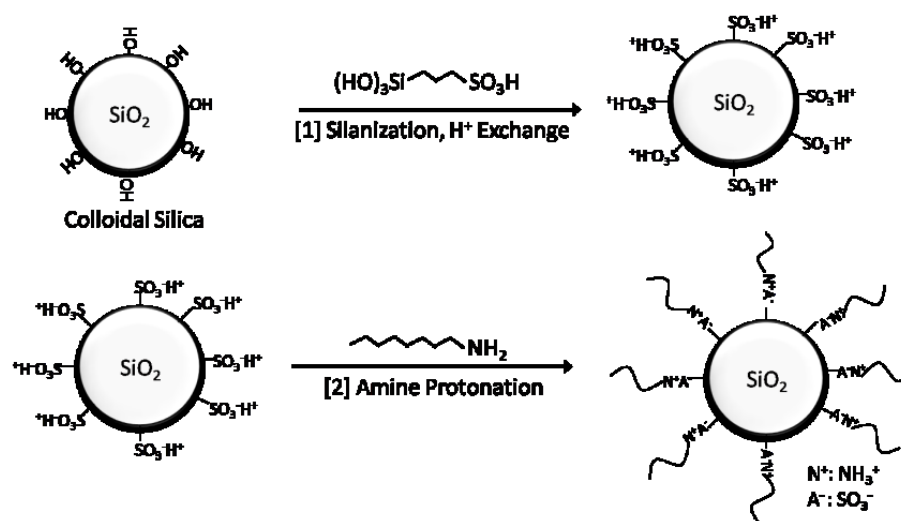


Figure 3-2 Schematic diagram showing NOHMs synthesis.

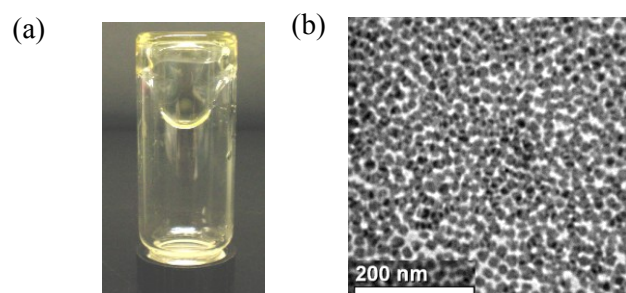


Figure 3-3 Photo (a) and Transmission Electron Microscopy image (b) of a typical NOHMs sample (NOHM-I-tPE).

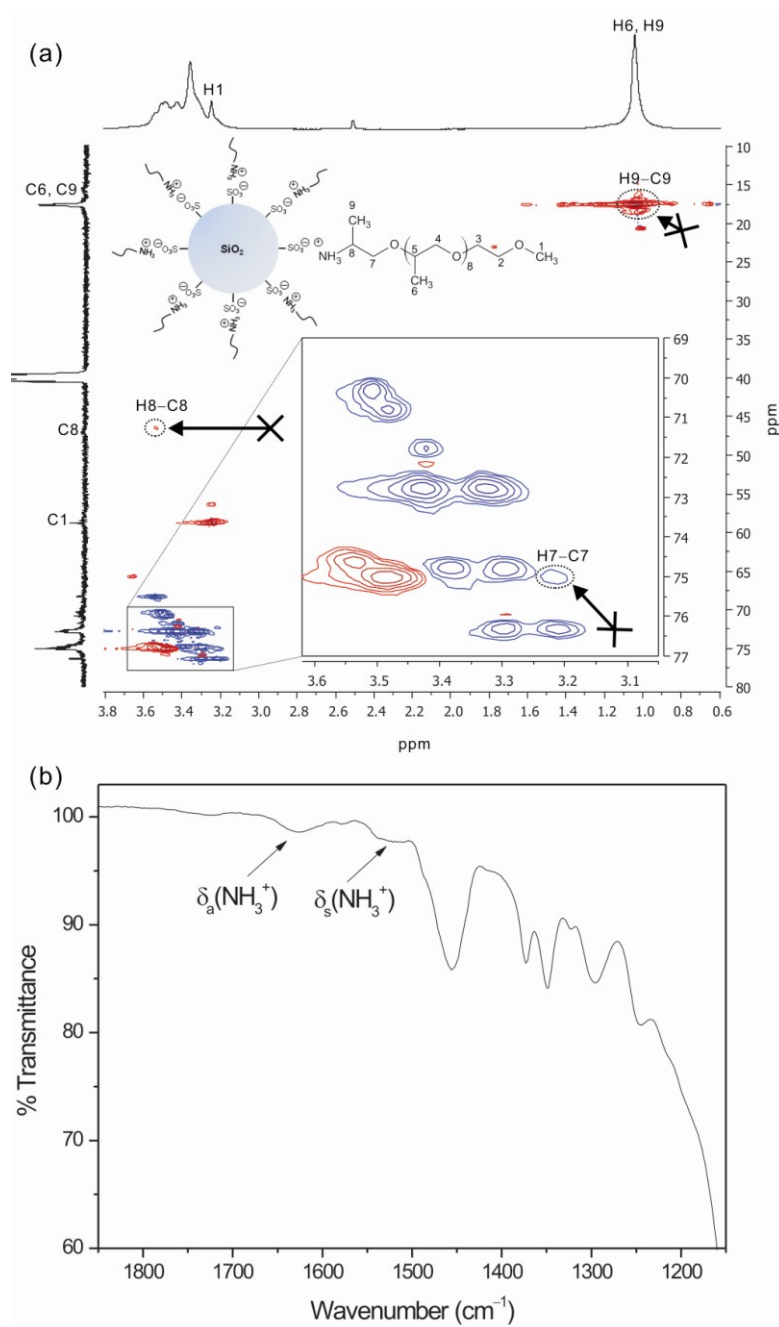


Figure 3-4 (a) 2D ^1H - ^{13}C edited HSQC NMR spectra of NOHM-I-PE600 in $\text{DMSO}-d_6$ at 25 $^\circ\text{C}$. Red contour exhibits carbons of CH or CH_3 (up) whereas blue exhibits CH_2 (down). Peaks in the range $\delta_{\text{H}} = 3.70 - 2.86$ ppm of horizontal ^1H spectra are assigned to CH and CH_2 protons of counterion species. Cross marks indicate the shifted peaks of Polyetheramine M-600. (b) ATR FT-IR spectrum of NOHM-I-PE600 in the range of bending modes of NH_3^+ .

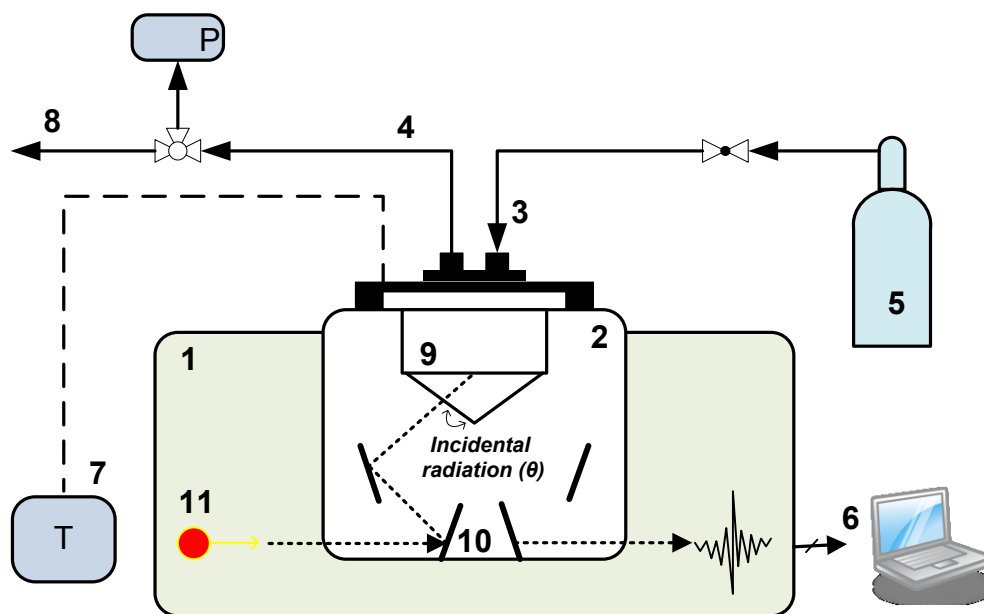


Figure 3-5 Schematic diagram of an in-situ CO₂ capture and diffusivity measurement apparatus. (1) FT-IR spectrometer, (2) ATR optic and high pressure fluid cell, (3) gas line inlet, (4) gas line outlet, (5) CO₂ pressure cylinder, (6) Data acquisition, (7) Temperature controller, (8) Venting line, (9) Diamond crystal, (10) Mirrors, (11) Infrared light source.

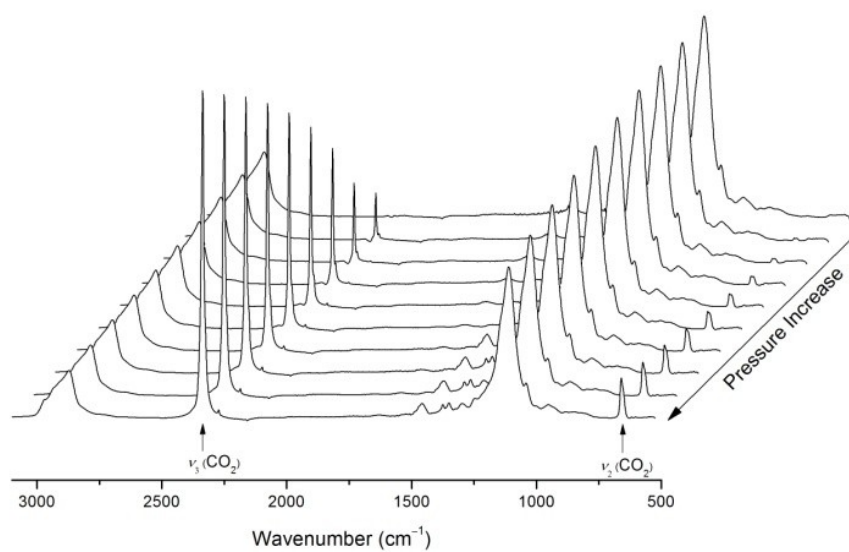


Figure 3-6 ATR FT-IR spectra of NOHM-I-PE2070 with various partial pressures of CO₂ ranging from 0 to 5.5 MPa at 25 °C.

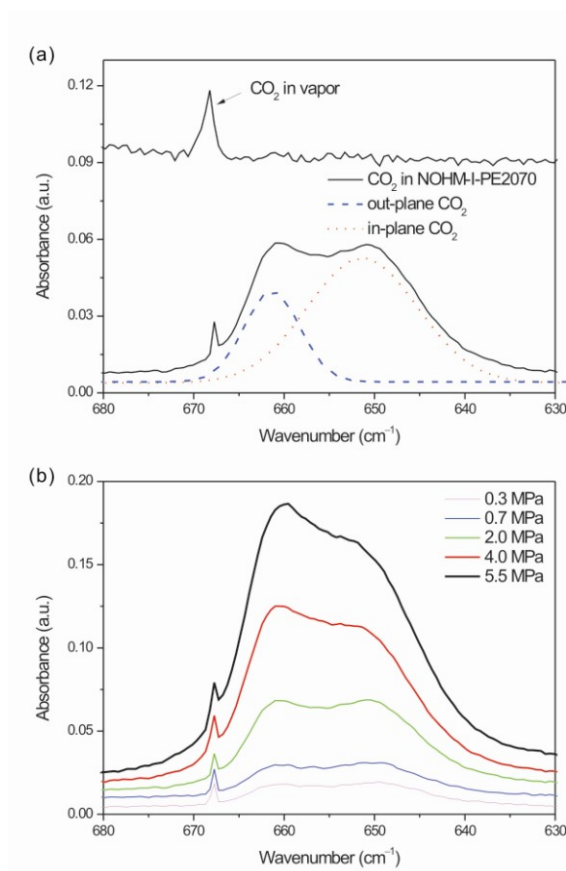


Figure 3-7 ATR FT-IR Spectra of ν_2 bands of NOHM-I-PE2070 pressurized by CO₂ at 25 °C. (a) CO₂ in vapor phase (up) and adsorbed CO₂ in NOHM-I-PE2070 (down). The dotted lines indicate the curve fit spectra. (b) Peak behavior of ν_2 band of CO₂ as a function of pressure.

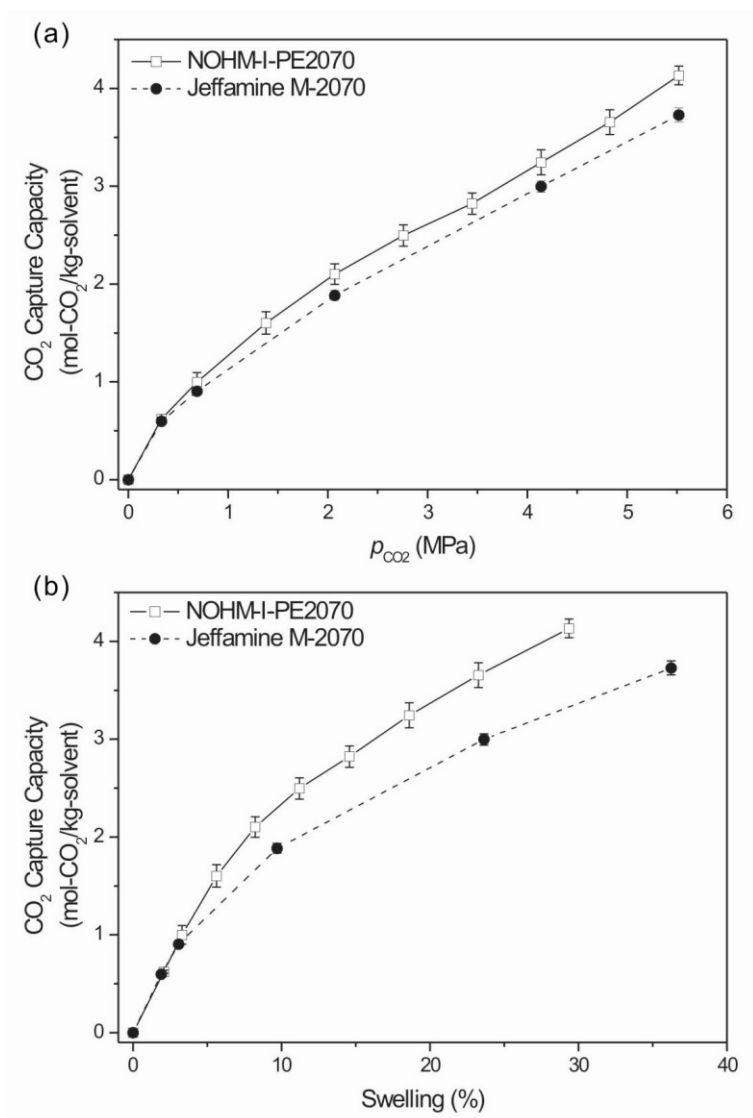


Figure 3-8 CO₂ capture capacity of NOHM-I-PE2070 vs. (a) P_{CO_2} and (b) degree of swelling at 25 °C.

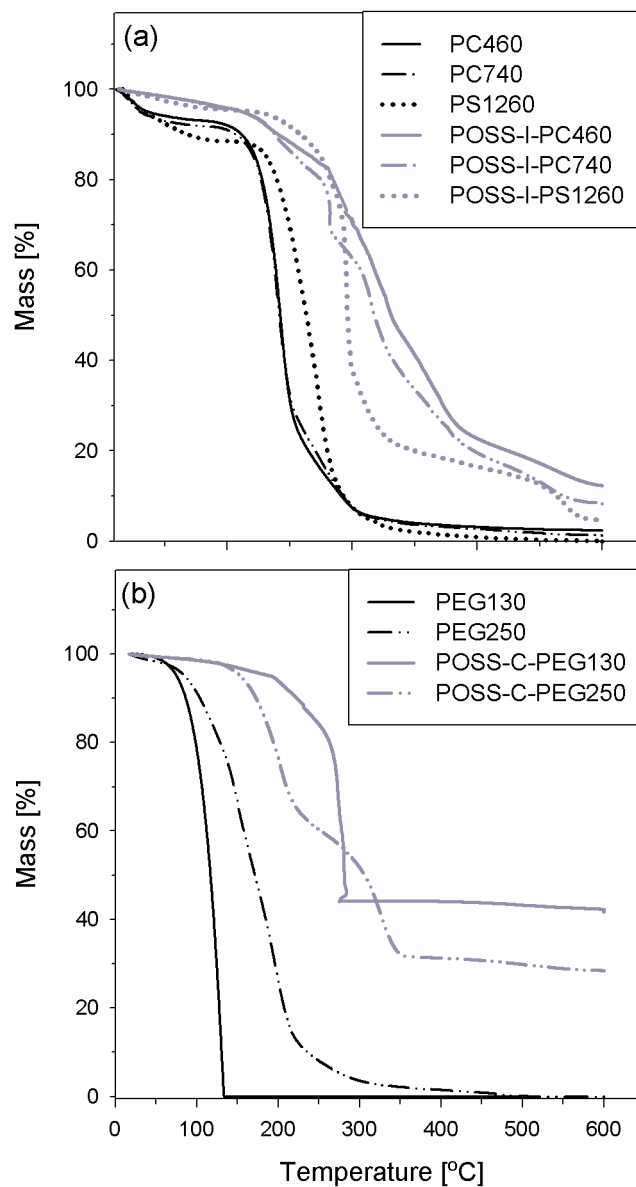


Figure 3-9 Thermogravimetric curves in oxygen atmosphere of: (a) POSS-based NOHMs with ionic bonding and the corresponding unbound polymers, and (b) POSS-based NOHMs with covalent bonding and the corresponding unbound polymers.

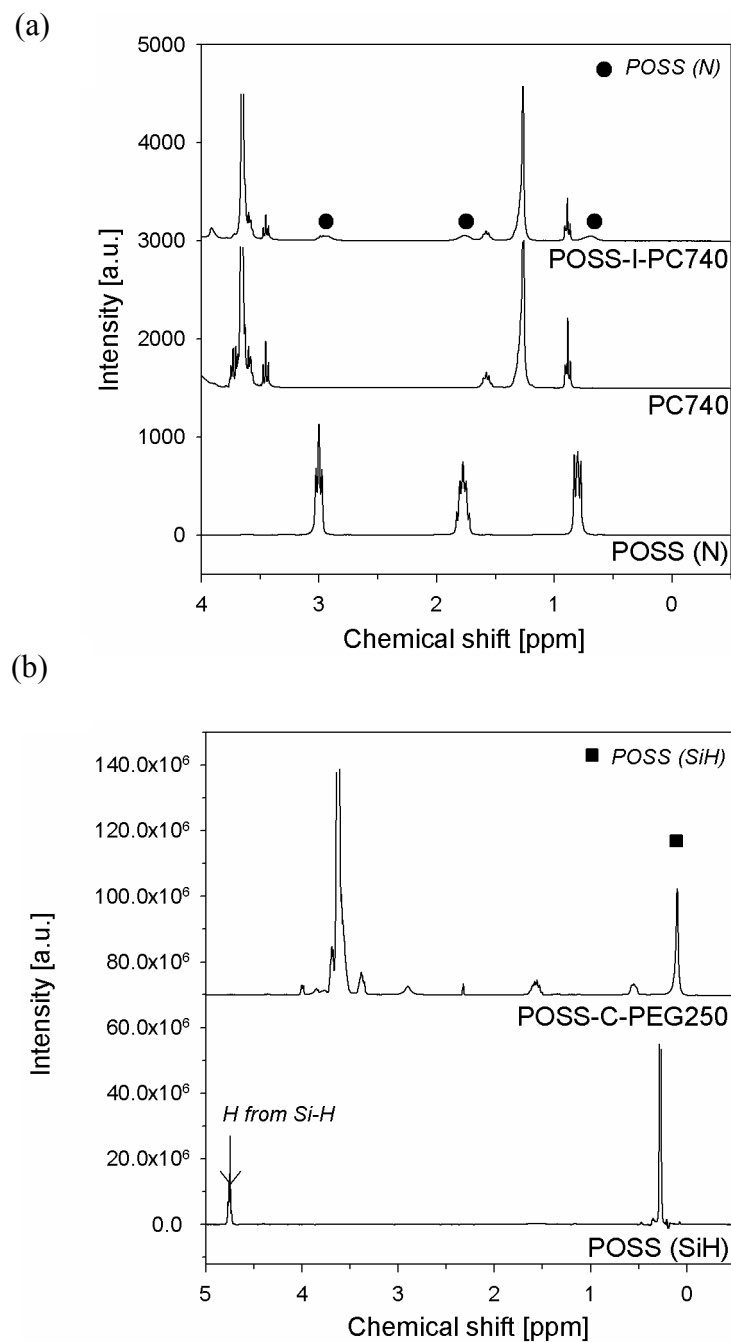


Figure 3-10 Examples of ^1H NMR spectra of the POSS, (a) the polymeric canopy and a POSS-based NOHMs with ionic bonding at 27 °C and (b) a POSS-based NOHMs with covalent bonding at 27 °C. Samples were prepared in CDCl_3 .

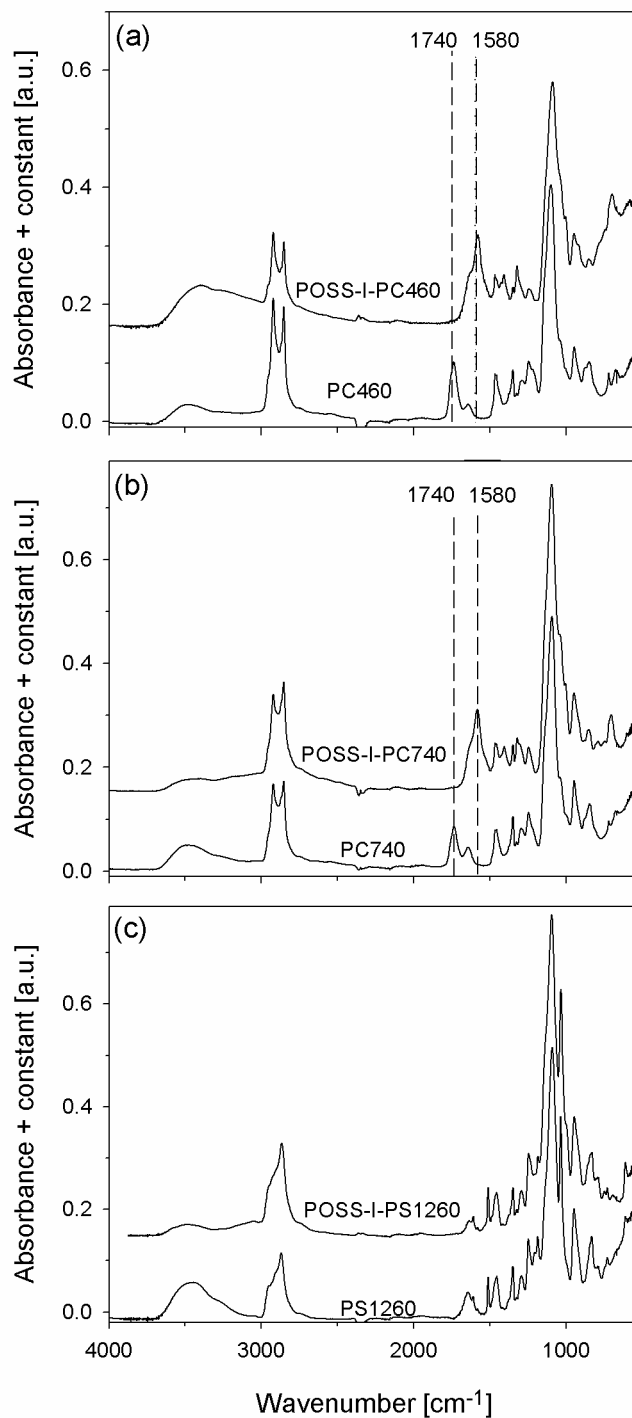


Figure 3-11 ATR FT-IR spectra at 25 °C of: (a) POSS-I-PC460 and its corresponding unbound polymer, (b) POSS-I-PC740 and its corresponding polymer.

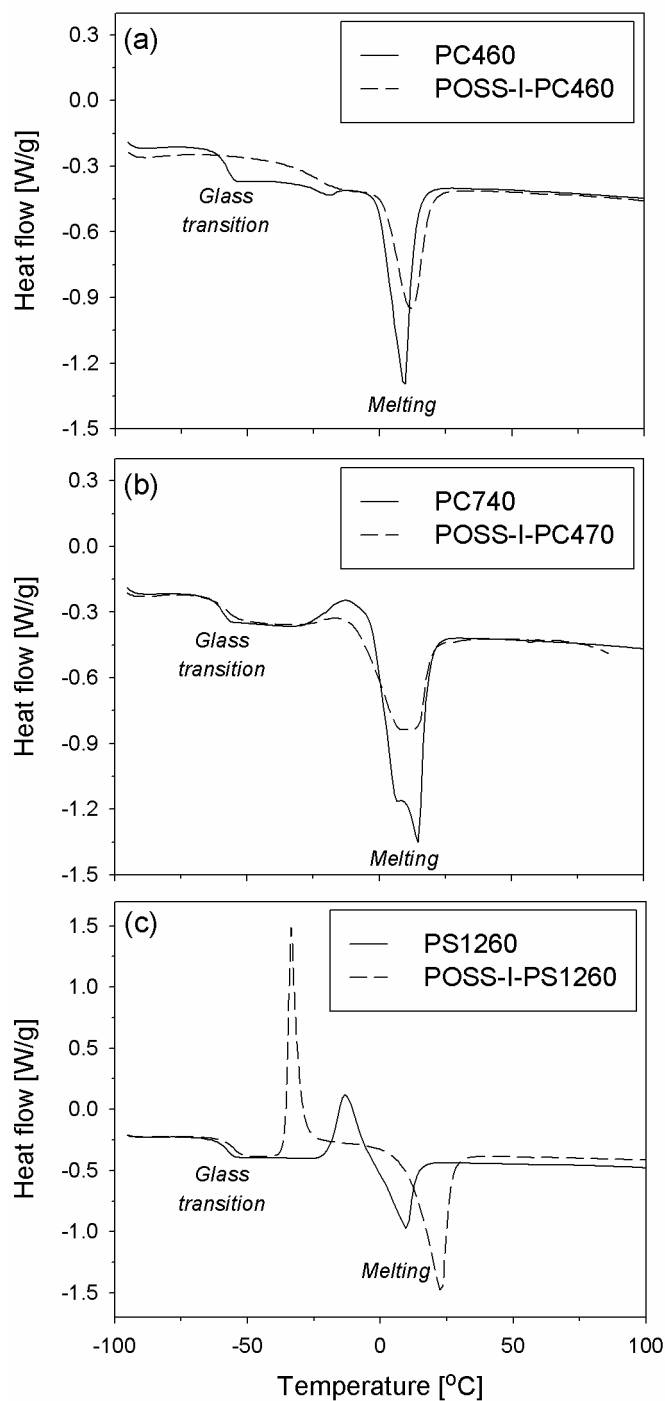


Figure 3-12 DSC traces of: (a) POSS-I-PC460 and its unbound polymer, (b) POSS-I-PC740 and its corresponding unbound polymer, and (c) POSS-I-PS1260 and its corresponding unbound polymer.

Reference

- Aaron, D. and Tsouris, C., "Separation of CO₂ from Flue Gas: A Review", *Separation Science and Technology*, 40, 321-348, 2005.
- Barzagli, F., Mani, F. and Peruzzini, M., "Continuous cycles of CO₂ absorption and amine regeneration with aqueous alkanolamines: a comparison of the efficiency between pure and blended DEA, MDEA and AMP solutions by ¹³C NMR spectroscopy", *Energy & Environmental Science*, 3, 772-779, 2010.
- Belmabkhout, Y. and Sayari, A., "Effect of pore expansion and amine functionalization of mesoporous silica on CO₂ adsorption over a wide range of conditions", *Adsorption*, 15, 318-328, 2009.
- Belmabkhout, Y., Serna-Guerrero, R. and Sayari, A., "Adsorption of from dry gases on MCM-41 silica at ambient temperature and high pressure. 1: Pure adsorption", *Chemical Engineering Science*, 64, 3721-3728, 2009.
- Cabaniss, S. E., Leenheer, J. A. and McVey, I. F., "Aqueous infrared carboxylate absorbances: aliphatic di-acids", *Spectrochimica Acta Part A: Molecular and Biomolecular Spectroscopy*, 54, 449-458, 1998.
- Chang, Y.-W., Wang, E., Shin, G., Han, J.-E. and Mather, P. T., "Poly(vinyl alcohol) (PVA)/sulfonated polyhedral oligosilsesquioxane (sPOSS) hybrid membranes for direct methanol fuel cell applications", *Polymers for Advanced Technologies*, 18, 535-543, 2007.
- Chen, Y. and Iroh, J. O., "Synthesis and Characterization of Polyimide/Silica Hybrid Composites", *Chemistry of Materials*, 11, 1218-1222, 1999.
- Cordes, D. B., Lickiss, P. D. and Rataboul, F., "Recent Developments in the Chemistry of Cubic Polyhedral Oligosilsesquioxanes", *Chemical Reviews*, 110, 2081-2173, 2010.
- Huang, H. Y., Yang, R. T., Chinn, D. and Munson, C. L., "Amine-Grafted MCM-48 and Silica Xerogel as Superior Sorbents for Acidic Gas Removal from Natural Gas", *Industrial & Engineering Chemistry Research*, 42, 2427-2433, 2002.
- Jespersen, M. L., Mirau, P. A., Meerwall, E. v., Vaia, R. A., Rodriguez, R. and Giannelis, E. P., "Canopy Dynamics in Nanoscale Ionic Materials", *ACS Nano*, 4, 3735-3742, 2010.
- Li, G., Wang, L., Ni, H. and Pittman, C. U., "Polyhedral Oligomeric Silsesquioxane (POSS) Polymers and Copolymers: A Review", *Journal of Inorganic and Organometallic Polymers*, 11, 123-154, 2001.
- Li, J.-R., Kuppler, R. J. and Zhou, H.-C., "Selective gas adsorption and separation in metal-organic frameworks", *Chemical Society Reviews*, 38, 1477-1504, 2009.
- Lide, D. R., "CRC handbook of chemistry and physics", *CRC Press, Boca Raton, FL* 1993.
- Lin, K.-Y. A., Park, Y., Petit, C. and Park, A.-H. A., "Investigation of the Structural Parameters affecting the Thermal Stability and the Thermally and CO₂-induced Swelling Behaviors in Liquid-like Nanoparticle Organic Hybrid Materials ", *Environmental Science & Technology*, In preparation 2011.
- Meeks, N. D., S. Rankin, et al., "Sulfur-Functionalization of Porous Silica Particles and Application to Mercury Vapor Sorption" *Industrial & Engineering Chemistry Research* 49(10), 4687-4693, 2010.

- Munoz, D. M., Portugal, A. F., Lozano, A. E., de la Campa, J. G. and de Abajo, J., "New liquid absorbents for the removal of CO₂ from gas mixtures", *Energy & Environmental Science*, 2, 883-891, 2009.
- Qi, G., Wang, Y., Estevez, L., Duan, X., Anako, N., Park, A.-H. A., Li, W., Jones, C. W. and Giannelis, E. P., "High efficiency nanocomposite sorbents for CO₂ capture based on amine-functionalized mesoporous capsules", *Energy & Environmental Science*, 4, 444-452, 2011.
- Rainbolt, J. E., Koech, P. K., Yonker, C. R., Zheng, F., Main, D., Weaver, M. L., Linehan, J. C. and Heldebrant, D. J., "Anhydrous tertiary alkanolamines as hybrid chemical and physical CO₂ capture reagents with pressure-swing regeneration", *Energy & Environmental Science*, 4, 480-484, 2011.
- Rodriguez, R., Herrera, R., Bourlinos, A. B., Li, R., Amassian, A., Archer, L. A. and Giannelis, E. P., "The synthesis and properties of nanoscale ionic materials", *Applied Organometallic Chemistry*, 24, 581-589, 2010.
- Smith, B. C., "Infrared spectral interpretation: a systematic approach", *CRC Press*, 1999.
- Subianto, S., Mistry, M. K., Choudhury, N. R., Dutta, N. K. and Knott, R., "Composite Polymer Electrolyte Containing Ionic Liquid and Functionalized Polyhedral Oligomeric Silsesquioxanes for Anhydrous PEM Applications", *ACS Applied Materials & Interfaces*, 1, 1173-1182, 2009.
- Tanaka, K., Ishiguro, F. and Chujo, Y., "POSS Ionic Liquid", *Journal of the American Chemical Society*, 132, 17649-17651, 2010.
- Wang, Q., Luo, J., Zhong, Z. and Borgna, A., "CO₂ capture by solid adsorbents and their applications: current status and new trends", *Energy & Environmental Science*, 4, 42-55, 2011.

CHAPTER 4

EFFECTS OF CHEMICAL AND STRUCTURAL PARAMETERS ON THERMAL STABILITY OF NOHMs

This chapter is based on the following manuscript in preparation:

K.-Y. A. Lin, Y. Park, C. Petit and A.-H. A. Park, “Investigation of the structural parameters affecting the thermal stability and the thermal and Carbon Dioxide induced swelling behaviors in Liquid-like Nanoparticle Organic Hybrid Materials”, 2012.

4.1 Introduction

Unlike conventional surface-modified nanostructures which are solid in the absence of solvents, (Niemeyer 2001; Pileni 2001; Tohver et al., 2001; Rogach et al., 2002; Scher et al., 2003; Ginger et al., 2004) NOHMs can exhibit liquid-like properties without the addition of solvents. Since the polymer chains are grafted onto the surface-functionalized nanoparticles via chemical bonds, the loss of the polymer in liquid-like NOHMs is prevented, thus allowing zero vapor pressure and enhancing thermal stability (Rodriguez 2008). A higher thermal stability can allow NOHMs to be employed in a wider range of temperatures during CO₂ capture and regeneration. Although NOHMs have exhibited notably higher thermal stability compared to the unbound polymer (Lin and Park 2011), the mechanisms pertaining to this enhanced thermal stability in liquid-like NOHMs, like other polymeric modified nanostructures, are still not thoroughly understood (Pandey et al., 2005; Morgan and Wilkie 2007). Since NOHMs will be used at elevated temperature, the volume change due to the temperature change (so-called thermally-induced swelling) in NOHMs is also important and represents essential information for determining the reactor volume.

Accordingly, this chapter aims at investigating effects of the chemical and structural parameters, such as chain length and presence of core, on the thermal stability and thermally-induced swelling. For synthesizing NOHMs with various chain lengths, linear polymer chains with different molecular weights (MW: 1,000, 2,000, 5,000 g/mol) were chosen. Polyethylene glycol (PEG) was used as the linear polymer chains because it is one of the most common materials for NOHMs (Agarwal et al., 2009; Agarwal and Archer 2011). The thermal stability of NOHMs with various chain lengths was determined by thermogravimetric analysis (TGA).

Thermally-induced swelling was measured by an Attenuated Total Reflectance (ATR) Fourier-transform infrared (FT-IR) Spectrometer.

4.2 Experimental

4.2.1 Synthesis of NOHMs and Ionized PEG

NOHMs were prepared according to the procedure shown schematically in Figure 4-1. Ionized polyethylene glycol (Ionized PEG) was prepared through an acid-base reaction between the mono-amine terminated polyethylene glycol and 3-(trihydroxysilyl)-1-propane sulfonic acid (THOPS, Gelest Inc.). Briefly, the mono-amine terminated polyethylene glycol (PEG) and 3-(trihydroxysilyl)-1-propane sulfonic acid were diluted with deionized water into 10 wt% solutions. While monitoring the pH, the THOPS solution was dropwise added to the PEG solution. Equivalence point plots were employed to ensure the 1:1 ratio of sulfonate groups/amine groups. To obtain the final Ionized PEG, water was removed under reduced pressure at 35 °C.

4.2.2 Thermal Stability Analysis and Thermally-Induced Swelling

Thermal stability experiments were conducted using a TGA (Q50, TA Instrument). The sample was heated with ramping rate 5 °C/min in an oxygen environment. To investigate the long-term stability of NOHMs during a series of temperature swing cycles, cyclic thermal stability experiments were conducted by heating samples cyclically from ambient temperature to a target temperature (e.g. 100 cycles at 120 °C and 25 cycles at 140 °C) in an oxygen environment and then cooling down to the ambient temperature followed by another heating cycle.

The thermally-induced swelling was measured by the ATR FT-IR spectroscopy (as shown in Figure 3-5). The experiment procedure for the thermally-induced swelling of NOHMs and PEGs

began with placing a small amount of the molten sample on the crystal surface which was heated to a desired temperature (60 – 120 °C). All spectra were obtained from the acquisition of 16 scans, the resolution of 4 cm⁻¹, and the spectrum range of 4000 cm⁻¹ – 525 cm⁻¹. Interferograms were multiplied by the Norton–Beer “medium” apodization function prior to Fourier transformation. Stabilization of the thermally-induced swelling at a target temperature was achieved in less than 5 minutes.

The thermally-induced swelling (S) by the ATR FT-IR spectroscopy was calculated by

$$S = \frac{A^0}{A} \cdot \frac{d_e}{d_e^0} - 1 \quad (4-1)$$

where A_0 , d_e^0 , A , and d_e are the absorbance and the effective path length at T_0 ($T_0 = 60$ °C) and T ($T = 70$ °C to 120 °C), respectively. It was assumed that the effective path length is not significantly affected by the temperature change. In order to measure the degree of the thermally-induced swelling, the absorbance of C–H stretching bands around 2840 cm⁻¹ was selected, which is one of the characteristic bands for the polymer chains of NOHMs and the corresponding PEGs. The absorbance at the temperatures studied was integrated in the interval from 2600 cm⁻¹ to 3000 cm⁻¹.

4.3 Results and Discussion

4.3.1 Characterization of NOHMs and Ionized PEG

In general, the synthesized NOHMs were denoted as NOHM-I-PEG (MW)-wt% of nanoparticles. However, those synthesized at the equivalence point are referred to as NOHM-I-PEG (MW) E, where “E” indicates the equivalence point and “I” refers to the formation of

NOHMs via ionic bonding. Ionized PEG was prepared to isolate the effect of the acid-base reaction formed between PEG and THOPS without nanoparticles. PEG1K / NP-25 corresponds to a physical mixture of PEG1K with dry colloidal silica (no addition of THOPS). All materials investigated in this study are assigned sample IDs and listed in Table 4-1.

Since NOHMs and Ionized PEG were synthesized via the acid-base reaction, ATR FT-IR spectroscopy was used to determine the reaction between the primary amine of PEG and the sulfonate groups on the surface-modified nanoparticles. The ATR FT-IR spectra of PEG1K, Ionized PEG1K and NOHM-I-PEG1K were displayed in Figure 4-2. Unlike on the spectrum of PEG1K, the protonated amine $\delta_s(\text{NH}_3^+$, symmetric bending mode) at 1530 cm^{-1} and $\delta_a(\text{NH}_3^+$, asymmetric bending mode) at 1630 cm^{-1} appeared on the spectrum of Ionized PEG1K, which confirmed the acid-base reaction between the primary amine and the sulfonate group. In NOHM-I-PEG1K, the protonated amine bands were also observed, indicating the formation of ionic bonding between the primary amine and the sulfonate group, suggesting that PEG1K successfully grafted onto the modified nanoparticles. The protonated amine bands were also seen in NOHM-I-PEG2K, NOHM-I-PEG5K, Ionized 2K and Ionized 5K.

4.3.2 Effects of Chemical and Structural Parameters on Thermal Stability

PEGs were first tested for their thermal stabilities to provide a baseline for comparing with NOHMs and Ionized PEGs. Figure 4-3 shows the thermal stability of PEG1K, PEG2K and PEG5K measured by TGA, which displays a sample's mass change as a function of temperature. The initial temperatures of degradation (T_d^i) of the three PEGs all appeared at $175\text{ }^\circ\text{C}$ and the effect of polymer chain length was not significant in terms of the decomposition temperature (as measured at the point of 50% mass loss) (Gilman 1999).

Prior to examining the thermal stability of NOHMs, Ionized PEGs which contain ionic bonding and the alkoxysilane (THOPS) as in NOHMs were analyzed by TGA. Figure 4-3 shows the thermogravimetric (TG) curves of Ionized PEGs. All Ionized PEGs exhibited higher decomposition temperatures (as measured at the point of 50% mass loss caused by thermal decomposition) than their pristine corresponding PEGs: 98 °C higher in Ionized PEG1K, 63 °C higher in Ionized PEG2K and 25 °C higher in Ionized PEG5K.

Such an enhancement of thermal stability in Ionized PEGs was caused by ionic bonding which causes that additional heat is required to degrade the polymer (Pielichowski et al., 2010). Since the enhancement was most pronounced in Ionized PEG1K, followed by Ionized PEG2K and then Ionized PEG5K, this suggests that the contribution of a single ionic bond to thermal stability was more pronounced as the polymer chain length was shortened. Accordingly, as the chain length increases, the contribution from the single ionic bond on thermal stability to the whole Ionized PEG is diminished.

4.3.3 Effect of the Surface-Modified Nanoparticles

By grafting PEG onto the surface-modified nanoparticles, PEG was protonated and participated in the acid-base reaction to create ionic bonding. Unlike Ionized PEG, THOPS, the alkoxysilane, in NOHMs were tethered to the nanoparticles (cores). Thermal stabilities of NOHMs with various chain lengths were measured and shown in Figure 4-4. Compared to the pristine PEGs, all NOHMs showed considerably higher decomposition temperatures (as measured at the point of 50% mass loss): 123 °C higher in NOHM-I-PEG1K, 100 °C higher in NOHM-I-PEG2K, and 85 °C higher in NOHM-I-PEG5K. This indicates that grafting the polymer chains onto the surface-modified nanoparticles also significantly enhanced the thermal stability of PEG. The

enhancement was most pronounced in NOHM-I-PEG1K-E, and was less for NOHM-I-PEG with longer polymer chains. Figure 4-4 also reveals an interesting feature that during the mass change from 100% to 60%, NOHM-I-PEG5K-E exhibited a linear decomposition curve while NOHM-I-PEG1K-E and NOHM-I-PEG2K-E exhibited non-linear decomposition curves. This indicates that the initial degradation of NOHM-I-PEG5K-E was not retarded while the initial degradation of NOHM-I-PEG1K-E and NOHM-I-PEG2K-E was retarded. This difference may be attributed to the fact that NOHM-I-PEG5K-E has a relatively long chain and its free end is far from the location of the core. Since the degradation of a polymeric chain is initiated from weak sites, such as an unstable end or side chain groups (Pielichowski et al., 2010), NOHM-I-PEG5K-E was decomposed readily starting from its “weak” site (i.e., the end of the polymer chain). Correspondingly, since the polymer chains in NOHM-I-PEG1K-E and NOHM-I-PEG2K-E were shorter and strengthened by the graft onto the surface-modified nanoparticles, the initial degradation was retarded significantly. Thus, the location of additional bonding and core also affected the extent of the enhancement in thermal stability of NOHMs.

As discussed previously, the acid-base reaction between the primary amine of PEG and the sulfonate group of the surface-modified nanoparticles contributed to part of the thermal stability enhancement by the additional bonding. However, the effect of the introduction of nanoparticles on the enhancement has yet to be determined. Some reports in the literature have indicated that the addition of nanofillers into a polymer medium can enhance thermal stability (Giannelis 1996; Gilman 1999; Gilman et al., 2000; Zhu et al., 2001; Utracki 2004; Zanetti et al., 2004; Pavlidou and Papaspyrides 2008) due to physical cross-linking or contact between the polymer and the nanofillers (Pielichowski et al., 2010).

Since NOHM-I-PEG1K, NOHM-I-PEG2K and NOHM-I-PEG5K were prepared with the 1:1 ratio of sulfonate groups/amine groups, the same amount of sulfonate groups was used to protonate PEGs of various MW. Therefore, the wt% of nanoparticles in three NOHMs were different: 25 wt% for NOHM-I-PEG1K-E, 19 wt% for NOHM-I-PEG2K-E, and 5 wt% for NOHM-I-PEG5K-E. The interface contact in each NOHMs could be varied as the weight fraction of nanoparticles changed. Thus, it is essential to clarify whether the different degrees of enhancement in NOHMs' thermal stability were caused by varied extents of interface contact in NOHMs. Thus, NOHM-I-PEG2K-25 and NOHM-I-PEG5K-25, both with a 25 wt% of nanoparticles, were prepared. Since sulfonate groups exhibit distinct thermal stability, the same sulfonate group functionalized nanoparticle was employed to NOHM-I-PEG2K-25 and NOHM-I-PEG5K-25 below the equivalent point to have same interface contact as NOHM-I-PEG1K-E whose core fraction is 25 wt%. Thus, the degree of interface contact and the amount of sulfonate groups in NOHM-I-PEG1K-E, NOHM-I-PEG2K-25 and NOHM-I-PEG5K-25, were controlled to be equal. As seen in Figure 4-5 NOHM-I-PEG1K-E still exhibited the highest thermal stability among the three NOHMs, followed by NOHM-I-PEG2K-25 and then NOHM-I-PEG5K-25. This indicates that the interface contact from the nanoparticle surface was not a dominant factor in enhancing the thermal stability of NOHMs. There must be other factors predominantly affecting the thermal stability.

In order to determine these factors, a mixture of PEG1K with dry silica nanoparticles (ave. dia. =12 nm, same size as used for NOHM-I-PEG preparation) was prepared (denoted as PEG1K / NP-25) and tested for its thermal stability. The difference between NOHM-I-PEG1K and PEG1K / NP-25 was that THOPS was used in NOHM-I-PEG1K as the alkoxysilane while no THOPS was used in PEG1K / NP-25. THOPS initiated silanization during the synthesis of

NOHMs and covalently bonded the surface of the nanoparticle, which resulted in the formation of a silica network (Si–O–Si bond).

Figure 4-6 shows the thermal stabilities of PEG1K, PEG1K / NP-25, Ionized PEG1K, and NOHM-I-PEG1K. Without the existence of ionic bonding and the silica network, PEG1K / NP-25 exhibited no enhancement in thermal stability compared to PEG1K in terms of T_d^i , even though the physical contact existed. The introduction of colloidal silica did not show any positive contribution to the thermal stability. A similar observation was also found for the mixture of colloidal silica with polymaleimides (Lu and Huang 2002). This may be due to the high fraction of polymer in NOHMs, which is required to ensure NOHMs' fluid feature, leading to the significantly limited physical interface contact existing between the polymer and the nanoparticles in NOHMs compared to conventional solid nanocomposites in which usually the polymer fraction is relatively low. Nanoparticles may not be uniformly dispersed in the physically mixed blend; and the uneven dispersion may have limited interaction between polymer chains and nanoparticles leading to no visible impact on thermal stability. Nevertheless, the fact that there was not even partial thermal stability enhancement in the physical mixture of polymer and nanoparticles, suggests that physical blending does not improve the thermal stability of the system. Consequently, the enhancement in thermal stability caused by physical interaction was not significant.

However, once ionic bonding was incorporated in PEG (e.g. Ionized PEG1K), the thermal stability was significantly enhanced as mentioned earlier. Following the presence of ionic bonding, the silica network took place on the surface of the nanoparticles by the silanization which also enhanced the thermal stability significantly. Therefore, the factors leading to the enhancement of thermal stability were mainly the presence of ionic bonding and the occurrence

of the silica network to provide “additional bonding” within NOHMs. This additional bonding means that more thermal energy is required to degrade NOHMs.

4.3.4 Long-Term Thermal Stability

Owing to the enhanced thermal stability, NOHMs can be operated in a wider range of temperatures and allow their recycling/regeneration via a temperature swing process without significant loss of the material. As mentioned earlier, NOHMs have been proposed for CO₂ capture and generally NOHMs can be regenerated via a pressure swing or a temperature swing process to release CO₂. When the temperature swing process is employed, the CO₂-rich NOHMs are heated up to a certain temperature to release CO₂. Most of CO₂ capture media are regenerated at 120 °C (Goff and Rochelle 2004) or higher to release CO₂. Herein, NOHM-I-PEG1K was tested for its thermal stability during a series of temperature swing cycles and the results were compared to those of PEG1K. Figure 4-7 shows the residual mass of NOHM-I-PEG1K and PEG1K after a 100-cycle temperature swing (20 °C – 120 °C) process. While the residual mass of PEG1K was less than 20% after the 100 cycles, there was no significant loss in the case of NOHM-I-PEG1K. The enhanced thermal stability of NOHM-I-PEG1K, when compared to PEG1K (T_d^i increased by about 70 °C), considerably avoided the loss of the material during the temperature swing process. At a higher temperature (140 °C), the advantage of the enhancement on the recyclability of NOHMs over PEG1K was observed even more readily. Thus, the enhanced thermal stability of NOHMs significantly increases their long-term thermal recyclability.


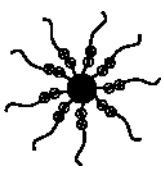



4.3.5 Thermally-Induced Swelling of NOHMs

Since NOHMs are proposed to operate at elevated temperatures for CO₂ capture and regeneration, the elevated temperature can cause volume changes within NOHMs. This thermally-induced volume change (swelling) represents critical information for the reactor design. Figure 4-8 presents the thermally-induced swelling of NOHMs and the corresponding PEGs with various chain lengths in the temperature range from 60 to 120 °C. As described in equation (4-1), the swelling percentage was calculated based on the absorbance of NOHMs at 60 °C over the absorbance of NOHMs at a higher temperature (70 °C – 120 °C). As seen in Figure 4-8, the effect of higher temperatures significantly caused swelling in both NOHMs and PEGs. In the case of PEGs, although their molecular weight ranged from 1000 to 5000 g/mol, the effect of polymer length was negligible and the three PEGs all exhibited around 2 % swelling per 10 °C increase. Compared to the latter value, the thermally-induced swelling of chains of NOHMs with various chain lengths was smaller. Such a difference may be attributed to the restriction on the movement of the polymer chains tethered onto the nanoparticle surface. Additionally, the effect of chain length on the thermally-induced swelling was notable in the case of NOHMs. For a given increase in temperature, NOHM-I-PEG5K exhibited more swelling, followed by NOHM-I-PEG2K and then NOHM-I-PEG1K, suggesting decreased thermally-induced swelling for NOHMs with shorter chain lengths. Less thermally-induced swelling in NOHMs can reduce the reactor volume when NOHMs is employed at elevated temperatures for CO₂ capture or regeneration.

4.4 Conclusions

Compared to unbound PEGs, NOHMs exhibited enhanced thermal stability. Although the introduction of nanoparticles in NOHMs provided physical interface contact between the polymer and the nanoparticles, this enhancement was predominantly attributed to ionic bonding existing in NOHMs and the silica network formed on the nanoparticle surface. Due to these additional bondings, NOHM-I-PEG1K, exhibited a significant increase on the initial degradation temperature (70 °C) compared to its corresponding polymer. Such an increase allows NOHMs to be used in a wider range of operational temperatures. NOHM-I-PEG1K was also tested in a series of cyclic temperature swing to investigate its thermal recyclability. While PEG1K degraded 80 wt% after a 100-cycle temperature swing, there was no significant loss in NOHM-I-PEG1K. Experiments of thermally-induced swelling of NOHMs indicate reduced swelling compared to that of PEGs. The effect of chain length on thermal stability and swelling behaviors can provide valuable information to optimize NOHMs for CO₂ capture.

Table 4- 1 List of NOHMs and polymers

Category	Sample ID	Description	Core Fraction (wt%)
PEG Amine group 	PEG1K	Mono-amine terminated PEG of MW 1000	-
	PEG2K	Mono-amine terminated PEG of MW 2000	-
	PEG5K	Mono-amine terminated PEG of MW 5000	-
NOHMs 	NOHM-I-PEG1K-E	Chain = PEG ^[a] of MW 1000 at Equivalent point ^[b]	25
	NOHM-I-PEG2K-E	Chain = PEG of MW 2000 at Equivalent point	19
	NOHM-I-PEG5K-E	Chain = PEG of MW 5000 at Equivalent point	5
	NOHM-I-PEG2K-25	Chain = PEG of MW 2000 at 25 wt% core fraction	25
	NOHM-I-PEG5K-25	Chain = PEG of MW 5000 at 25 wt% core fraction	25
Mixture of PEG and nanoparticles 	PEG1K / NP-25	Physical mixture of “PEG1K” and 25 wt % of silica nanoparticles	25
Ionized PEG 	Ionized PEG1K	Ionized “PEG1K” using THOPS ^[c]	-
	Ionized PEG2K	Ionized “PEG2K” using THOPS	-
	Ionized PEG5K	Ionized “PEG5K” using THOPS	-
mPEG Methoxy group 	mPEG1K	Methoxy-PEG of MW 1000	-
	mPEG2K	Methoxy-PEG of MW 2000	-
	mPEG5K	Methoxy-PEG of MW 5000	-

[a] PEG: PolyEthylene Glycol

[b] Anionic polymer chains : cationic sites on nanoparticles = 1 : 1

[c] THOPS: 3-(trihydroxysilyl)-1-propane sulfonic acid

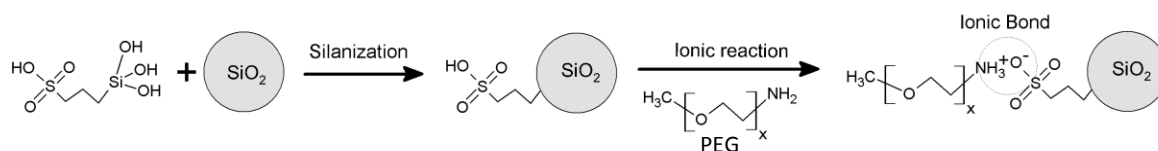


Figure 4-1 Scheme of the synthesis of PEG-based NOHMs

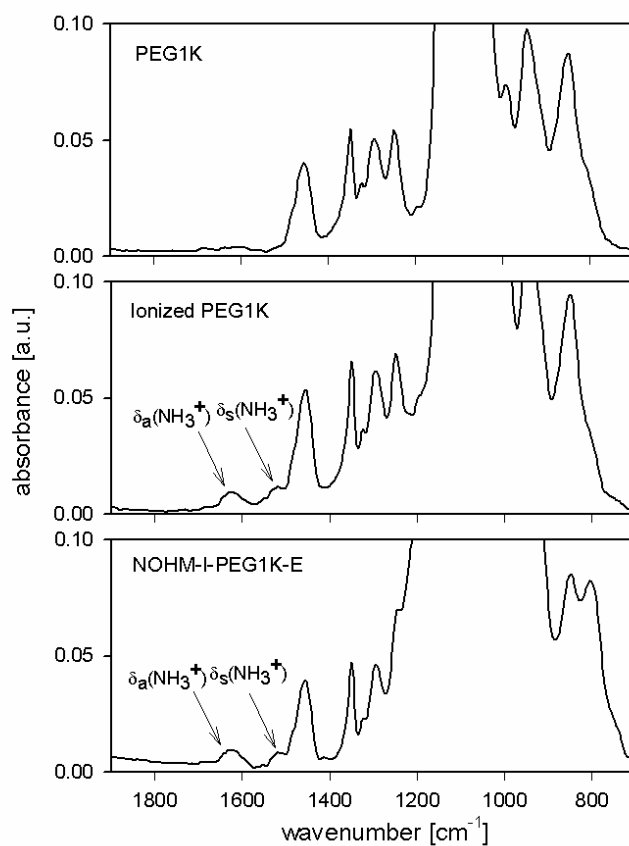


Figure 4-2 ATR FT-IR spectra of PEG1K, Ionized PEG1K and NOHM-I-PEG1K-E.

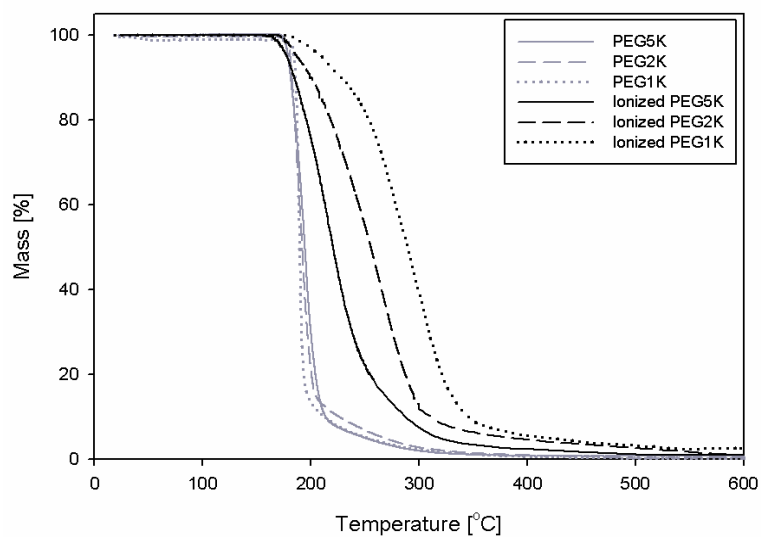


Figure 4-3 Thermal stability of Ionized PEGs with various molecular weights and the corresponding PEGs in oxygen environment with a ramping rate 5 °C/min.

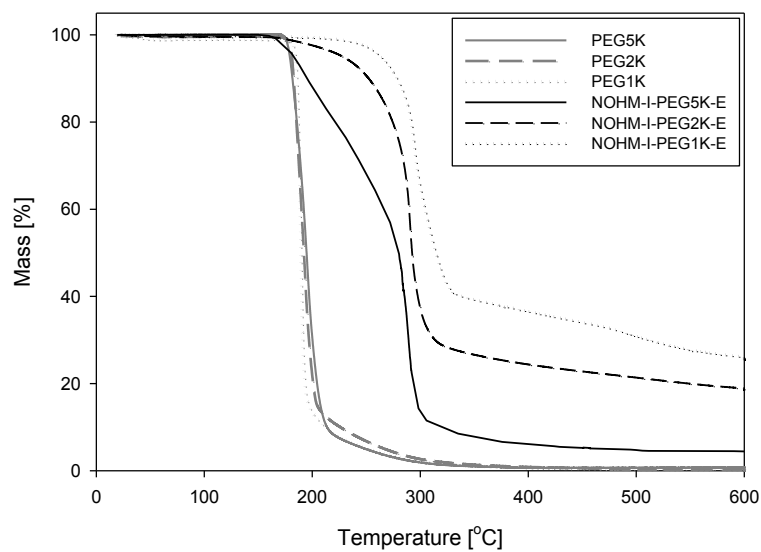


Figure 4-4 Thermal stability of NOHMs with various chain lengths and the corresponding PEGs in oxygen environment with a ramping rate 5 °C/min.

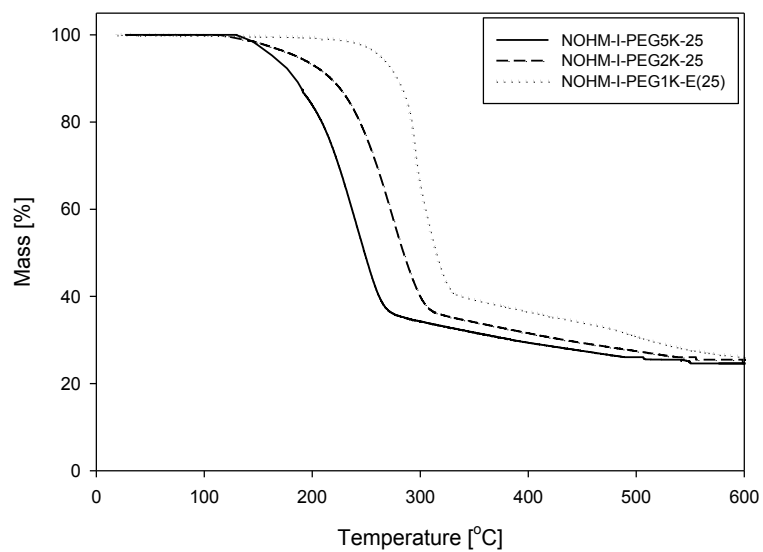


Figure 4-5 Thermal stabilities of NOHMs with the same core fraction and various chain lengths in oxygen environment with a ramping rate 5 °C/min.

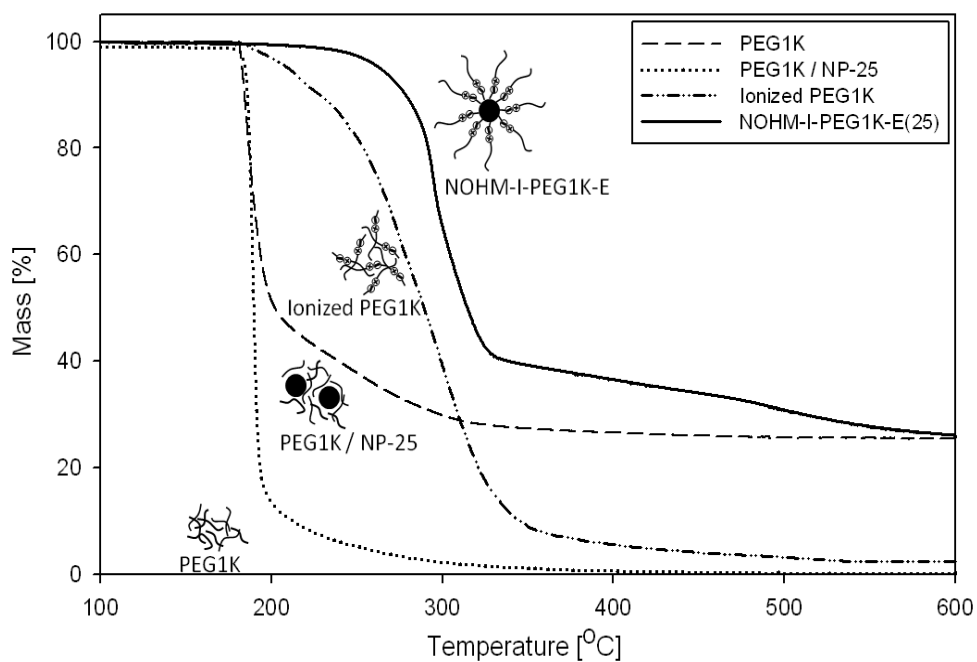


Figure 4-6 Thermal stability of, PEG1K, PEG1K / NP-25, Ionized PEG1K and NOHM-I-PEG1K-E in oxygen environment with a ramping rate 5 °C/min.

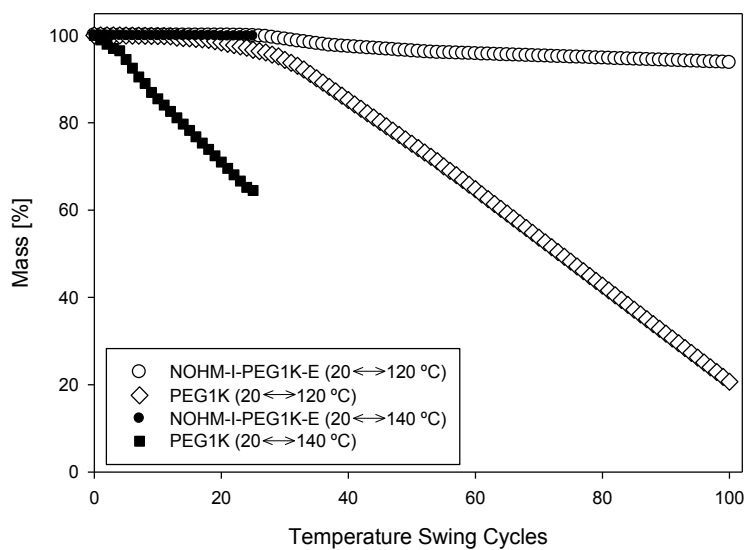


Figure 4-7 Cyclic thermal stability of NOHM-I-PEG1K-E and PEG1K (temperature swing from 20 °C to 120 °C/140 °C with a ramping rate 5 °C/min and isothermal for 5 minutes, each cycle is 25/29 minutes, respectively)

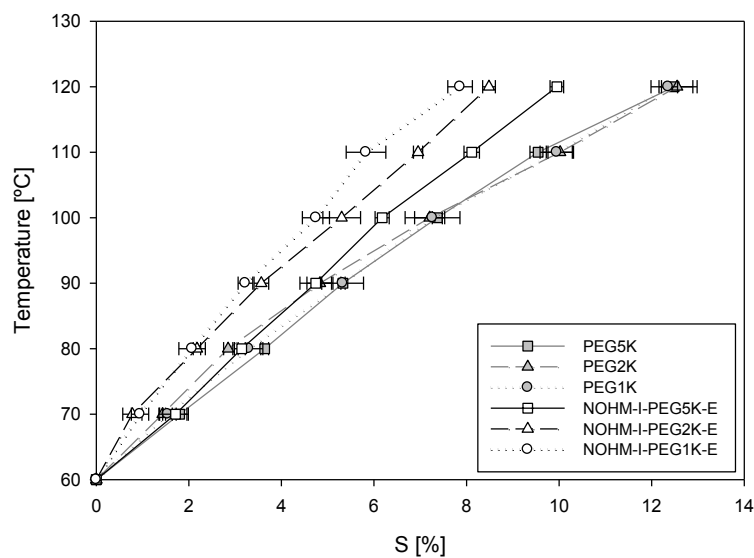


Figure 4-8 Thermally-induced swelling of NOHMs with various chain lengths (conducted at $P_{CO_2} = 0$ MPa).

Reference

- Agarwal, P. and Archer, L. A., "Strain-accelerated dynamics of soft colloidal glasses", *Physical Review E*, 83, 041402, 2011.
- Agarwal, P., Qi, H. and Archer, L. A., "The Ages in a Self-Suspended Nanoparticle Liquid", *Nano Letters*, 10, 111-115, 2009.
- Giannelis, E. P., "Polymer Layered Silicate Nanocomposites", *Advanced Materials*, 8, 29-35, 1996.
- Gilman, J. W., "Flammability and thermal stability studies of polymer layered-silicate (clay) nanocomposites", *Applied Clay Science*, 15, 31-49, 1999.
- Gilman, J. W., Jackson, C. L., Morgan, A. B., Harris, R., Manias, E., Giannelis, E. P., Wuthenow, M., Hilton, D. and Phillips, S. H., "Flammability Properties of Polymer-Layered-Silicate Nanocomposites. Polypropylene and Polystyrene Nanocomposites", *Chemistry of Materials*, 12, 1866-1873, 2000.
- Ginger, D. S., Zhang, H. and Mirkin, C. A., "The Evolution of Dip-Pen Nanolithography", *Angewandte Chemie International Edition*, 43, 30-45, 2004.
- Goff, G. S. and Rochelle, G. T., "Monoethanolamine Degradation: O₂ Mass Transfer Effects under CO₂ Capture Conditions", *Industrial & Engineering Chemistry Research*, 43, 6400-6408, 2004.
- Lin, K.-Y. A. and Park, A.-H. A., "Effects of Bonding Types and Functional Groups on CO₂ Capture using Novel Multiphase Systems of Liquid-like Nanoparticle Organic Hybrid Materials", *Environmental Science & Technology*, 2011.
- Lu, G. T. and Huang, Y., "Synthesis of polymaleimide/silica nanocomposites", *Journal of Materials Science*, 37, 2305-2309, 2002.
- Morgan, A. B. and Wilkie, C. A., *Flame Retardant Polymer Nanocomposites*, John Wiley & Sons, Inc., New York, 2007.
- Niemeyer, C. M., "Nanoparticles, Proteins, and Nucleic Acids: Biotechnology Meets Materials Science", *Angewandte Chemie International Edition*, 40, 4128-4158, 2001.
- Pandey, J. K., Raghunatha Reddy, K., Pratheep Kumar, A. and Singh, R. P., "An overview on the degradability of polymer nanocomposites", *Polymer Degradation and Stability*, 88, 234-250, 2005.
- Pavlidou, S. and Papaspyrides, C. D., "A review on polymer-layered silicate nanocomposites", *Progress in Polymer Science*, 33, 1119-1198, 2008.
- Pielichowski, K., Leszczyńska, A. and Njuguna, J., "Mechanisms of Thermal Stability Enhancement in Polymer Nanocomposites", *Optimization of Polymer Nanocomposite Properties*, 195-210, 2010.
- Pileni, M. P., "Nanocrystal Self-Assemblies: Fabrication and Collective Properties", *The Journal of Physical Chemistry B*, 105, 3358-3371, 2001.
- Rodriguez, R., Herrera, R., Archer, L. A., Giannelis, E. P., "Nanoscale Ionic Materials", *Adv. Mater.*, 20, 4353-4358, 2008.
- Rogach, A. L., Talapin, D. V., Shevchenko, E. V., Kornowski, A., Haase, M. and Weller, H., "Organization of Matter on Different Size Scales: Monodisperse Nanocrystals and Their Superstructures", *Advanced Functional Materials*, 12, 653-664, 2002.
- Scher, E. C., Manna, L. and Alivisatos, A. P., "Shape control and applications of nanocrystals", *Philosophical Transactions of the Royal Society of London. Series A: Mathematical, Physical and Engineering Sciences*, 361, 241-257, 2003.

- Tohver, V., Chan, A., Sakurada, O. and Lewis, J. A., "Nanoparticle Engineering of Complex Fluid Behavior", *Langmuir*, 17, 8414-8421, 2001.
- Utracki, L. A., *Clay-Containing Polymeric Nanocomposites*, Rapra, Shawbury, 2004.
- Zanetti, M., Bracco, P. and Costa, L., "Thermal degradation behaviour of PE/clay nanocomposites", *Polymer Degradation and Stability*, 85, 657-665, 2004.
- Zhu, J., Morgan, A. B., Lamelas, F. J. and Wilkie, C. A., "Fire Properties of Polystyrene–Clay Nanocomposites", *Chemistry of Materials*, 13, 3774-3780, 2001.

CHAPTER 5

EFFECTS OF STRUCTURAL PARAMETERS ON CO₂ CAPTURE CAPACITY, CO₂-INDUCED AND PACKING BEHAVIORS OF NOHMs

This chapter is based on the following publication:

C. Petit, Y. Park, **K.-Y. A. Lin** and A.-H. A. Park, “Spectroscopic investigation of the canopy configurations in Nanoparticle Organic Hybrid Materials of various grafting densities”, *Journal of Physical Chemistry C*, 2011, DOI: 10.1021/jp210391c

The manuscript in preparation:

K.-Y. A. Lin, Y. Park, C. Petit and A.-H. A. Park, “Investigation of the structural parameters affecting the thermal stability and the thermal and Carbon Dioxide induced swelling behaviors in Liquid-like Nanoparticle Organic Hybrid Materials”, 2011.

5.1 Introduction

As mentioned in Chapter 4, elevated temperatures can cause NOHMs to swell. It is essential to investigate swelling behavior since volume change in NOHMs determines the size of reactors. The swelling behavior also provides understanding of the interactions between polymer chains in NOHMs. Besides temperature, CO₂ sorption can also cause significant swelling of NOHMs which is also known as CO₂-induced swelling. Investigation of structural parameters on CO₂-induced swelling not only provides information to design reactors, but also gives critical information on intermolecular relationships between CO₂ and polymer chains of NOHMs as well as the entropic effect of NOHMs configuration. Since CO₂-induced swelling behavior is associated with how CO₂ is packed within NOHMs' polymer chains, CO₂ packing behavior is also investigated.

This chapter aims to investigate the effects of the structural parameters, such as chain length and grafting density on CO₂-induced swelling and packing behaviors in NOHMs. For synthesizing NOHMs with various chain lengths, linear polymer chains with different molecular weights were chosen. Polyethylene glycol (PEG) was used as liner polymer chains because PEG has no task-specific functional groups (e.g. amines) to chemically interact with CO₂. Thus, CO₂-induced swelling in PEG-base NOHMs can be considered as a consequence of CO₂ physisorption of CO₂ in NOHMs. For NOHMs with varied grafting densities, four NOHMs with different grafting densities (1.0, 2.0, 2.5 and 3.8 chains/nm²) were prepared. CO₂ capture capacity and CO₂-induced swelling of NOHMs were measured by Attenuated Total Reflectance (ATR) Fourier-transform infrared (FT-IR) Spectrometer. (Flichy et al., 2001; Pasquali et al., 2008)

5.2 Experimental

5.2.1 Synthesis of NOHMs and Ionized PEG

NOHMs of various chain lengths were prepared according to the procedures discussed in Chapter 4. Mono-amine terminated polyethylene glycol (PEG) (MW = 1000 ~ 5000 g/mol, PDI < 1.08, purity > 95%) and 3-(trihydroxysilyl)-1-propane sulfonic acid (THOPS) were diluted with deionized water into 10 wt% solutions. While monitoring the pH, the THOPS solution was added dropwise to the PEG solution. Equivalence point plots were also employed to ensure the 1:1 ratio of sulfonate groups/amine groups. Finally, to obtain the final Ionized PEG, water was removed under vacuum at 35 °C.

NOHMs of varied grafting densities (1.0, 2.0, 2.5 and 3.8 chains/nm²) were synthesized using the same method as described above. Sulfonic acid-functionalized nanoparticle suspension was prepared with 7 nm nanoparticles. The polyetheramine (Jeffamine M2070) solution was added dropwise to the functionalized silica suspension while monitoring the pH. Four different amounts of Jeffamine 2070 solution were added in order to obtain NOHMs with different grafting densities (3.8, 2.5, 2.0 or 1.0 chains/nm²). The highest grafting density corresponded to the addition of polyetheramine up to the equivalent point. Finally, NOHMs samples were dried under vacuum at 35 °C for about 48 hours.

NOHMs samples are referred to as NOHM-I-HPE-n, where n corresponds to the grafting density in chains/nm². As defined in Chapter 3, “I” stands for “Ionic” and indicates the type of bonding between the corona and the canopy, while “HPE” refers to polyetheramine (“PE”) with a high (“H”) ether group content. For Jeffamine 2070, the ethylene oxide/propylene oxide ratio is 31/10. In the following, the starting silica colloidal suspension will be referred to as “7 nm SiO₂ suspension”, the silane solution as “linker solution”, and the polyetheramine as “Jeffamine 2070”.

5.2.2 CO₂ Capture Capacity and CO₂-induced Swelling Behavior

CO₂ capture capacity was calculated using Beer–Lambert law was used, which expresses the relationship between the absorbance (A), the absorptivity (ϵ), the concentration (c), and the infrared path length (d). Since the internal reflection at the interface between the crystal surface and the specimen causes an evanescent electric field which undergoes exponential decay in its intensity, an effective thickness of the evanescent wave (d_e) is considered (Harrick 1967). The resulting Beer–Lambert law is described as the equation (3-1), $A = \epsilon \cdot c \cdot d_e$, where d_e is the arithmetical mean between the effective path length for perpendicular ($d_e \perp$) and parallel ($d_e \parallel$) polarization. For calculation of d_e , the refractive indices of NOHMs were measured by a refractometer. The absorbance of CO₂ was quantified by measuring the intensity of ν_3 band (ca. 2338 cm⁻¹, CO₂ asymmetric stretching mode), and its molar absorptivity at high-pressure was 1.0×10^6 cm²/mol. (Maiella et al., 1999) The CO₂-induced swelling of NOHMs was calculated by the equation (3-2).

5.2.3 Raman Spectroscopy

Raman spectra were collected at room temperature using a LabRAM ARAMIS spectrometer (Horiba Jobin Yvon) equipped with a microscope and a 50× objective. A solid-state frequency doubled YAG 532 nm laser and 1200 gr/mm grating were used for this study. The exposure time was set at 20 seconds and 5 scans were collected for each sample to improve the signal-to-noise ratio. Experiments were performed on the as-synthesized/as-received materials deposited on a glass slide in the range 400-4000 cm⁻¹.

5.3 Results and discussion

5.3.1 Effect of Chain Length on CO₂ Capture Capacity

CO₂ capture capacity and CO₂-induced swelling of NOHMs were simultaneously obtained from the ATR FT-IR spectrometer. (Flichy et al., 2001; Pasquali et al., 2008; Park et al., 2011) Since PEG1K, PEG2K and PEG5K are amine-terminated PEGs that react with CO₂ to form carbamate, methoxy-polyethylene glycols (mPEG) were selected to substitute the amine-terminated PEGs for the CO₂ capture capacity and CO₂-induced swelling experiments in order to quantify physisorbed CO₂ in NOHMs. CO₂ capture capacities of NOHMs and their corresponding mPEGs are shown in Figure 5-1. The silica nanoparticles used in the synthesis of NOHMs were nonporous (Meeks, Rankin et al. 2010) and, thus silica nanoparticles were not considered as active components of CO₂ capture. Therefore, the capacity of NOHMs shown here is based on the organic component of NOHMs, which was considered as a “solvent.”

As seen in Figure 5-1, PEGs of different lengths capture almost the same amount of CO₂. This is because CO₂ solubility is strongly related to the amount of ether groups which form Lewis acid–base interactions with CO₂ (Lin and Freeman 2004), and for a given mass of PEG the same number of ether groups is present regardless of the length of the polymer. In Figure 5-1, however, the CO₂ capture capacities of NOHMs were slightly lower than those of mPEGs. There is also an observable effect of chain length on the CO₂ capture capacity of NOHMs, where NOHMs with a shorter chain have a slightly lower CO₂ capture capacity than NOHMs with longer chains. This difference may be attributed to the existence of alkoxysilane (THOPS) in NOHMs, which was used to modify the nanoparticles surface. Since THOPS did not contain any ether and the amine of the amine-terminated PEG was protonated by the functional group of alkoxysilane, the organic component (“solvent”) of NOHMs does not contain as many active

groups/sites for CO₂ capture as PEGs of comparable mass. Therefore, NOHMs have lower CO₂ capture capacity than mPEGs and the existence of the alkoxysilane had the most significant effect on the CO₂ capture capacity of NOHMs with the shortest chain (e.g. NOHM-I-PEG1K-E).

5.3.2 Effect of Chain Length on CO₂-induced Swelling

As discussed earlier, NOHMs prepared in the study are PEG-based NOHMs, which do not contain task-specific functional groups (e.g. primary amine, secondary amine and tertiary amine) for CO₂ capture. Thus CO₂ was captured by NOHMs by physisorption, which can cause CO₂-induced swelling in NOHMs. Figure 5-2 shows the CO₂ capture capacity of NOHMs and mPEGs as a function of CO₂-induced swelling. All mPEGs exhibited comparable swelling % for a given CO₂ capture capacity, suggesting the insignificant effect of chain length on the CO₂-induced swelling behavior of unbound PEG polymers. However, once a PEG was grafted onto the surface-modified nanoparticles, the swelling % for a given CO₂ capture capacity was reduced compared to its corresponding unbound mPEG for a given CO₂ capture capacity. Such a reduction in swelling for a given CO₂ capture capacity may be caused by the conformational difference between NOHMs and unbound polymers. Unlike in unbound polymers for which polymer chains can move freely, the polymer chains in NOHMs are tethered onto the surface-modified nanoparticles, and thus they are constrained and are forced to stretch out to fill the space between the nanoparticles. Therefore, a more orderly orientation of polymer chains may be expected in NOHMs than the unbound polymer chains ^(Park et al., 2011). The frustration undergone by the polymer chains in NOHMs may result in a distinct pattern of CO₂ packing between polymer chains; therefore allowing more CO₂ molecules to be captured (Park et al., 2011). Another noticeable trend in Figure 5-2 is that, for a given CO₂ capture capacity, the shorter the

chain length, the smaller the swelling percentage. This suggests that the frustration undergone in the polymer chain of NOHMs is more pronounced when the length of polymer chain is shorter. Another interesting feature found in Figure 5-2 is that for each mPEG, an equal amount of CO₂ captured (~0.2 mmol/g) resulted in comparable CO₂-induced swelling percentages. However, for the three different NOHMs, every increase in CO₂ capture capacity (0.2 mmol-CO₂/g-solvent) produced distinct values in swelling percentages.

In order to further explore this swelling feature, the amount of swelling percentage caused by 0.2 mmol/g CO₂ capture capacity is defined as delta swelling to calculate a ratio of delta swelling of mPEG to a delta swelling of NOHMs with the same chain length. A plot of the ratio was drawn as a function of CO₂ capture capacity, shown in Figure 5-3. It shows the effect of chain length on the deviation between CO₂-induced swelling behavior of mPEG and NOHMs. With the shortest chain in this study, mPEG1K and NOHM-I-PEG1K-E exhibited notably distinct swelling behaviors with the ratio of 1.8 at the low CO₂ capture capacity. On the other hand, mPEG5K and NOHM-I-PEG5K have a ratio very close to 1 at the low CO₂ capture capacity, indicating the less-distinct CO₂-induced swelling behaviors in the two materials. Interestingly, when more CO₂ was captured, the ratio in each case was closer to 1, suggesting that at high CO₂ loading, the CO₂-induced swelling behaviors of mPEG and NOHMs are comparable to each other. This also implies that the conformational structure in NOHMs initially allows more CO₂ to be captured in NOHMs with the same volume change as mPEG. Then, as the conformational difference between NOHMs and mPEG diminishes due to continual packing of CO₂, NOHMs start to behave similarly to mPEG in CO₂-induced swelling behaviors.

The higher delta swelling ratio in NOHM-I-PEG1K-E than NOHM-I-PEG5K can be attributed to the more ordered structure in NOHM-I-PEG1K-E. In order to investigate whether

the polymer chains in NOHM-I-PEG1K-E are more ordered, Raman spectroscopy was employed to probe the conformation of mPEG and NOHMs. Raman spectroscopy has been proposed to determine the conformational order of linear molecules (Larsson and Rand 1973; Orendorff et al., 2002). By analyzing Raman spectra of polymers, some indicators can be used to correlate the conformational change of linear molecules to various conditions and manipulations. Figure 5-4 shows a typical Raman spectrum of PEG (PEG1K). Since CH₂ group is the backbone unit of PEG, the intensity ratio of $\nu_a(\text{CH}_2)$ band (asymmetric stretching mode, $\sim 2850 \text{ cm}^{-1}$) to $\nu_s(\text{CH}_2)$ band (symmetric stretching mode, $\sim 2885 \text{ cm}^{-1}$) has been an indicator to correlate the conformational order (Orendorff et al., 2002).

Spectra of PEG and NOHMs with various chain lengths in the $\nu_a(\text{CH}_2)$ and $\nu_s(\text{CH}_2)$ regions were obtained without introducing CO₂ and are shown in Figure 5-5. The ratio of $I[\nu_a(\text{CH}_2)]$ to $I[\nu_s(\text{CH}_2)]$ in each spectrum was calculated and plotted in Figure 5-6. The ratios of $I[\nu_a(\text{CH}_2)]$ to $I[\nu_s(\text{CH}_2)]$ of PEGs were comparable to each other, indicating an insignificant effect of chain length on the conformational order for unbound polymers. However, once PEG was grafted onto the surface-functionalized nanoparticles to form NOHMs, the ratio of $I[\nu_a(\text{CH}_2)]$ to $I[\nu_s(\text{CH}_2)]$ of each NOHM-I-PEG was notably higher than that of PEG. This implies that the polymer chains of NOHMs have a higher conformational order than that of PEG, which may be due to the frustration undergone by the polymer chains in NOHMs. The higher conformational order in NOHMs may be the explanation for the distinct CO₂-induced swelling between NOHMs and PEG. Furthermore, while comparing to the $I[\nu_a(\text{CH}_2)]/I[\nu_s(\text{CH}_2)]$ of three PEGs, NOHM-I-PEG1K-E showed the highest increase among three NOHMs, followed by NOHM-I-PEG2K-E and NOHM-I-PEG5K-E. Such a trend may be the reason for the highest ratio of delta swelling of PEG1K to NOHM-I-PEG1K-E found in Figure 5-3. Considering this knowledge of the effect of

chain lengths on the conformational order and CO₂-induced swelling, NOHMs can be optimized to capture CO₂ with significantly less volume change, therefore minimizing the reactor volume.

5.3.3 Effect of Grafting Density on CO₂ Capture Capacity

Prior to the structural investigation of NOHMs' canopy, the grafting densities of NOHMs samples were estimated using a TGA method. As designed, NOHMs exhibited grafting densities ranging from 1 to 3.8 chains/nm² (details given in Table 5-1). The range of the grafting densities was selected considering similar work conducted on polymer brushes (Sander et al., 2005) to cover a sufficiently large range to allow for the identification of distinct structural arrangements in NOHMs.

Generally, about 4.5~5 OH groups/nm² are observed on the surface of silica. Therefore, the estimated grafting density of NOHM-I-HPE-3.8 seems reasonable. The lower bound of the grafting density was limited to 1.0 chains/nm² due to the increase in NOHMs' viscosity. Since the same 7 nm silica nanoparticles were used throughout NOHMs' synthesis, the core fraction increased with decreased grafting density, and thus, the viscosity of NOHM-I-HPE-1.0 was significantly higher than that of NOHM-I-HPE-3.8.

¹H NMR spectra of the synthesized NOHMs are presented in Figure 5-7. The dominant peak of the H atoms in CH₂ is found at about 3.6 ppm, in addition to three other H peaks that are most relevant to the identification of NOHMs' structure. The peak at about 3.3 ppm is attributed to H on the terminal CH₃, denoted H_a, and that at 1.1 ppm corresponds to H on CH₃ along propylene oxide units, referred to as H_b. A small peak at about 1.25 ppm (1.15 ppm for NOHM-I-HPE-3.8) represents H on CH₃ close to the terminal amine side of the polymer chain, assigned as H_c. The locations of these H atoms are graphically marked in Figure 5-7. In the case of NOHMs, the H_c

peak was found upfield compared to H_b , while in the unbound polymer (Jeffamine 2070) it was downfield compared to H_b , as also shown in a previous study (Park et al., 2011). This feature was the consequence of the protonation of the amine via ionic reaction with the sulfonate group, confirming both the successful tethering of Jeffamine 2070 onto the functionalized nanoparticles and the absence of unbound (excess) polymers. It is also interesting to observe that the peak shift to upfield was more pronounced for NOHMs with lower grafting densities.

Further evidence of the protonation of the amine groups and the absence of unbound polymer was obtained via ^{13}C NMR analysis as shown in Figure 5-8. The ^{13}C NMR spectrum of NOHM-I-HPE-3.8 exhibits a dominant peak at approximately 70 ppm along with side peaks around 68 ppm which are related to C atoms in CH_2 of the ethylene oxide portion of Jeffamine 2070. The peaks from the C atoms in CH_2 of the propylene oxide portion of Jeffamine 2070 are observed near 75 ppm. Finally, C atoms from CH_3 of the propylene oxide portion of the polymeric canopy are seen at 16 ppm. After exposure to 0.7 MPa CO_2 , a new peak appeared at 125 ppm which was consistent with the presence of physisorbed CO_2 (Abbott et al., 1982). The important feature to notice is the absence of the carbamate peak which is generally located around 162 ppm (Blasucci et al., 2009). The presence of the carbamate peak would have indicated the reaction between CO_2 and the amine group of Jeffamine 2070, which in this study was used for ionic bonding and not for CO_2 capture. Thus, these results suggest the absence of unbound polymer and the successful attachment of the Jeffamine 2070 to the functionalized cores via acid-base reaction.

The entanglement of tethered polymer chains and their interactions can be investigated using 2D ROESY NMR spectroscopy. This method enables the identification of through-space interactions between H atoms which are indicated by the presence of blue off-diagonal peaks on the NMR spectra (Bigler 2000). The grafted polymer chains showed significantly fewer

interactions among polymer chains compared to those of unbound polymers, and this impacted the CO₂ capture and CO₂-induced swelling behaviors of NOHMs. In this study, the grafting density of NOHMs was varied to further investigate the interaction between tethered polymer chains and its influences on the CO₂ capture mechanisms and capacity as well as the swelling and CO₂ packing behaviors.

According to the 2D ROESY NMR results shown in Figure 5-9, H_b and H_c atoms (of CH₃ along the chains and CH₃ close to the amine, respectively) showed significant through-space interactions with H and H_a atoms (of CH₂ and the terminal CH₃, respectively) for NOHMs with higher grafting densities. This ROEs was reduced as the grafting density was lowered. This trend continues to the lowest grafting density of 1.0 chains/nm². In other words, the intensity of interactions between polymer chains decreased as grafting density decreased. This is evidenced by the lowered ratio of intensities of a diagonal peak to the studied peak (off-diagonal peak) from 0.29 to unmeasurable level as the grafting density was reduced from 3.8 to 1.0 chains/nm². The absence of a correlation peak in the case of NOHM-I-HPE-1.0 may be due to the near surface covering of polymeric canopies on the inorganic cores which could lower the NMR intensities. However, the polymers used in this study are quite large in size (~MW 2000), and thus, this phenomena is less likely. Even at the lowest grafting density, the tethered polymer chains seem to stretch out to fill the gap between nanoparticle cores rather than covering the surface of the nanoparticles.

Next, NOHMs samples with different grafting densities as well as the silica precursor colloidal solution, the linker solution and Jeffamine 2070 were also analyzed using Raman spectroscopy. Figure 5-10(a) shows the full spectra while Figure 5-10(b) exhibits the details of the CH₂ stretching region of the spectra. The SiO₂ suspension spectrum did not exhibit any

predominant peaks due to the dilute nature of the silica colloidal suspension. On the other hand, several bands were visible on the spectrum of the linker solution. The most predominant bands can be assigned to: Si–O–Si symmetric stretching (530 cm^{-1}) (Ishida et al., 1982), CH_2 rocking ($800\text{--}900\text{ cm}^{-1}$) (Koenig and Angood 1970), SO_3^- stretching (1050 cm^{-1}) (Edwards et al., 2000), CH_2 bending ($1420, 1460\text{ cm}^{-1}$) (Orendorff et al., 2002), CH_2 symmetric and asymmetric stretching (2890 cm^{-1} and 2935 cm^{-1}), and O–H stretching from water (3450 cm^{-1}). The bands for Jeffamine 2070 can be attributed to: CH_2 rocking ($800\text{--}900, 930, 1045\text{ cm}^{-1}$) (Koenig and Angood 1970; Orendorff et al., 2002), C–C and C–O stretching ($930, 1045, 1135\text{ cm}^{-1}$), CH_2 twisting ($1245, 1290\text{ cm}^{-1}$), CH_2 wagging and CH_3 bending (1350 cm^{-1}), CH_2 bending (1460 cm^{-1}), CH_2 symmetric and asymmetric stretching (2875 cm^{-1} and 2935 cm^{-1}) (Koenig and Angood 1970; Orendorff et al., 2002), and NH_2 symmetric and asymmetric stretching (3310 cm^{-1} and 3375 cm^{-1}) (Mayo et al., 2004). As expected, the spectra of NOHMs samples exhibited features of both the spectra of the linker solution and Jeffamine 2070. More precisely, the main bands from Jeffamine 2070 were all observed for NOHMs samples and some bands from the linker solution appeared as well. The bands associated with the linker solution included Si–O–Si symmetric stretching (530 cm^{-1}), SO_3^- stretching (1050 cm^{-1}) and CH_2 bending (1420 cm^{-1}).

Many studies have reported the use of Raman spectroscopy to study the conformational order and the intermolecular interactions, or chain coupling, in polymers especially in polymer brushes (Orendorff et al., 2002; Sander et al., 2005). A commonly used spectral indicator of the conformational structure is the Raman shift value (position of a peak) of CH_2 symmetric stretching vibration, ν_{s,CH_2} , where an increase in ν_{s,CH_2} is a sign of decreased chain coupling (Ducey et al., 2002). As shown in Figure 5-11, the Raman shift value of CH_2 symmetric stretching vibration was increased as the grafting density was reduced. This indicates that fewer

intermolecular interactions were present in NOHMs with lower grafting densities. This trend is in agreement with the earlier 2D ROESY NMR data. Moreover, in all cases less chain coupling was observed for NOHMs samples compared to unbound polymer. This suggests that tethered polymer chains in NOHMs were likely more structured (i.e., better aligned) than the corresponding unbound polymer. Such effect likely originated from the specific structure of NOHMs. The polymer chains in NOHMs' canopies are grafted onto the functionalized nanoparticles in the absence of solvent, and thus, they are forced to stretch out to fill out the interparticle space. For unbound polymers, such limitations do not exist, and therefore, a more random configuration with increased chain coupling occurs.

Another spectral indicator for NOHMs systems is the intensity ratio of the asymmetric to symmetric stretching vibrations of CH_2 , $I(\nu_{\text{a,CH}_2})/I(\nu_{\text{s,CH}_2})$. The higher intensity ratio means greater conformational order (Ducey et al., 2002; Sander et al., 2005). The intensity ratios shown in Figure 5-11 were derived from the data given in Figure 5-10(b), and the results suggest that a greater conformational ordering occurred for NOHMs with lower grafting densities. Such behavior seems counter-intuitive and differs from the results reported for polymer brushes (Ducey et al., 2002). The discrepancy can be attributed to the structural difference between NOHMs and polymer brushes. While polymer chains in polymer brushes are grafted onto a flat surface, those in NOHMs are grafted onto a surface with high curvature. Consequently, the force that drives polymer chains to align in the case of polymer brushes is not likely to play an important role in the structure of the polymer chains in NOHMs. In case of NOHMs, the physical state of the materials could have significantly influenced the conformational ordering of the tethered polymer chains (Orendorff et al., 2002). NOHM-I-HPE-3.8, which was synthesized with the highest fraction of polymeric component, exhibited the lowest viscosity, whereas NOHM-I-

HPE-1.0 contained the least amount of polymers and thus, resembled more gel-like/solid-like compounds. Therefore, at the same temperature, a greater ordering would be expected for NOHMs with lower grafting densities (Orendorff et al., 2002). It should not be excluded that the higher intensity ratio, $I(\nu_{a,CH_2})/I(\nu_{s,CH_2})$, for the linker solution could also participate to this effect. However, based on the deconvolution performed on NOHMs' spectra, this effect was found to be relatively small. Finally, it is worth noting that, for all NOHMs samples, $I(\nu_{a,CH_2})/I(\nu_{s,CH_2})$ for all NOHMs samples were greater than that for the unbound polymer. As explained for the ν_{s,CH_2} shift, this behavior must be related to the specific configuration of NOHMs, which induced greater ordering of the polymer chains. The higher ratio observed in NOHMs compared to the unbound polymer is similar to the trends reported in the case of polymer brushes versus bulk polymer (Sander et al., 2005).

ATR FT-IR spectroscopy was employed to further provide information on the induced changes in intermolecular conformation of NOHMs. Figure 5-12(a) shows the ATR FT-IR spectra for NOHMs samples along with precursor materials (i.e., nanoparticle suspension, linker solution and unbound precursor polymer). For the 7 nm SiO₂ suspension, Si–O–Si stretching vibration was easily identified at 1105 cm⁻¹, and OH bending and stretching vibration from water were observed at 1620 cm⁻¹ and 3300 cm⁻¹, respectively (Almeida et al., 1990; Lide 1993). The linker solution spectrum exhibited broad overlapping bands in the region 800~1250 cm⁻¹ which can be assigned to Si–O–C stretching (Que et al., 2000), SO₃⁻ stretching (Kazarian et al., 1996) and CH₂ bending. OH bending and stretching vibrations were also observed at 1650 cm⁻¹ and 3400 cm⁻¹ (Lide 1993). The main features of Jeffamine 2070's spectrum included broad bands around 1050 cm⁻¹ and 2850 cm⁻¹ which correspond to C–O and CH₂ stretching vibrations, respectively (Lide 1993). The spectra of NOHMs were quite similar to that of Jeffamine 2070.

The difference between the spectra of NOHMs and Jeffamine 2070 should be associated with the presence of the linker. For instance, the band at about 1050 cm^{-1} appears as an overlap of two bands: one at 1075 cm^{-1} originating from the polymer and the other at 1035 cm^{-1} likely related to the linker. This hypothesis is also supported by the increase in the intensity of the latter band with a decrease in the grafting density, which is in accordance with the higher portion of unreacted silane linkers.

Upon exposure to 5.5 MPa CO_2 , significant changes in the ATR FT-IR spectra of NOHMs were observed as seen in Figure 5-12(b). These changes have been described in a previous study (Park et al., 2011) and include the appearance of CO_2 stretching and bending vibrations at about 2330 cm^{-1} (ν_3) and 670 cm^{-1} (ν_2), respectively. The current structural investigation was conducted on the CO_2 bending peaks since the CO_2 bending mode exhibited greater change during CO_2 capture. The bending mode of vapor CO_2 usually appears as a sharp band centered around 670 cm^{-1} (Kazarian et al., 1996; Yuan and Teja 2011). However, as shown in previous works conducted on various polymers exposed to CO_2 , a shift and loss of double degeneracy of the CO_2 bending band occurred as a result of Lewis acid–base interactions between CO_2 and the carbonyl or ether groups along the polymer chains which act as electron-donors for CO_2 (Kazarian et al., 1996; Yuan and Teja 2011). This CO_2 bending mode of polymer- CO_2 system thus appeared as a rather broad band which was comprised of two bands corresponding to the in-plane ($\sim 650\text{ cm}^{-1}$) and out-of-plane ($\sim 660\text{ cm}^{-1}$) bending modes of CO_2 (Kazarian et al., 1996; Yuan and Teja 2011). Such feature was also observed in the case of NOHMs since the functionality of the polymeric canopy (i.e., ether groups) was preserved in NOHMs.

Varying the grafting density of NOHMs' canopy would alter the chain coupling, and thereby offer a new way to tune the solvating properties of NOHMs. This phenomenon was specifically

investigated by focusing on the ATR FT-IR bending modes of absorbed CO₂ in NOHMs of various grafting densities as it can provide insight into CO₂ packing behaviors in NOHMs. As shown in Figure 5-13, the intensity of CO₂ bending vibration increased with CO₂ pressure and grafting density. Considering that the main CO₂ capture mechanism is related to the intermolecular interactions between CO₂ and the ether groups along the polymeric canopy, the bending mode of CO₂ was deconvoluted into in-plane and out-of-plane modes as illustrated in Figure 5-13 (Kazarian et al., 1996). The area ratios between the two corresponding bands were then calculated for each case in Figure 5-13, and the results are presented in Figure 5-14. All NOHMs samples exhibited a higher area ratio than that of corresponding unbound polymer.

Moreover, the magnitude of the area ratio increased with the CO₂ pressure in the case of NOHMs with the lowest value around 3, while it remained below 3 in the case of Jeffamine 2070. It is interesting to note that recent *ab initio* calculations performed for phosphorous containing compounds with similar Lewis acid-based interactions with CO₂ have revealed that the absorbance of in-plane mode of CO₂ is 3 times higher than the absorbance of out-of-plane mode. These results suggest that the different intermolecular interactions (i.e., chain coupling) and local structural conformations between NOHMs and unbound canopy led to distinct physicochemical properties such as CO₂ packing pattern or vibrational dynamics of CO₂ associated with ether groups. Since the amount of CO₂ absorbed in NOHMs and polymers might have influenced the area ratio and since different materials would likely have different CO₂ capture capacities, the relationship between the area ratios and CO₂ capture capacities for the studied materials was also investigated (Figure 5-14). These CO₂ capture capacities were obtained using the ATR FT-IR spectroscopy method as previously mentioned in Section 3.2. Briefly, the CO₂ capture capacity calculation involves the materials' density and refractive index ($n_D = 1.54$ for NOHMs and $n_D =$

1.52 for Jeffamine 2070), the angle of incidence of the light ($\theta = 43^\circ$), and the absorbance of the CO_2 asymmetric stretching vibration before and after exposure to CO_2 ($\sim 2330 \text{ cm}^{-1}$). It is important to note that CO_2 capture capacity is given in mmol of CO_2 per gram of solvent where the solvent refers to the polymeric fraction of NOHMs. The CO_2 capture capacities for NOHM-I-HPE-2.0 and NOHM-I-HPE-1.0 could not be estimated due to the high viscosities of these materials at 25°C that did not allow for the precise measurement of their densities. NOHMs tested in this study did not contain any task-specific functional groups and it is thus expected that higher CO_2 uptakes than those reported here can be reached when amine groups are present along the polymer chain of NOHMs' canopy. This is supported by the results presented in a previous paper by Lin and Park (Lin and Park 2011). As seen from Figures 5-14 (a) and (b), the area ratios for NOHMs significantly differ from that of Jeffamine 2070 as a function of both CO_2 pressure and CO_2 capture capacity which confirms the existence of a distinct packing behavior between NOHMs and unbound polymer.

Recently, Yuan and Teja reported the frequency order of possible vibrational modes in the range of $\nu_2(\text{CO}_2)$ for the electron donor-acceptor complexes (Yuan and Teja 2011). In particular, they suggested the occurrence of free CO_2 bending vibration (CO_2 not strongly associated with electron donor groups) between the out-of-plane and in-plane bending modes of CO_2 . Although the peak assignment in the region of CO_2 bending modes is still under discussion, the existence of differences between bound and unbound canopies is clearly valid. However, the change in the CO_2 packing behavior in NOHMs' canopy was not significantly influenced by the grafting density of NOHMs. More details on the assignments of the CO_2 bending mode peaks is subject to future investigation.

It is anticipated that the CO₂ packing behavior would also influence the CO₂-induced swelling in NOHMs and polymers. In Section 3.2, it was found that the sorption of CO₂ in NOHMs causes a specific swelling behavior. Thus, the current ATR FT-IR results were investigated further to evaluate the swelling behavior of the materials studied.

As mentioned in Section 3.2, when using ATR FT-IR measurement, S can be expressed as equation (3-2), where A^0 , d_e^0 , A , and d_e are the absorbance and the effective pathlengths without and with CO₂, respectively. The absorbance of C-H ($\sim 2850\text{ cm}^{-1}$) bands was selected for the swelling measurements. It was assumed that the absorptivity was not significantly affected by the concentration of CO₂ at different pressures, and thus, the change in the effective thickness was considered to be negligible. The results are presented in Figure 5-15 for different NOHMs and Jeffamine 2070 as a function of CO₂ pressure. For all samples, the degree of swelling increased with the CO₂ pressure. As expected, the degree of swelling also increased with the grafting density of NOHMs and NOHMs with the highest grafting density (NOHM-I-HPE-3.8) exhibited a swelling behavior quite similar to that of Jeffamine 2070. It is believed that the different swelling behaviors among various NOHMs and unbound polymers are the result of the different configurations of the polymer chains. Greater ordering of the polymer chains, as evidenced above, may create “unoccupied” space where CO₂ can be absorbed without significant volume changes. The relationship between CO₂ capture capacity and CO₂-induced swelling was then investigated. The results shown in Figure 5-15 confirm the distinct CO₂-induced swelling behaviors between the unbound polymer and NOHMs and also between NOHMs with different grafting densities although the effect is less pronounced. For instance, at the CO₂ capture capacity of 3 mmol of CO₂ per gram of solvent, the unbound polymer swelled about 12% more than NOHM-I-HPE-3.8, while NOHM-I-HPE-3.8 exhibited only 4% more volume increase

compared to that of NOHM-I-HPE-2.5, which may be due to the small difference in their grafting densities. The differences between swelling percentages became more significant as the CO₂ loading increased. It should be noted that the swelling measurement technique used was indirect and the results obtained are mostly used to indicate qualitative trends between the different NOHMs and between NOHMs and unbound polymer, rather than to point out specific values of swelling. All these results support that the greater ordering of the polymer chains in NOHMs compared to the unbound polymer favors the formation of “unoccupied” spaces available for CO₂ absorption. Moreover, a lower grafting density seemed to favor greater ordering of NOHMs’ canopy and resulted in reduced swelling during CO₂ capture.

5.4 Conclusions

CO₂ capture capacity of NOHMs and CO₂-induced swelling were simultaneously measured via the ATR FT-IR spectrometer. Regarding CO₂-induced swelling, NOHMs showed notably less swelling than their corresponding unbound polymers at a given CO₂ capture capacity. While shorter polymer chains, NOHMs exhibited even less swelling with shorter polymer chains at a given CO₂ capture capacity. This may be due to the conformational difference between NOHMs and unbound polymer, allowing more CO₂ molecules to pack within the polymer chains. For NOHMs with varied grafting densities, the differences (i.e., increased chain ordering and decreased intermolecular interactions in NOHMs compared to unbound polymer) were further pronounced by lowering the grafting density of NOHMs’ canopy. These differences were attributed to the specific structural configuration of NOHMs’ canopy in which polymer chains were tethered onto inorganic nanoparticle cores causing more “rigid” arrangements than that of bulk polymer. This particular structural change in NOHMs resulted in different CO₂ packing and

CO₂-induced swelling behaviors in novel hybrid materials compared to corresponding unbound polymer.

Table 5-1 List of NOHMs samples with their compositions and grafting densities determined by thermogravimetric analyses.

Sample	Core fraction (wt%)	Grafting density (chains/nm ²)
NOHM-I-HPE-3.8	17	3.8
NOHM-I-HPE-2.5	24	2.5
NOHM-I-HPE-2.0	29	2.0
NOHM-I-HPE-1.0	44	1.0

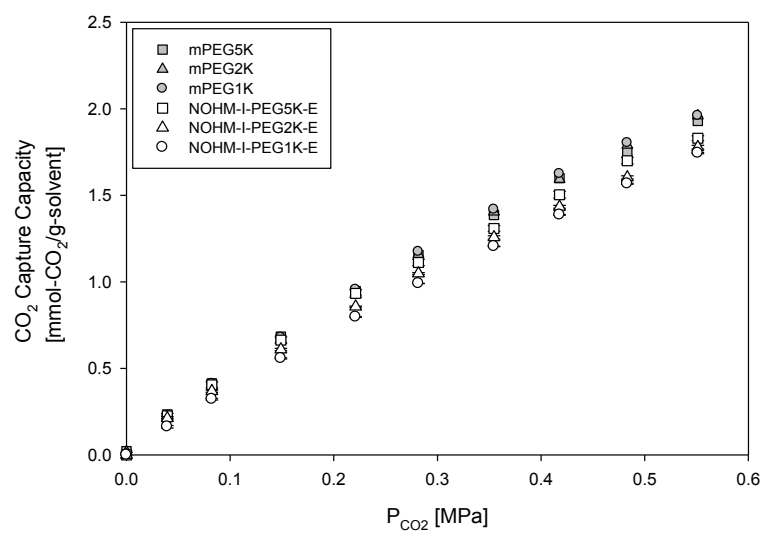


Figure 5-1 CO₂ solubility in NOHMs with various chain length at 60 °C and P_{CO₂}= 0.4 – 5.5 MPa.

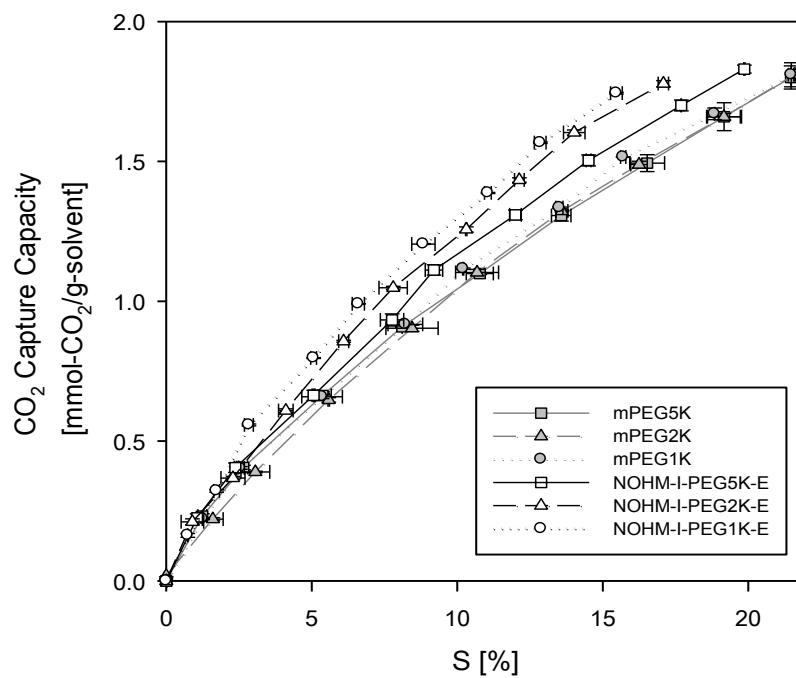


Figure 5-2 CO₂ capture capacity and CO₂-induced swelling of NOHM-I-HPE with various molecular weights of PEGs and the corresponding pure PEGs.

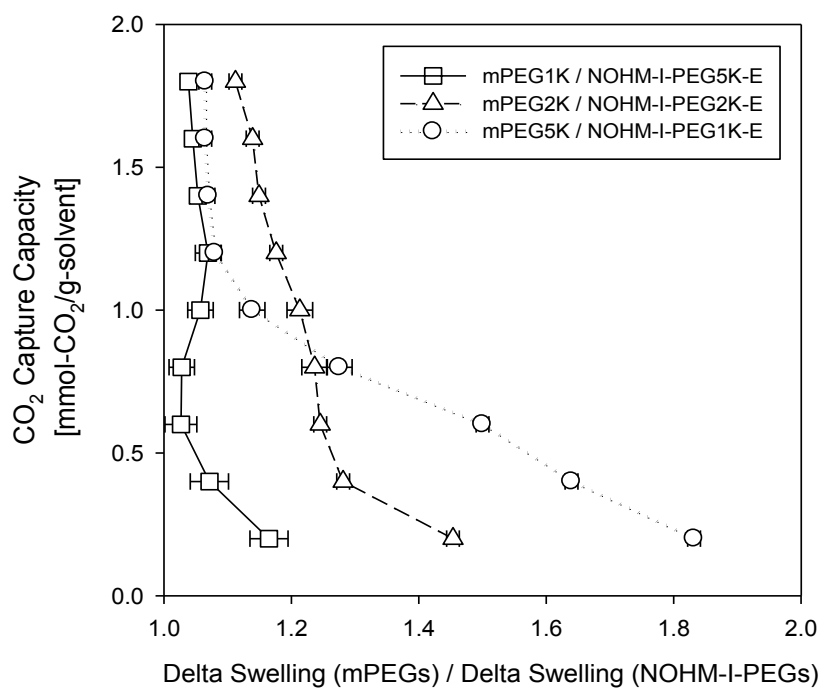


Figure 5-3 Ratios of delta swelling of mPEG to NOHM-I-PEGs at 60 °C and $P_{\text{CO}_2} = 0.8 - 5.5$ MPa. (Amount of swelling percentage caused by 0.2 mmol/g CO_2 capture capacity is defined as a delta swelling)

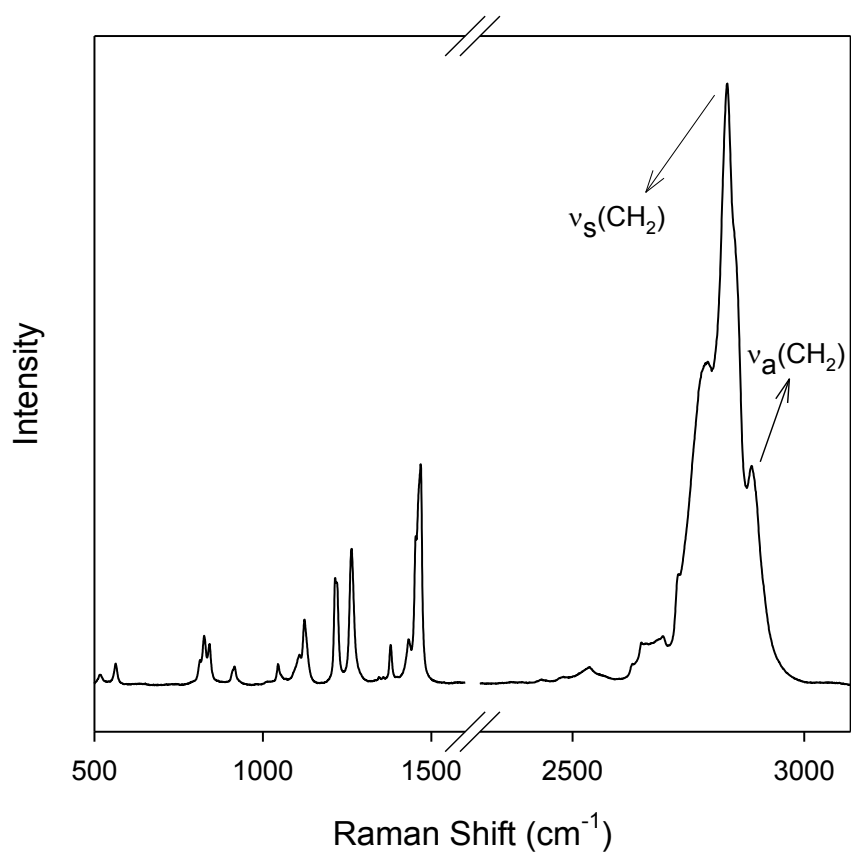


Figure 5-4 A typical Raman spectrum of NOHM-I-HPE

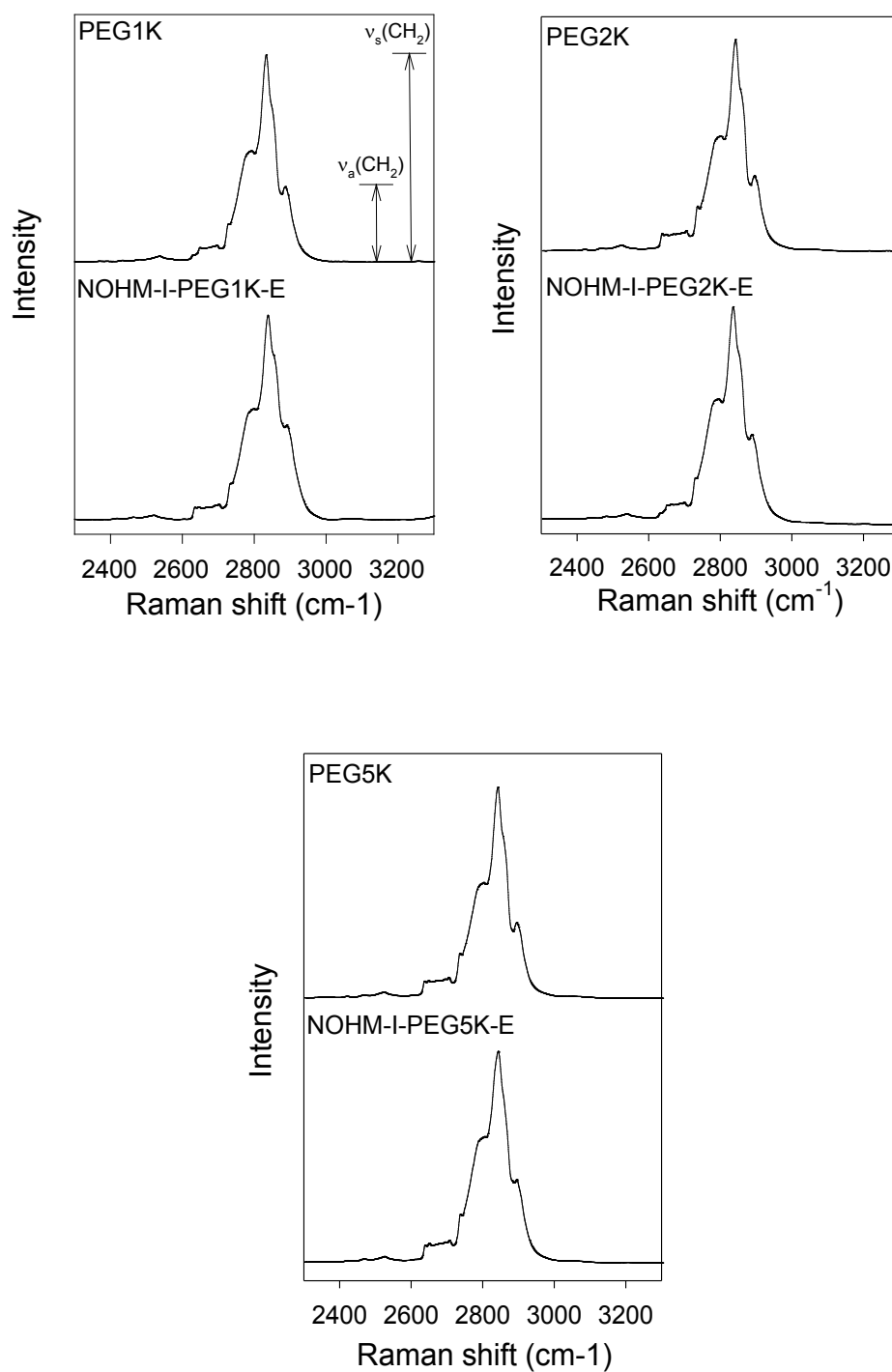


Figure 5-5 Raman spectra in the $\nu_a(\text{CH}_2)$ and $\nu_s(\text{CH}_2)$ regions for PEGs and NOHM-I-PEGs.

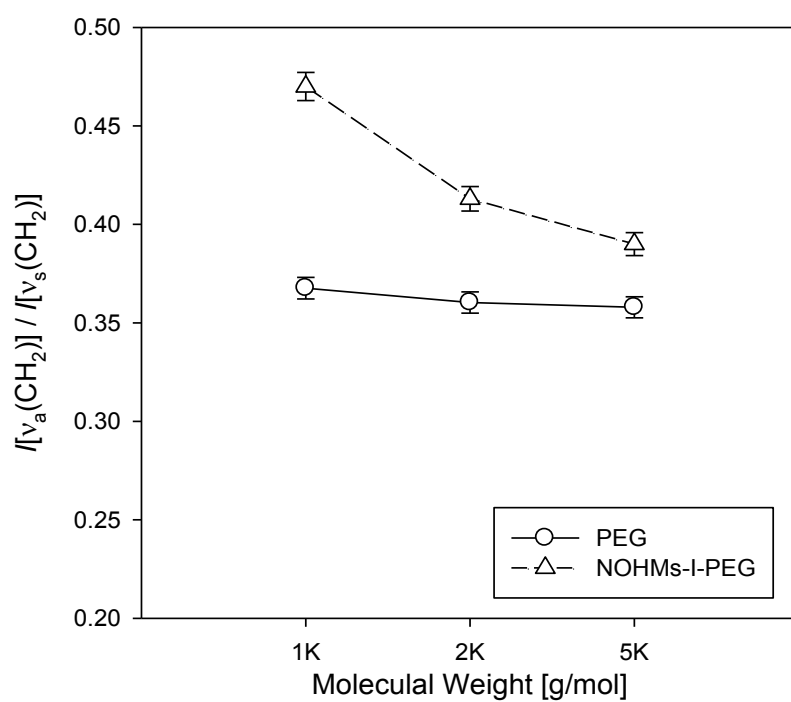


Figure 5-6 Ratios of Raman spectral intensity of $\nu_a(\text{CH}_2)$ to $\nu_s(\text{CH}_2)$ for PEGs and NOHM-I-PEGs at various molecular weights.

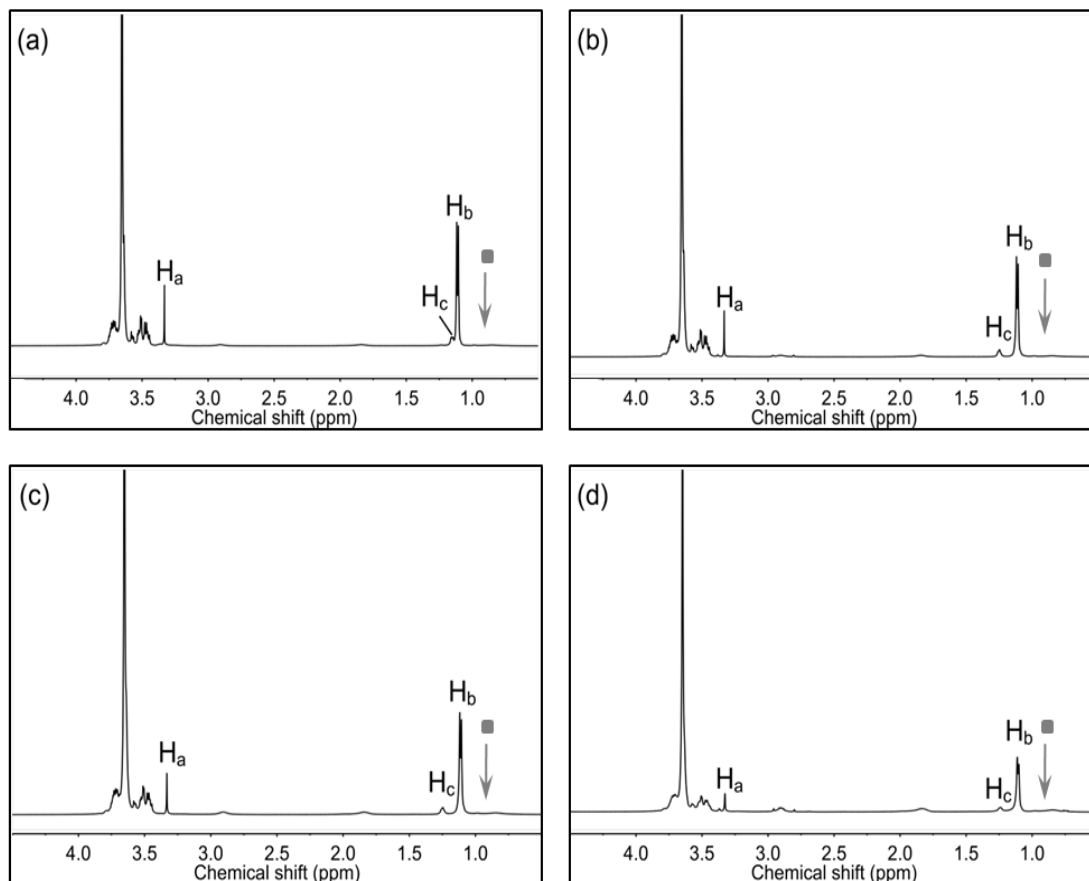


Figure 5-7 Confirmation of ionic bonding between the linker and Jeffamine 2070 provided by ^1H NMR spectra of: (a) NOHM-I-HPE-3.8, (b) NOHM-I-HPE-2.5, (c) NOHM-I-HPE-2.0 and (d) NOHM-I-HPE-1.0 at 27 °C. All samples were prepared in D_2O . The symbol ■ indicates the location of the H_c peak in the unbound Jeffamine 2070.

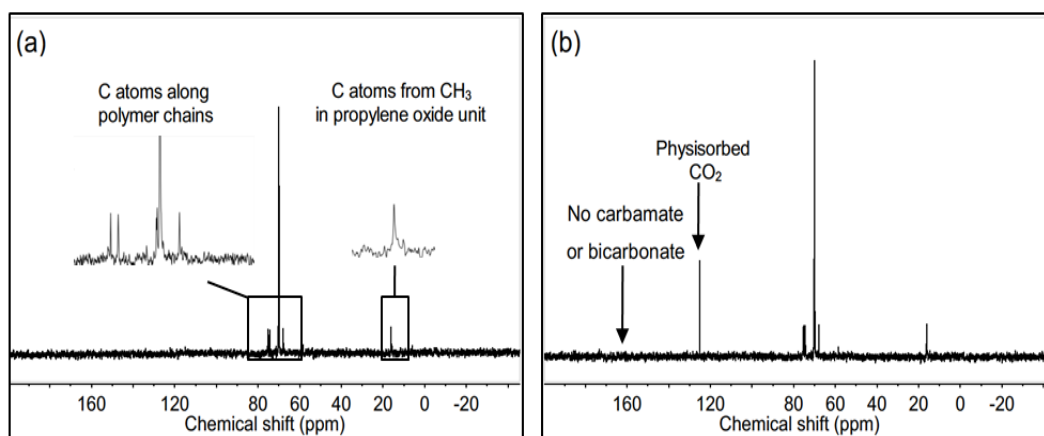


Figure 5-8 ^{13}C NMR spectra of NOHM-I-HPE-3.8 in D_2O : (a) before and (b) after exposure to CO_2 (~ 0.7 MPa) at 27°C .

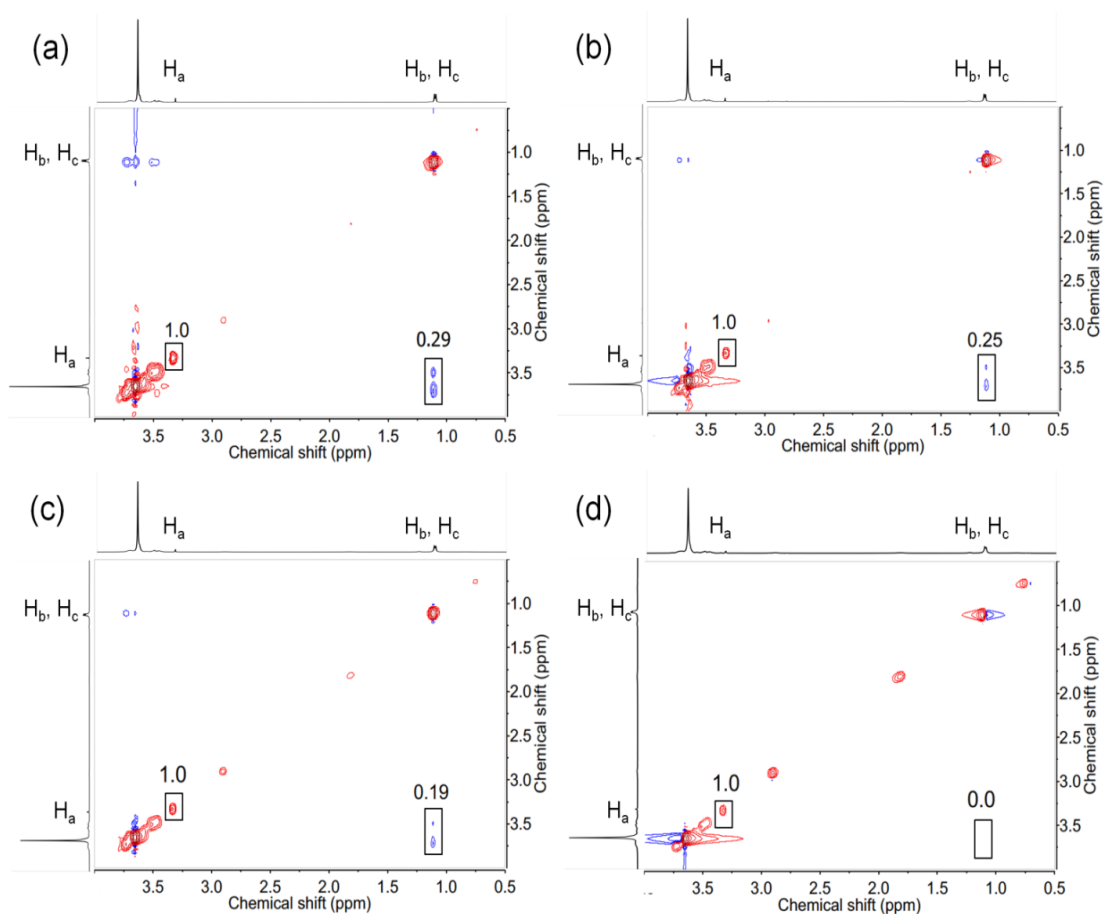


Figure 5-9 2D ROESY NMR spectra of: (a) NOHM-I-HPE-3.8, (b) NOHM-I-HPE-2.5, (c) NOHM-I-HPE-2.0 and (d) NOHM-I-HPE-1.0 in D_2O at 27 °C. Numbers on each graph indicate the integrated intensities. The red contours correspond to diagonal and TOCSY (Total Correlation Spectroscopy, off-diagonal) peaks, while the blue contours exhibit ROEs.

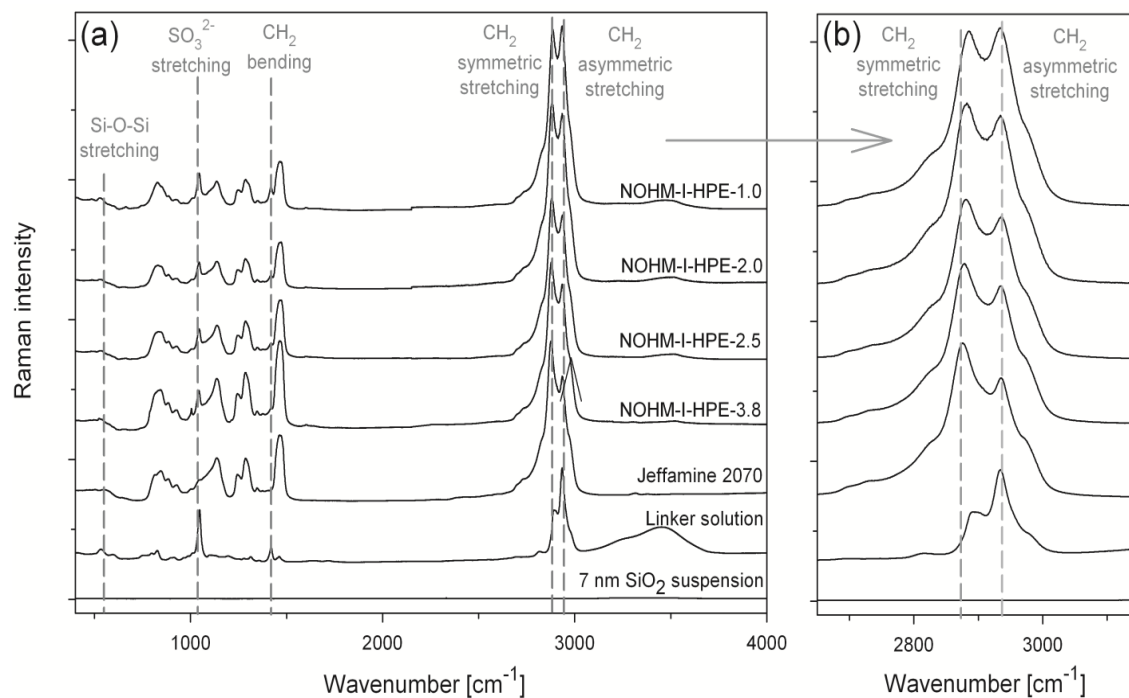


Figure 5-10 Raman spectra of NOHMs with various grafting densities (3.8, 2.5, 2.0 and 1.0 chains/nm²): (a) full spectra, and (b) CH₂ stretching region at 25 °C.

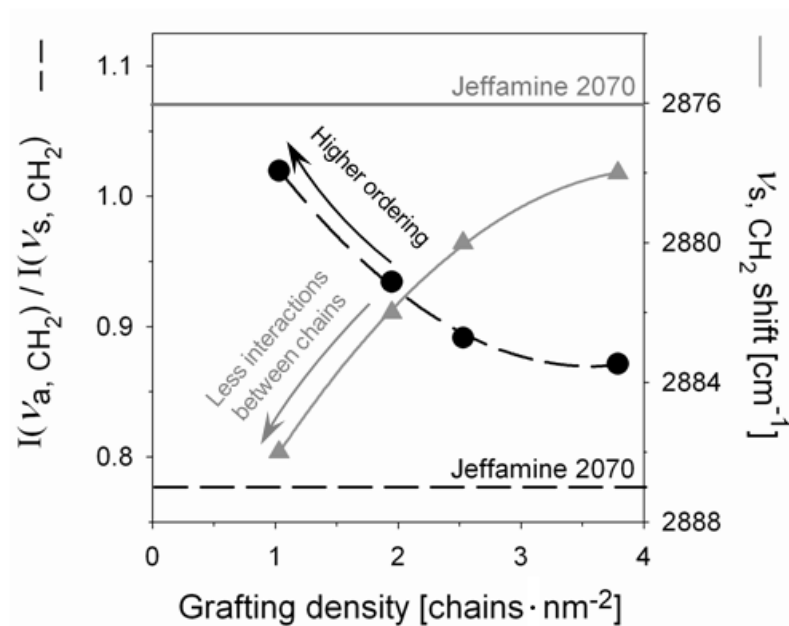


Figure 5-11 Effect of grafting density on the ν_{s, CH_2} shift and the intensity (I) ratios of symmetric to asymmetric stretching of CH_2 in NOHMs and unbound polymer.

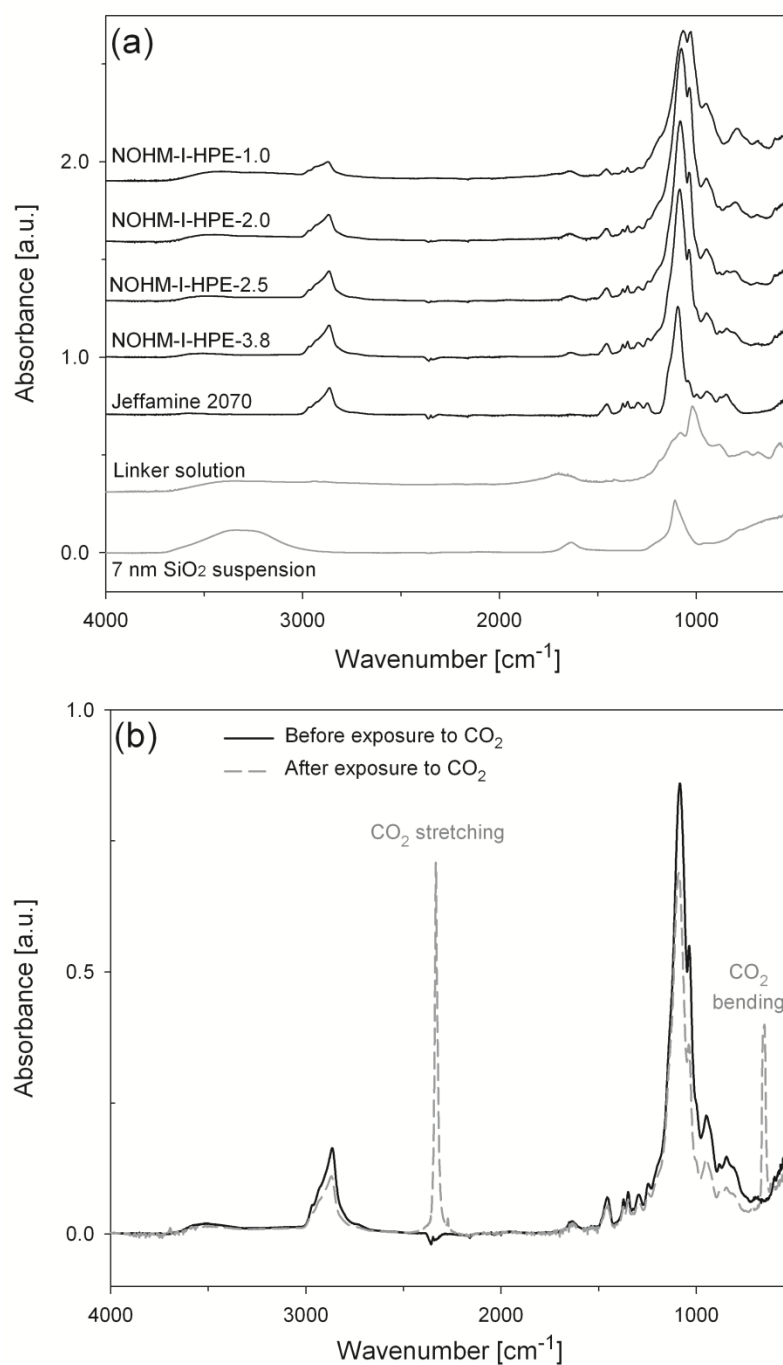


Figure 5-12 ATR FT-IR spectra of: (a) NOHMs with various grafting densities (3.8, 2.5, 2.0 and 1.0 chains/ nm^2) before exposure to CO_2 , and (b) NOHM-I-HPE-3.8 before and after exposure to CO_2 (5.5 MPa, 25 $^\circ\text{C}$).

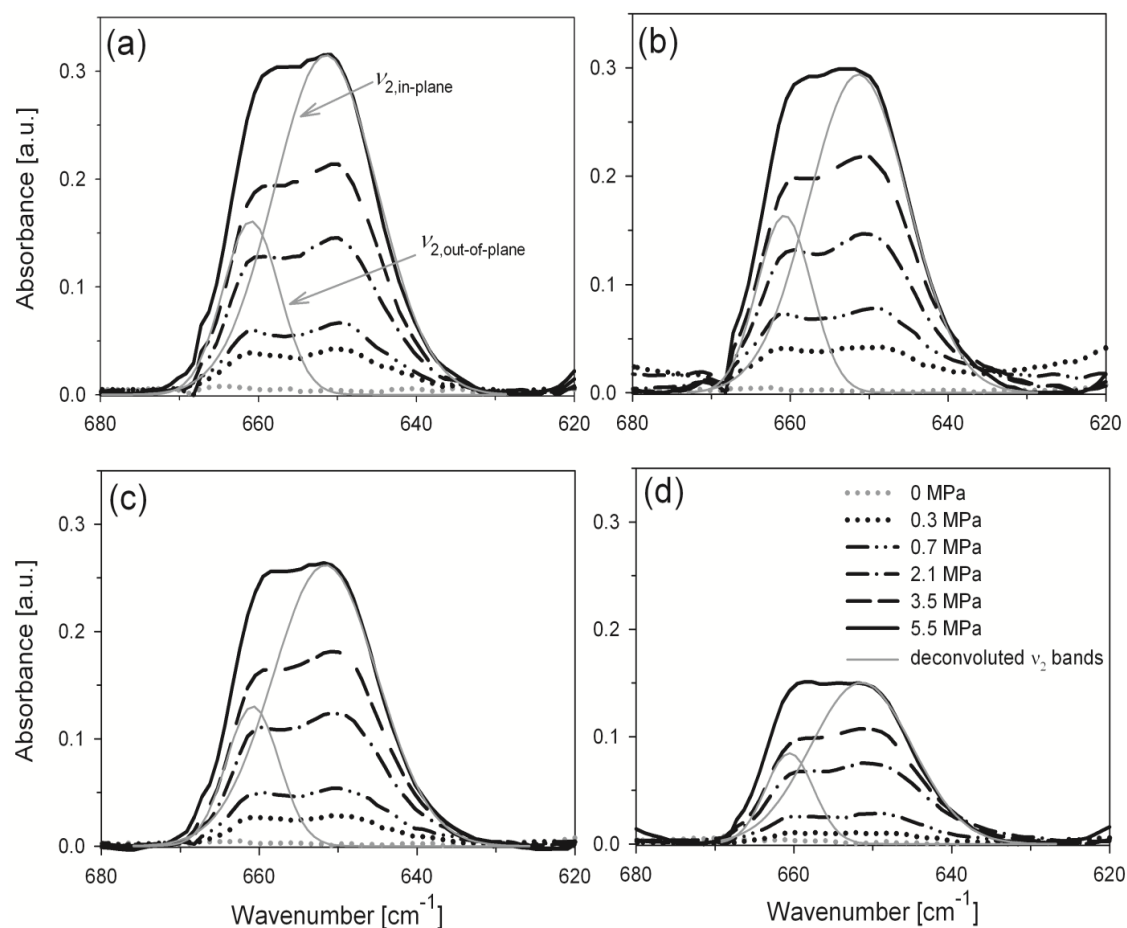


Figure 5-13 ATR FT-IR spectra of ν_2 bending modes of CO₂ absorbed in NOHMs with various grafting densities (3.8, 2.5, 2.0 and 1.0 chains/nm²): (a) NOHM-I-HPE-3.8, (b) NOHM-I-HPE-2.5, (c) NOHM-I-HPE-2.0 and (d) NOHM-I-HPE-1.0 at 25 °C.

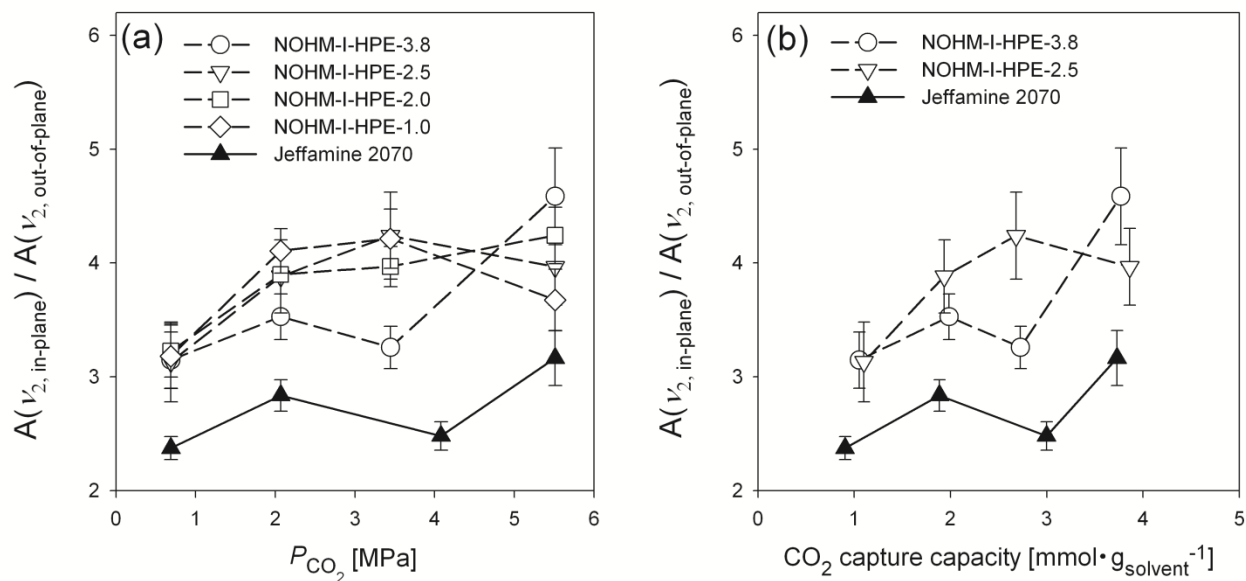


Figure 5-14 Area (A) ratios of in-plane ($\nu_{2, \text{in-plane}}$) to out-of-plane ($\nu_{2, \text{out-of-plane}}$) bending modes of CO_2 absorbed in NOHMs with different grafting densities (3.8, 2.5, 2.0 and 1 chains/ nm^2) and in Jeffamine 2070 as a function of: (a) CO_2 pressure, and (b) CO_2 capture capacity at 25 °C.

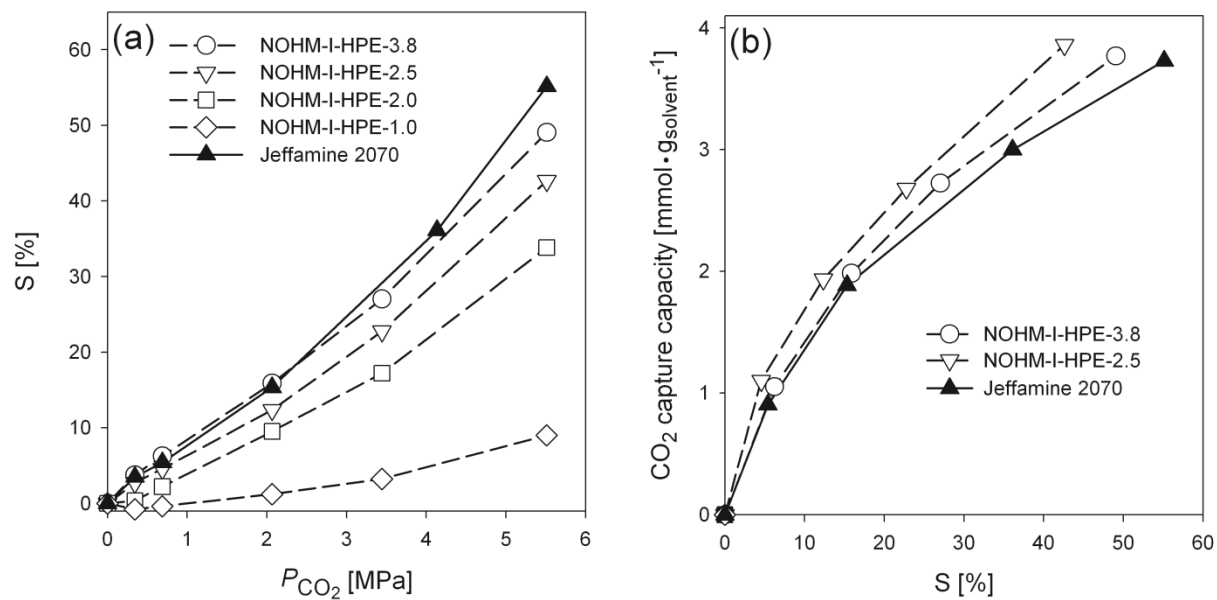


Figure 5-15 CO₂-induced swelling (S) behaviors of NOHMs (grafting densities = 3.8, 2.5, 2.0 and 1 chains/nm²) and Jeffamine 2070 at 25 °C (a) as a function of CO₂ pressure, and (b) CO₂ capture capacity.

Reference

- Abbott, T. M., Buchanan, G. W., Kruus, P. and Lee, K. C., " ^{13}C nuclear magnetic resonance and Raman investigations of aqueous carbon dioxide systems", *Canadian Journal of Chemistry*, 60 1000-1006, 1982.
- Almeida, R. M., Guiton, T. A. and Pantano, C. G., "Characterization of silica gels by infrared reflection spectroscopy", *Journal of Non-Crystalline Solids*, 121, 193-197, 1990.
- Bigler, P., "NMR spectroscopy: processing strategies", *Wiley-VCH: Weinheim*, 2000.
- Blasucci, V., Dilek, C., Huttenhower, H., John, E., Llopis-Mestre, V., Pollet, P., Eckert, C. A. and Liotta, C. L., "One-component, switchable ionic liquids derived from siloxylated amines", *Chemical Communications*, 116-118, 2009.
- Ducey, M. W., Orendorff, C. J., Pemberton, J. E. and Sander, L. C., "Structure-Function Relationships in High-Density Octadecylsilane Stationary Phases by Raman Spectroscopy. 2. Effect of Common Mobile-Phase Solvents", *Analytical Chemistry*, 74, 5585-5592, 2002.
- Edwards, H. G. M., Brown, D. R., Dale, J. A. and Plant, S., "Raman spectroscopy of sulfonated polystyrene resins", *Vibrational Spectroscopy*, 24, 213-224, 2000.
- Flichy, N. M. B., Kazarian, S. G., Lawrence, C. J. and Briscoe, B. J., "An ATR-IR Study of Poly (Dimethylsiloxane) under High-Pressure Carbon Dioxide: Simultaneous Measurement of Sorption and Swelling", *The Journal of Physical Chemistry B*, 106, 754-759, 2001.
- Harrick, N. J., *Internal reflection spectroscopy*, Interscience Publishers: New York, NY, 1967.
- Ishida, H., Chiang, C.-h. and Koenig, J. L., "The structure of aminofunctional silane coupling agents: 1. γ -Aminopropyltriethoxysilane and its analogues", *Polymer*, 23, 251-257, 1982.
- Kazarian, S. G., Vincent, M. F., Bright, F. V., Liotta, C. L. and Eckert, C. A., "Specific Intermolecular Interaction of Carbon Dioxide with Polymers", *Journal of the American Chemical Society*, 118, 1729-1736, 1996.
- Koenig, J. L. and Angood, A. C., "Raman spectra of poly(ethylene glycols) in solution", *Journal of Polymer Science Part A-2: Polymer Physics*, 8, 1787-1796, 1970.
- Larsson, K. and Rand, R. P., "Detection of changes in the environment of hydrocarbon chains by raman spectroscopy and its application to lipid-protein systems", *Biochimica et Biophysica Acta (BBA) - Lipids and Lipid Metabolism*, 326, 245-255, 1973.
- Lide, D. R., "CRC handbook of chemistry and physics", *CRC Press, Boca Raton, FL* 1993.
- Lin, H. and Freeman, B. D., "Gas solubility, diffusivity and permeability in poly(ethylene oxide)", *Journal of Membrane Science*, 239, 105-117 2004.
- Lin, K.-Y. A. and Park, A.-H. A., "Effects of Bonding Types and Functional Groups on CO_2 Capture using Novel Multiphase Systems of Liquid-like Nanoparticle Organic Hybrid Materials", *Environmental Science & Technology*, 45, 6633-6639, 2011.
- Maiella, P. G., Schoppelrei, J. W. and Brill, T. B., "Spectroscopy of Hydrothermal Reactions. Part XI: Infrared Absorptivity of CO_2 and N_2O in Water at Elevated Temperature and Pressure", *Applied Spectroscopy*, 53, 351-355, 1999.
- Mayo, D. W., Miller, F. A. and Hannah, R. W., "Course notes on the interpretation of infrared and Raman spectra", *John Wiley and Sons: Hoboken, NJ*, 2004., 2004.
- Meeks, N. D., S. Rankin, et al., "Sulfur-Functionalization of Porous Silica Particles and Application to Mercury Vapor Sorption" *Industrial & Engineering Chemistry Research* 49(10), 4687-4693, 2010.

- Orendorff, C. J., Ducey, M. W. and Pemberton, J. E., "Quantitative Correlation of Raman Spectral Indicators in Determining Conformational Order in Alkyl Chains", *The Journal of Physical Chemistry A*, 106, 6991-6998, 2002.
- Park, Y., Decatur, J., Lin, K.-Y. A. and Park, A.-H. A., "Investigation of CO₂ capture mechanisms of liquid-like nanoparticle organic hybrid materials via structural characterization", *Physical Chemistry Chemical Physics*, 13, 18115-18122, 2011.
- Pasquali, I., Andanson, J.-M., Kazarian, S. G. and Bettini, R., "Measurement of CO₂ sorption and PEG 1500 swelling by ATR-IR spectroscopy", *The Journal of Supercritical Fluids*, 45, 384-390, 2008.
- Que, W., Sun, Z., Zhou, Y., Lam, Y. L., Chan, Y. C. and Kam, C. H., "Optical and mechanical properties of TiO₂/SiO₂/organically modified silane composite films prepared by sol-gel processing", *Thin Solid Films*, 359, 177-183, 2000.
- Sander, L. C., Lippa, K. A. and Wise, S. A., "Order and disorder in alkyl stationary phases", *Analytical and Bioanalytical Chemistry*, 382, 646-668, 2005.
- Yuan, Y. and Teja, A. S., "Quantification of specific interactions between CO₂ and the carbonyl group in polymers via ATR-FTIR measurements", *The Journal of Supercritical Fluids*, 56, 208-212, 2011.

CHAPTER 6

EFFECTS OF BONDING TYPES AND FUNCTIONAL GROUPS OF NOHMs ON CO₂ CAPTURE

This chapter has been published as:

K.-Y. A. Lin and A.-H. A. Park, “Effects of Bonding Types and Functional Groups on CO₂ Capture in Novel Multiphase Systems of Liquid-like Nanoparticle Organic Hybrid Materials (NOHMs)”, *Environmental Science & Technology*, 45 (15), 6633–6639, 2011.

6.1 Introduction

NOHMs have been demonstrated to show enhanced thermal stability and unique solvation properties (CO₂-induced swelling and packing behaviors). Earlier versions of the liquid-like hybrid solvents were developed and referred as NIMs (Nanoparticle-based Ionic Materials). NIMs were synthesized via an acid-base reaction between amine and sulfonate groups of polymer chains. (Bourlinos 2005; Bourlinos 2005; Rodriguez 2008). In this chapter, types of NOHMs were broadened and five specific NOHMs were prepared (as shown in Figure 3-1): NOHM-I-HPE, NOHM-I-PEI, NOHM-I-tPE, NOHM-C-HPE, NOHM-C-MPE. Both the effects of bonding types (i.e., ionic and covalent bonds) and functional groups (i.e., ether and amine groups) of NOHMs on CO₂ capture were investigated in terms of their thermal stability, CO₂ capture capacity, selectivity and solvent recyclability.

6.2 Experimental

6.2.1 Chemicals

Silica nanoparticles of 10-15 nm diameter suspended in methanol (MT-ST) and water (Ludox HS-30) were provided by Nissan Chemicals and Sigma Aldrich, respectively. Two different suspensions were used based on the miscibility of selected polymeric corona. For polymeric corona, two mono-amine terminated polyetheramines, Jeffamine M-2070 (HPE) and M-2005 (MPE). ethylene oxide (EO) / propylene oxide (PO) in HPE and MPE were 31/10 and 6/29, respectively. Tertiary amine (ethylenediamine tetrakis (ethoxylate-block-propoxylate) tetrol, M.W.~7200) and polyethylenimine (M.W.~1800) were obtained from Huntsman and Polysciences Inc. (3-glycidyloxypropyl) trimethoxysilane and 3-(trihydroxysilyl)-1-propane

sulfonic acid were selected as linker (coupling agents), while the Dowex HCR-W2 ion exchange resin was employed during the synthesis of NOHMs.

6.2.2 Synthesis of NOHMs via Ionic Bond (NOHM-I-HPE, NOHM-I-tPE and NOHM-I-PEI)

NOHM-I-HPE was prepared according to the procedures described in Chapter 4 (Section 4-2). In case of NOHM-I-tPE and NOHM-I-PEI, they were synthesized without linkers, and thus, their preparation steps were slightly different from that of NOHM-I-HPE. Ludox HS-30 was diluted with deionized water to obtain 3 wt% silica suspension. First, Na^+ of the prepared silica suspension was replaced by protons using an ion exchange column. While monitoring the reaction pH to reach the equivalent point of 6, NOHM-I-tPE was prepared by adding 10 wt% tertiary amine (tPE) solution to the functionalized silica suspension. In case of NOHM-I-PEI, due to the large quantity of amine functional groups in the system, the reaction pH did not provide information on the extent of reaction. Therefore, the functionalized silica suspension was mixed with the polymeric solution based on the desired core/canopy ratio. The extent of acid-base reaction as well as the confirmation of ionic bonds was carried out via a thermogravimetric analysis (TGA). The main difference between NOHM-I-tPE and NOHM-I-PEI was the existence of the task-specific functional groups in the latter material.

NOHM-Cs were prepared via covalent bond as follows. 3 wt% HPE and MPE solutions in ethanol were prepared and a molar equivalence of (3-glycidyloxypropyl) trimethoxysilane was added to each solution. HPE and MPE were selected based on the amount of ether groups in polymeric chains (i.e., high (HPE) and moderate (MPE)). The polyether-silane solutions were then stirred at room temperature for 12 hours to ensure complete reaction. The silica suspension

prepared in the similar manner as for NOHM-I-HPE was added dropwise into each polyether-silane solution and the resulting mixture was stirred for 5 hours and dialyzed (MWCO 3.5k) against deionized water for 48 hours to remove excess polyether-silane. In all cases, to obtain the final NOHMs products, water was removed under reduced pressure at 35 °C to obtain the final NOHMs. Figure 3-1 (bottom) also illustrates the representative structures of prepared NOHMs.

6.2.3 CO₂ Capture using NOHMs

The synthesized NOHMs were characterized for physical and chemical properties using a series of analytical tools including TEM, FTIR and TGA. Each FT-IR spectrum from 4000 to 600 cm⁻¹ was averaged over 16 scan at 8 cm⁻¹ resolution for both pure polymer and NOHMs samples. A high pressure reactor system was constructed with a temperature control (shown in Figure 6-1) in order to evaluate the CO₂ capture capacity of NOHMs. The internal volume of the each reactor chamber was 15 ml and sample holders were designed so that it can hold about 0.15 g of thin layer of a NOHMs sample to minimize mass transfer problems. The loaded sample holder was placed into the high pressure chamber which was equipped with an on-line pressure transducer. Before each run, any air or gas in the loaded reactor was removed by applying vacuum ($P_{\text{vacuum}} = 0.00025$ MPa). A selected gas (i.e., CO₂, N₂, N₂O, or O₂) was introduced at a desired pressure (0.1 ~ 0.34 MPa) and temperature (30 ~ 70 °C) and the equilibrium CO₂ capture capacity was then calculated based on the pressure drop using the ideal gas law.

6.3 Results and Discussion

6.3.1 Characterization of NOHMs

Synthesized NOHMs samples were analyzed using the FT-IR to verify the reaction between the primary amines and the surface functional groups of the nanoparticle cores (i.e., ionic bond with sulfonate groups for NOHM-I and covalent bond with glycidyl ether groups for NOHM-C). As shown in Figure 6-2(a), the protonated amine peaks confirming the formation of ionic bonding between the polyetheramine and the sulfonate groups were found at 1530 cm^{-1} ($\delta_s(\text{NH}_3^+)$) and at 1630 cm^{-1} ($\delta_a(\text{NH}_3^+)$). The ^{13}C NMR result of NOHM-I-HPE in DMSO- d_6 (experimental condition: $^{13}\text{CO}_2$ at $P_{\text{CO}_2} = 0.5\text{ MPa}$ and room temperature) (Figure 6-3) also suggested that CO_2 sorption by NOHMs was mainly due to physisorption rather than chemisorption. In other words, the amine functional groups of the polyetheramines were entirely consumed during the synthesis of NOHMs and the bonds between the nanoparticle core and the grafted polymer chains were very stable. Furthermore, NOHMs samples did not contain any unreacted free polymers. In case of NOHM-C-HPE, the formation of the polyether-silane was confirmed by the disappearance of a band at 3056 cm^{-1} ($\nu_{\text{C-H}}$ epoxy) and the presence of hydroxyl groups at $3400\sim 3600\text{ cm}^{-1}$ (Figure 6-2 (b)). The similar patterns of FT-IR spectra were found for NOHM-C-MPE and its corresponding polyether-silane.

6.3.2 Thermal Stabilities of NOHMs

As polymer chains were tethered onto the surface of nanoparticles, their thermal stability was improved, and this was confirmed from the thermal decomposition experiments performed using a TGA (Figure 6-4). According to the mass change during the thermal swing, all five NOHMs samples (i.e., NOHM-I-HPE, NOHM-C-HPE, NOHM-C-MPE, NOHM-I-tPE and NOHM-I-PEI)

illustrated 10 – 40 °C improvement in their thermal stability for given mass changes compared to their corresponding polymers. The improvements in NOHM-C-HPE and NOHM-C-MPE were relatively smaller than those in NOHM-I-HPE (THOPS). The difference may be due to that 3-(trihydroxysilyl)-1-propane sulfonic acid has higher thermal stability than that of (3-Glycidyloxypropyl)trimethoxysilane. In other words, the coupling agents have significant effects on the thermal stability of synthesized NOHMs. Compared to the thermal decomposition curves of NOHM-I-HPE, NOHM-C-HPE, NOHM-C-MPE, and NOHM-I-tPE, the thermal decomposition curves of PEI and NOHM-I-PEI resulted in faster reduction in mass with the same temperature ramping program because polyethylenimine (PEI) has greater volatility than polyetheramines (HPE and MPE). This implies that the selection of the polymeric chains would also strongly affect the range of the operating conditions of synthesized NOHMs. Similar thermal improvement was observed for NOHM-I-tPE, which was prepared via grafting ethylenediamine tetrakis(ethoxylate-block-propoxylate) onto negatively charged silica nanoparticles. The improvements in thermal stabilities of NOHMs investigated in this study were varied from as low as 10 °C to as high as 40 °C. These are very promising results for CO₂ capture at elevated temperatures of flue gas. Unlike MEA solutions, all NOHMs samples synthesized using polyetheramines showed excellent thermal stabilities with no weight drop until the onset of their thermal decomposition, indicating negligible vapor pressure over a wide range of operating temperatures. According to the experimental results, the thermal stability of NOHMs can be further optimized by selecting different polymers and linkers.

6.3.3 Effects of Temperature and Pressure on CO₂ Capture using NOHMs

Since the silica nanoparticles used in this study for the preparation of NOHMs were nonporous (Meeks, Rankin et al. 2010), the CO₂ capture in NOHMs was considered to be essentially attributed to the liquid soft materials, the polymeric canopy. Therefore, CO₂ solubilities in NOHMs were expected to follow Henry's law; a linear relationship of CO₂ solubility in NOHMs with respect to the partial pressure of CO₂. A higher CO₂ capture capacity is expected at a higher partial pressure of CO₂. Besides the pressure, temperature also has a significant effect on the CO₂ solubility in NOHMs. Therefore, like other CO₂ capture solvents, NOHMs' CO₂ capture capacity increased with an increase in the partial pressure of CO₂ while the operating temperature showed an adverse effect. The quantity of pure CO₂ stream produced from this separation process would be a function of the slopes of the data shown in Figures 6-5 and 6-6, and be directly proportional to the differences between initial and final CO₂ pressures and temperatures. For example, according to the data given in Figure 6-5, 0.4 mol of CO₂ can be captured by 1 kg of solvent (corona portion of NOHM-C-HPE) at $P_{\text{CO}_2} = 0.32$ MPa. By exposing this CO₂-rich NOHM-C-HPE to $P_{\text{CO}_2} = 0.13$ MPa where NOHM-C-HPE's CO₂ capture capacity is only 0.18 mmol-CO₂/g-solvent, 0.22 mmol of CO₂ can be released as the separated product stream. The CO₂-lean NOHM-C-HPE is then recycled back to the capture reactor for the next separation cycle.

For both pressure and temperature swings, NOHMs synthesized via covalent bond (NOHM-C-HPE) resulted in higher CO₂ capture capacities than those synthesized via ionic bond (NOHM-I-HPE). This was due to the availability of the secondary amine groups in NOHM-C-HPE as previously discussed. If both NOHMs contained the same amount of amine functional groups, the resulting CO₂ capture capacities would have been similar. In both cases of NOHM-I-

HPE and NOHM-C-HPE, HPE is an ether-based polymer, and the ether groups in both NOHMs participated in CO₂ absorption owing to its dipole–quadrupole interaction (Lin and Freeman 2004; Lin and Freeman 2005). However, for the operating conditions given in Figures 6-5 and 6-6, NOHM-C-HPE captured as high as 50% more CO₂ than NOHM-I-HPE while there was only one amine group but 41 ether groups per HPE chain. This implies that the task-specific functional groups such as amine groups are much more effective at CO₂ capture than ether groups. This phenomenon will be further discussed in a later section. Stronger interaction between CO₂ and NOHMs would result in a greater CO₂ capture capacity; however, it could also result in higher energy requirement for solvent regeneration.

6.3.4 Absorption Selectivity of Gases in NOHMs

In addition to the high capture capacity, one of the most important factors required for any capture medium is its selectivity towards the gas of interest, in this case CO₂. With the promising CO₂ capture capacities of NOHMs, a series of subsequent experiments were designed to evaluate the solubilities of other gases in NOHMs samples that exist in flue gas such as nitrogen (N₂) and oxygen (O₂). Nitrous oxide (N₂O) was also evaluated because N₂O is similar to CO₂ in terms of molecular configuration, electronic structure and molecular volume, but different in terms of chemical reactivity with NOHMs' amine groups. In NOHM-I-HPE, CO₂ exhibited the highest solubility among the tested gases, followed by N₂O (Figure 6-7). Oxygen was found to be slightly soluble in NOHM-I-HPE while N₂ appeared to be almost insoluble. Since the solubility of gases in liquid phase is governed by the interaction between gaseous and liquid molecules, high solubilities of CO₂ and N₂O in NOHM-I-HPE were expected due to their relatively high quadrupole moments (Ghosal et al., 1996). Although the solubilities of CO₂ and

N₂O in NOHM-I-HPE were comparable, a significant difference was presented in the solubilities of CO₂ and N₂O in NOHM-C-HPE (Figure 6-8). This difference could be explained by the existence of the secondary amines in NOHM-C-HPE which can chemically react with CO₂ but not with N₂O. Since NOHM-I-HPE and NOHM-C-HPE both exhibited high selectivity towards CO₂ over N₂, which is the major gaseous component in flue gas, NOHMs have a great potential as a CO₂ capture medium from flue gas or any other gaseous mixtures of CO₂ and inert gases.

6.3.5 Recyclability of NOHMs during CO₂ Capture and Solvent Regeneration Cycles

Another desirable characteristic of CO₂ capture medium is recyclability because more cycles could be achieved with the solvent; the overall economic feasibility of the separation process would be improved. The regeneration of CO₂-rich NOHMs can be performed either by pressure or temperature swings. A pressure swing process was selected to investigate the recyclability of NOHMs during CO₂ capture. First, NOHMs (i.e., NOHM-I-HPE and NOHM-C-HPE) were exposed to CO₂ at 25 °C and $P_{\text{CO}_2} = 0.34$ MPa. Once CO₂ absorption equilibrium was achieved, CO₂-rich NOHMs samples were regenerated under isothermal condition by applying vacuum ($P_{\text{CO}_2} = 0.00025$ MPa) for 20 minutes. The regenerated NOHMs samples were then re-introduced to the capture reactor for the next CO₂ capture cycle.

The CO₂ capture capacity of recycled NOHM-I-HPE remained at the same level as that of a fresh NOHM-I-HPE sample even after 10 cycles (Figure 6-9). Since there were no primary or secondary amines present in NOHM-I-HPE to chemically absorb CO₂, most of interactions between CO₂ and polymeric chain of NOHM-I-HPE were relatively weak (i.e., physisorption and Lewis acid-base interaction). Therefore, CO₂-rich NOHM-I-HPE was easily regenerated by pressure swing. However, in case of NOHM-C-HPE shown in Figure 6-10, there was a

considerable reduction in CO₂ capture capacity after the first cycle. This significant drop was attributed to the chemical bonding of CO₂ and the secondary amine in NOHM-C-HPE which could not be broken by the given pressure swing. Thus, a temperature swing method was employed to regenerate NOHM-C-HPE by purging in N₂ environment at 120 °C. Figure 5.11 shows that CO₂ capture capacity of NOHM-C-HPE was fully recovered without significant loss after 10 cycles.

6.3.6 Effects of Ether and Amine Groups on CO₂ Capture using NOHMs

The effect of functional groups was already briefly discussed in previous sections. Here, two functional groups, ether and amine groups were further investigated to quantify the enhancement of CO₂ capture via chemical interactions. First, NOHM-C-HPE and NOHM-C-MPE were prepared using polyetheramines that have comparable molecular weights but different amounts of ether groups. On average, NOHM-C-HPE contained 41 ether groups, and NOHM-C-MPE consists of 35 ether groups. As shown in Figure 6-11, there was a slight increase in CO₂ solubilities in NOHM-C-HPE compared to that in NOHM-C-MPE. This trend was more significant as the partial pressure CO₂ increased. Interestingly, the ratio between CO₂ capture capacities of NOHM-C-HPE and NOHM-C-MPE at $P_{\text{CO}_2} = 0.34$ MPa matched the ratio of the amount of ether groups in two NOHMs samples (i.e., 41/35).

In case of amine groups, the effect of functional groups on CO₂ capture was much stronger. In order to investigate this effect, two NOHMs samples were prepared: NOHM-I-PEI (polyethylenimine-nanoparticle hybrid) and NOHM-I-tPE (synthesized using polyetheramines with tertiary amine groups). CO₂ capture capacity of pure polyetheramines with tertiary amine groups was about 0.4 mmol-CO₂/g-solvent (at 25 °C and $P_{\text{CO}_2} = 0.32$ MPa) and about 2.5 mmol-

CO₂/g-solvent for pure polyethylenimine (at 75 °C and P_{CO₂} = 0.1 MPa) (Qi et al., 2011). As shown in Figure 6-12, the existence of amine groups (both primary and secondary amines) significantly increased the CO₂ capture capacity of NOHMs. Under the same capture conditions (at 30 °C and P_{CO₂} = 0.34 MPa), NOHM-I-tPE exhibited the CO₂ capture capacity of 0.25 mmol-CO₂/g-solvent, while NOHM-I-PEI achieved the CO₂ capture capacity of 1.0 mmol-CO₂/g-solvent after 2 hours. This was because the branched amine groups in NOHM-I-PEI were more readily available to interact with CO₂.

6.4 Conclusions

NOHMs in NOHM-I group exhibited lower CO₂ capture capacity than NOHMs in NOHM-C group because the amine groups of the polymers in NOHM-I group were protonated whereas secondary amines in NOHM-C group were available for the reaction with CO₂. It was also found that ether groups on corona chains of NOHMs enhanced CO₂ capture via Lewis acid-base interactions. The effect of functional groups on CO₂ capture was far more significant when amines were incorporated in NOHMs. NOHMs also exhibited a high selectivity towards CO₂ compared to N₂, O₂, and N₂O, and a promising recyclability. With these unique features, NOHMs have shown a great potential for CO₂ capture.

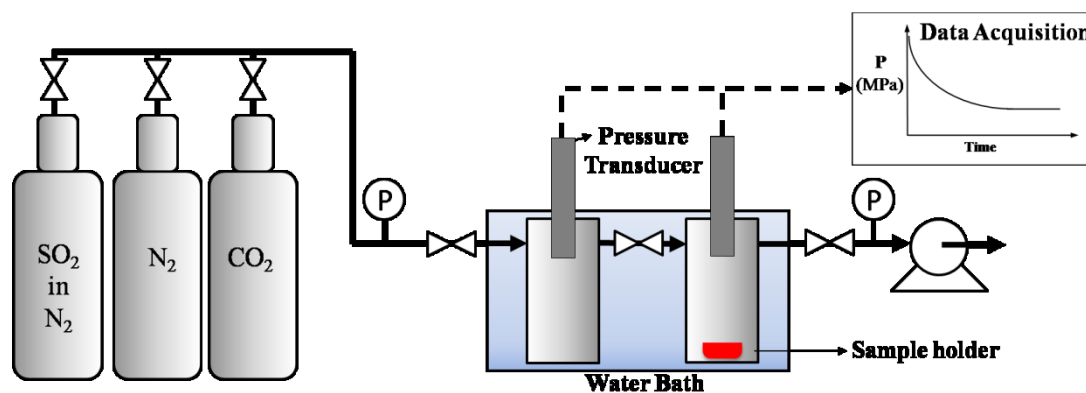
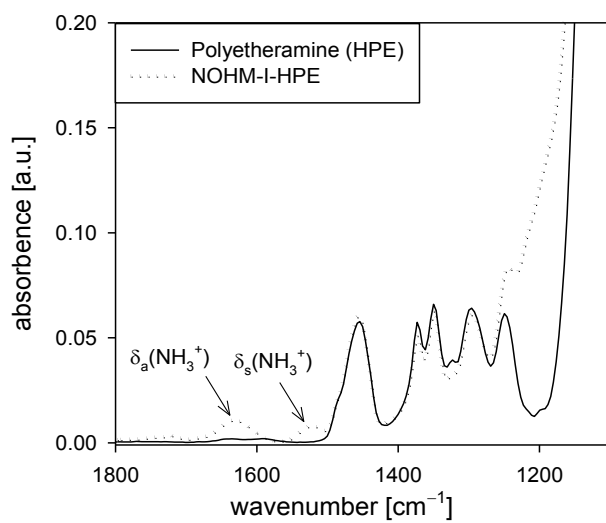


Figure 6-1 A Schematic diagram for a dual-chamber reactor for gas sorption with pressure range 0.1 -0.34 MPa and temperature range 25 – 80°C.

(a)



(b)

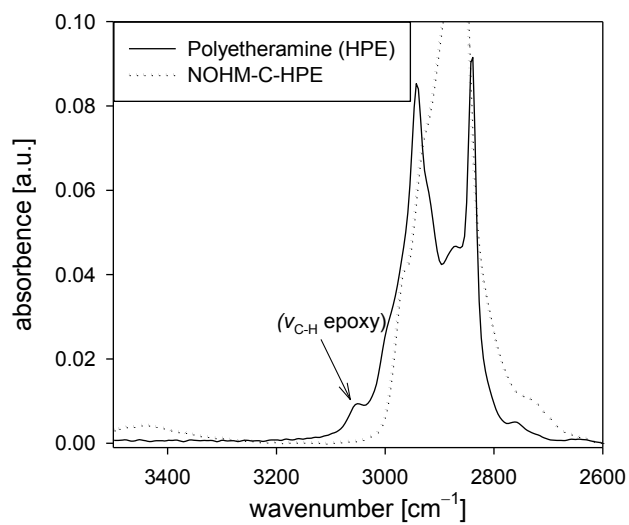


Figure 6-2 ATR FT-IR spectra of synthesized NOHMs (a) NOHM-I-HPE, (b) NOHM-C-HPE

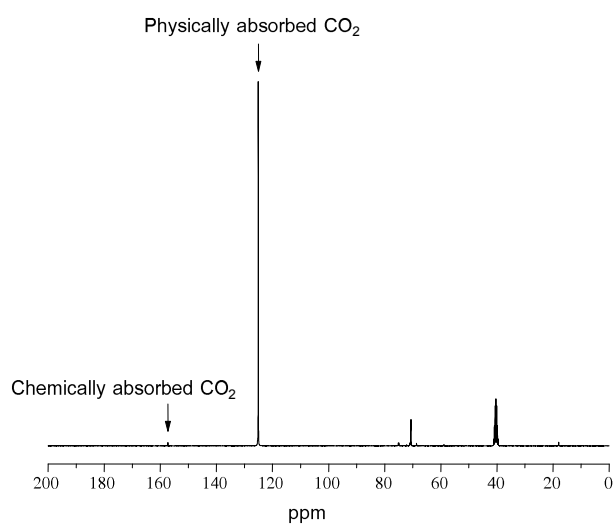


Figure 6-3 ^{13}C NMR of NOHM-I-HPE loaded with $^{13}\text{CO}_2$. (NOHM-I-HPE in DMSO-d_6 was placed in a high pressure NMR tube at $P^{13}\text{CO}_2 = 0.5 \text{ MPa}$)

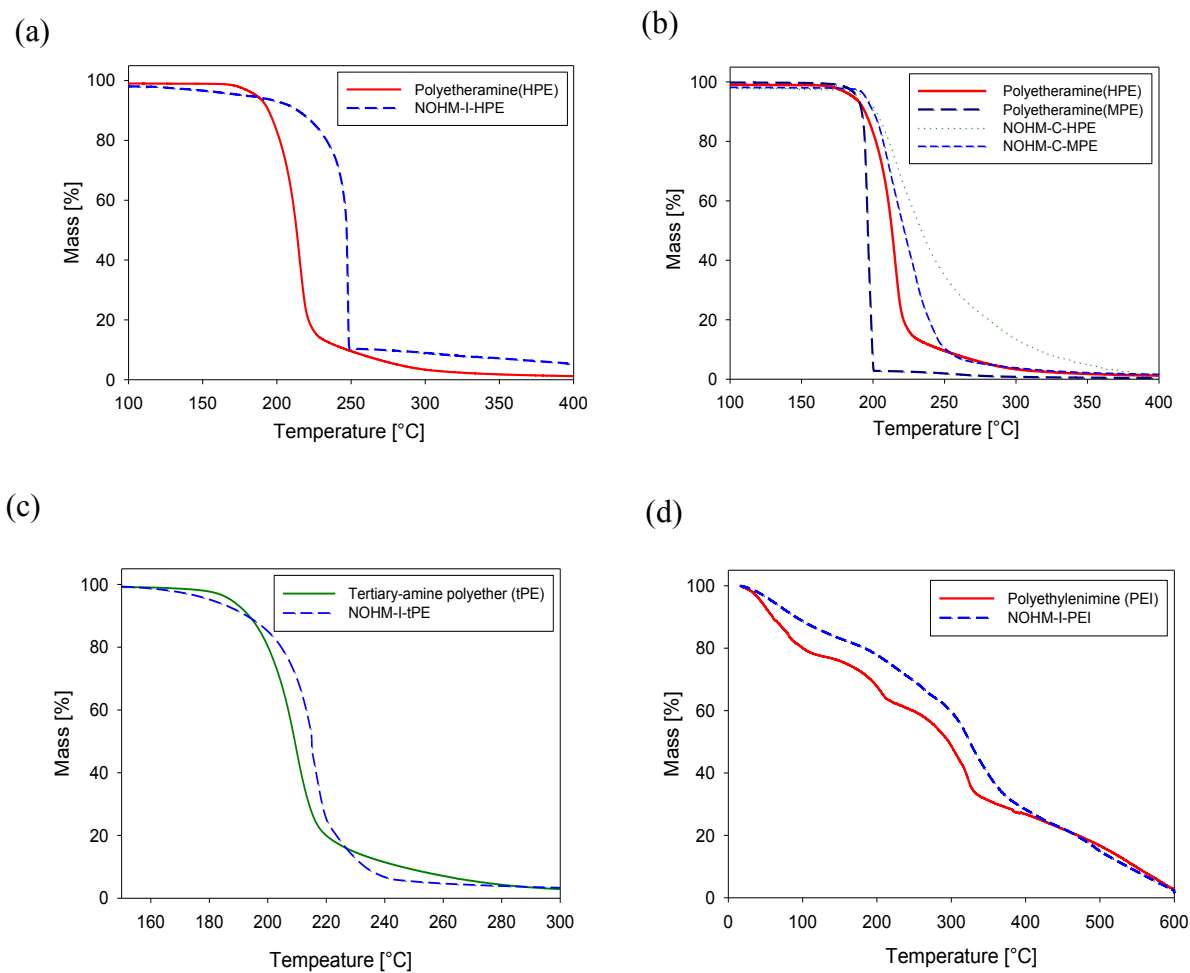


Figure 6-4 Thermal stabilities of NOHMs and their corresponding polymers determined by thermogravimetric analyses. (a) NOHM-I-HPE, (b) NOHM-C-HPE and NOHM-C-MPE, (c) NOHM-I-tPE and (d) NOHM-I-PEI. Mass (%) was calculated based on only the mass of the organic portion of NOHMs.

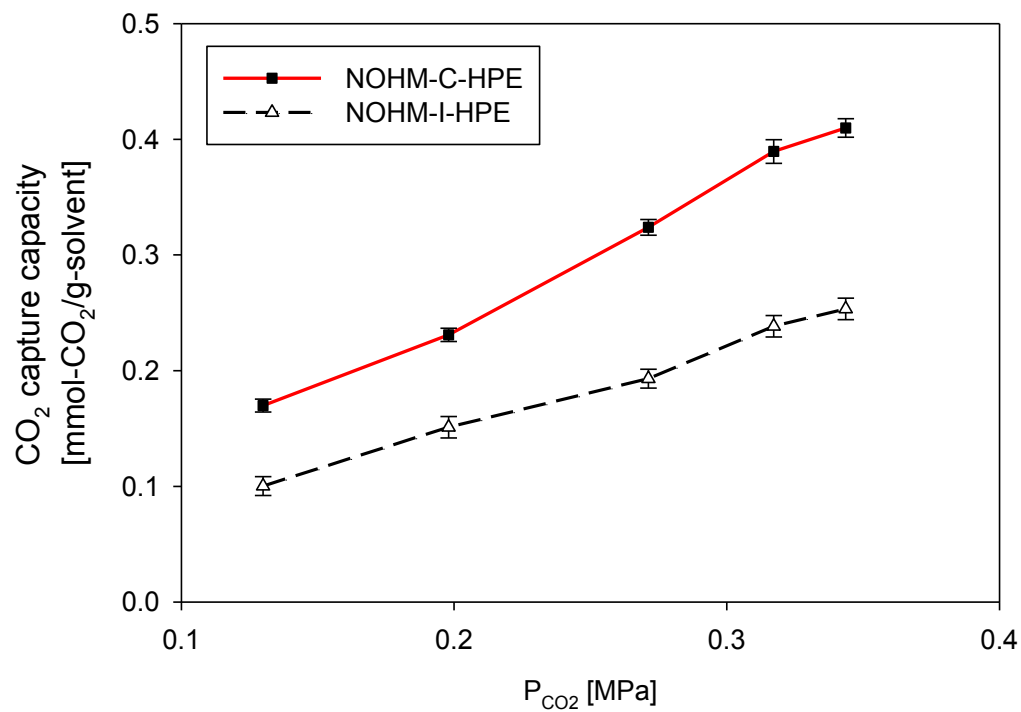


Figure 6-5 Effect of bonding types used in the synthesis of NOHMs on CO₂ capture capacity as a function of partial pressure of CO₂ at 25 °C

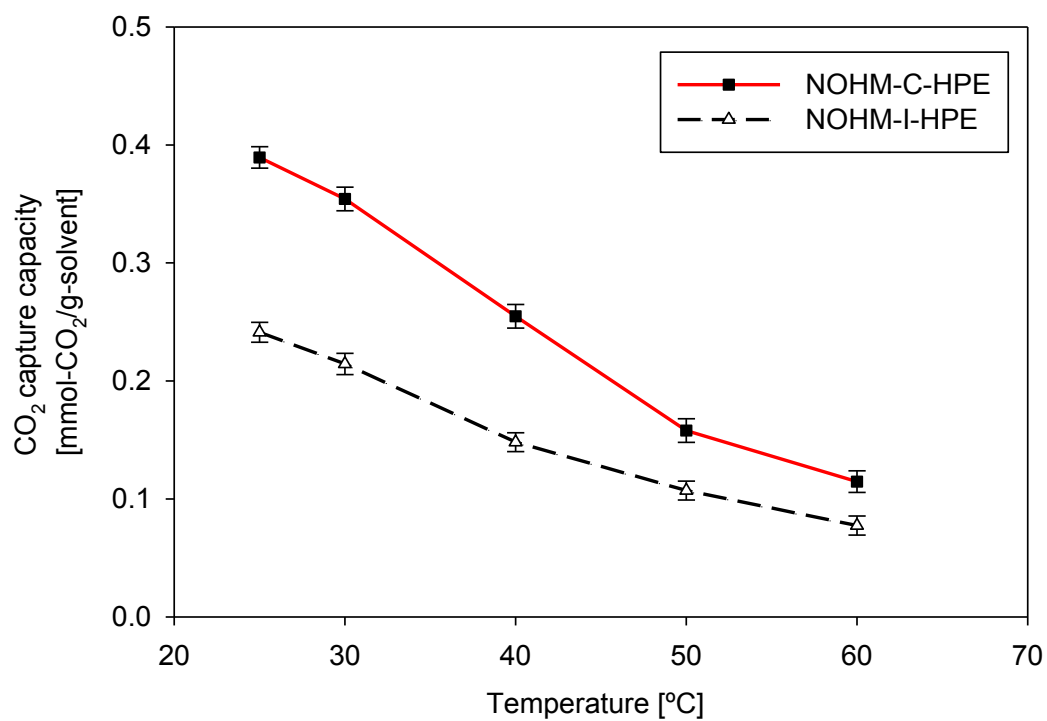


Figure 6-6 Effect of bonding types used in the synthesis of NOHMs on CO₂ capture capacity as a function of temperature at $P_{\text{CO}_2} = 0.32$ MPa.

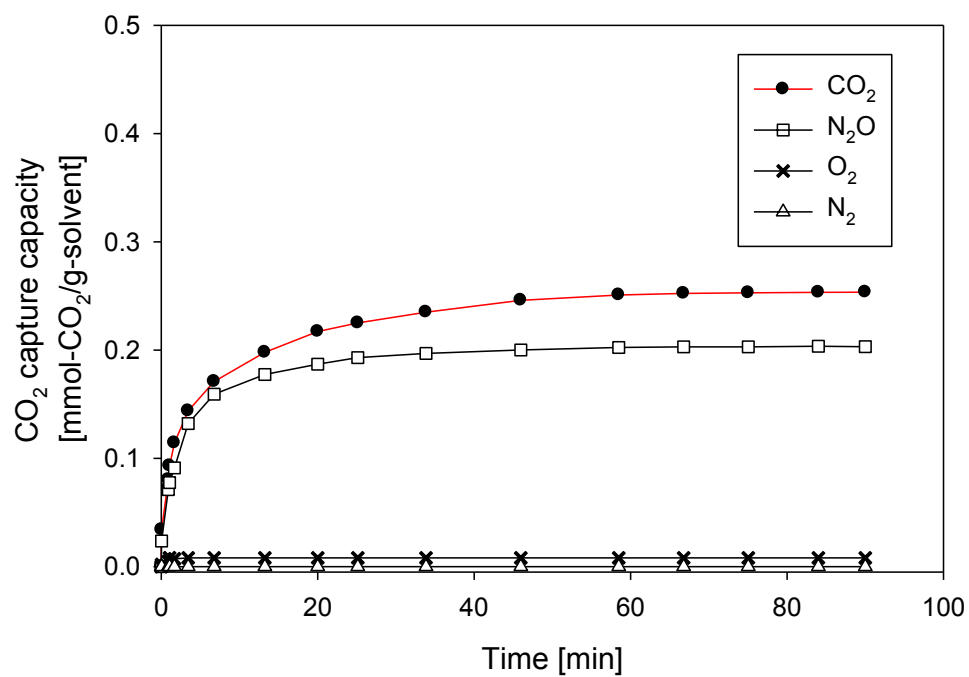


Figure 6-7 Sorption kinetics of CO₂ and other gases in NOHM-I-HPE ($T = 25\text{ }^{\circ}\text{C}$, $P_{\text{CO}_2} = 0.34\text{ MPa}$, $P_{\text{N}_2\text{O}} = 0.34\text{ MPa}$, $P_{\text{O}_2} = 0.34\text{ MPa}$ and $P_{\text{N}_2} = 0.34\text{ MPa}$).

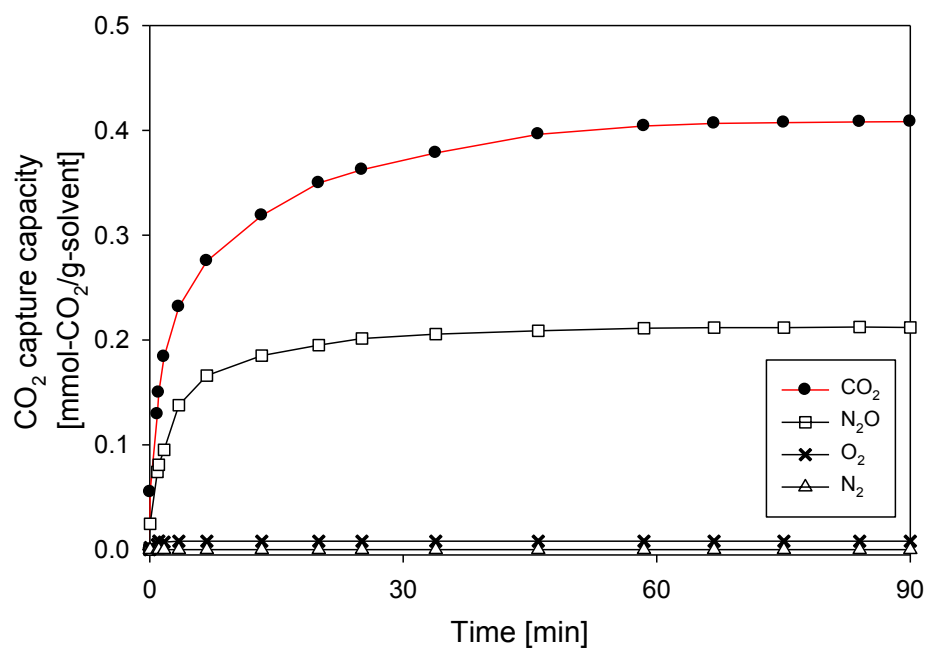


Figure 6-8 Sorption kinetics of CO₂ and other gases in NOHM-C-HPE ($T = 25\text{ }^{\circ}\text{C}$, $P_{\text{CO}_2} = 0.34\text{ MPa}$, $P_{\text{N}_2\text{O}} = 0.34\text{ MPa}$, $P_{\text{O}_2} = 0.34\text{ MPa}$ and $P_{\text{N}_2} = 0.34\text{ MPa}$)

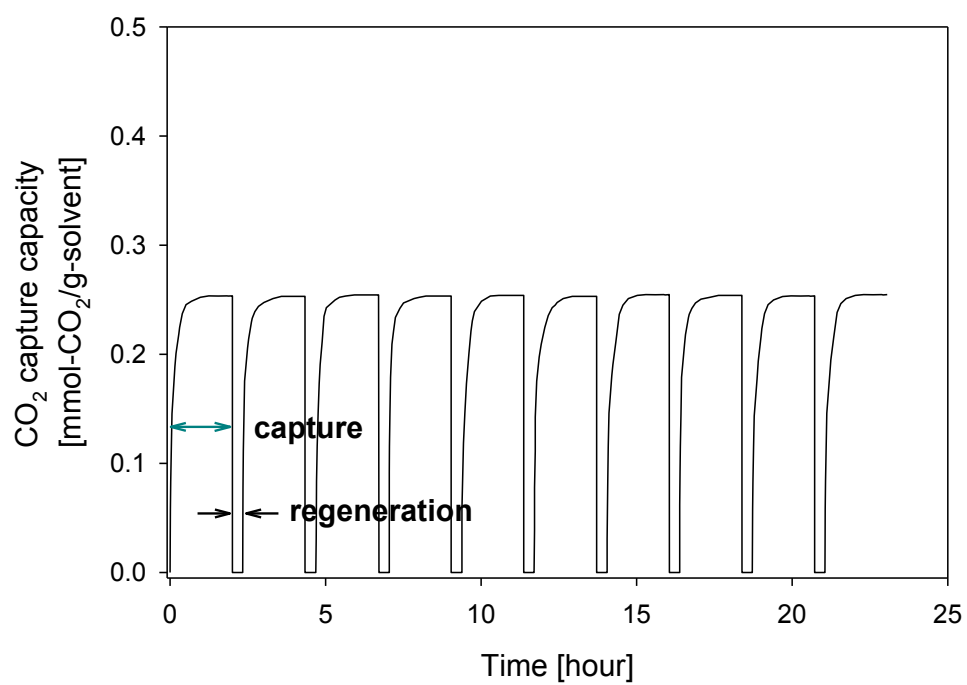


Figure 6-9 Multi-cycle CO₂ capture using NOHM-I-HPE (Capture conditions: T = 25 °C and P_{CO2} = 0.34 MPa; Regeneration conditions: T = 25 °C and P_{vacuum} = 0.00025 MPa).

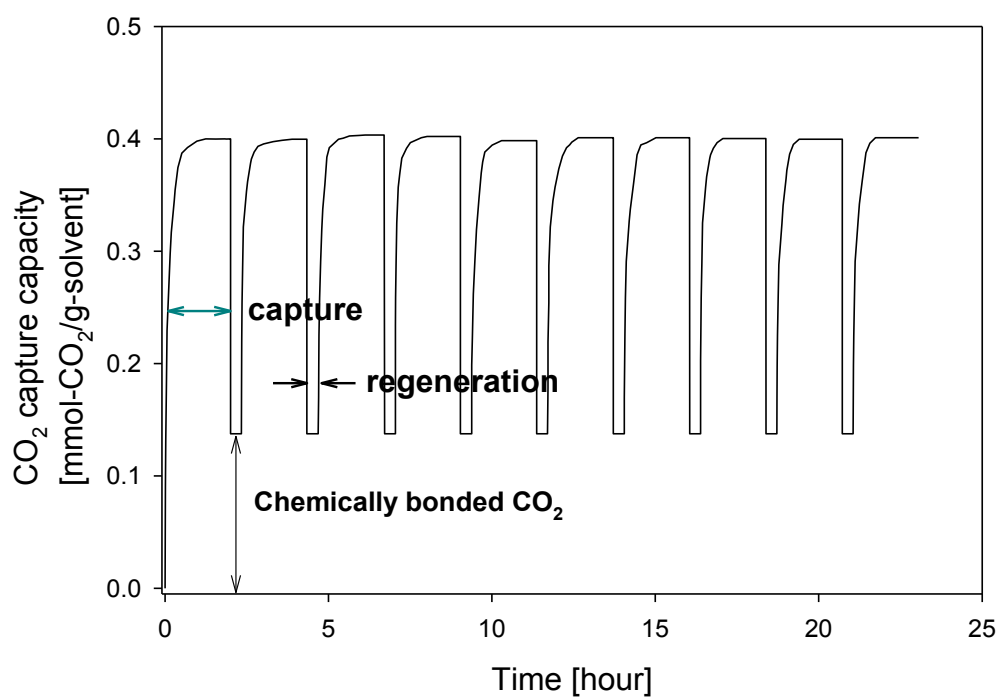


Figure 6-10 Multi-cycle CO₂ capture using NOHM-C-HPE (Capture conditions: T = 25 °C and P_{CO₂} = 0.34 MPa; Regeneration conditions: T = 25 °C and P_{vacuum} = 0.00025 MPa).

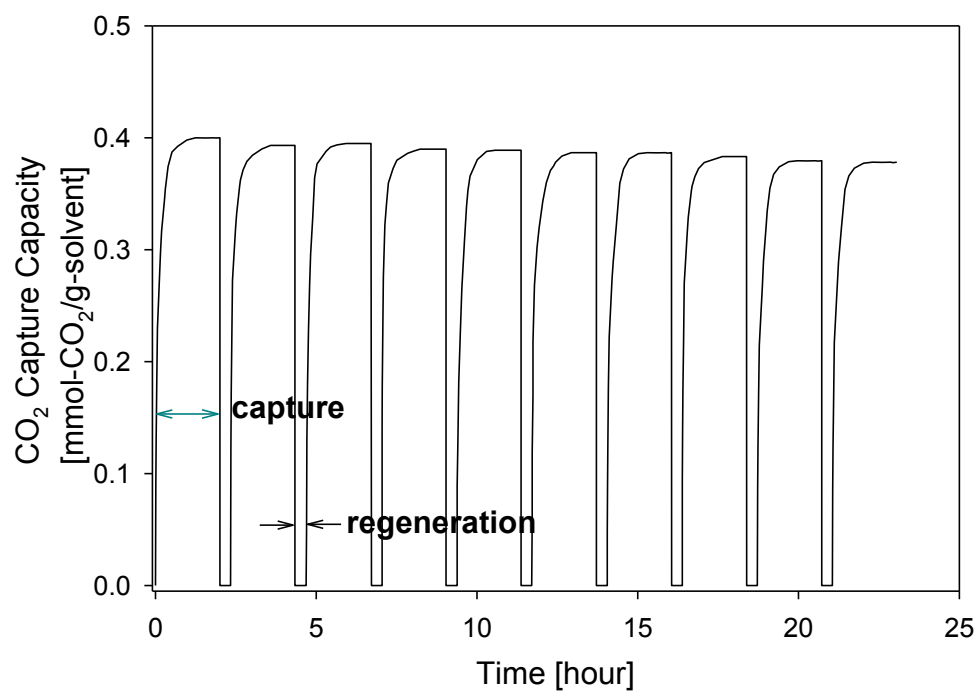


Figure 6-11 Multi-cycle CO₂ capture using NOHM-C-HPE (Capture conditions: T = 25 °C and P_{CO2} = 0.34 MPa; Regeneration conditions: T = 120 °C with N₂ purge).

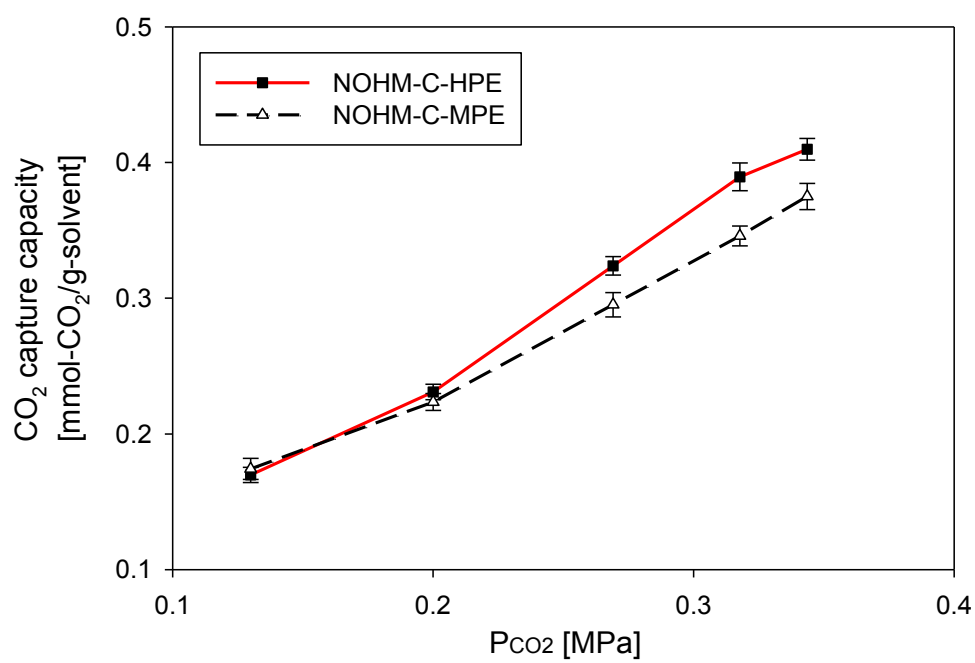


Figure 6-12 Effect of ether groups on CO₂ capture capacity of NOHMs at 25 °C

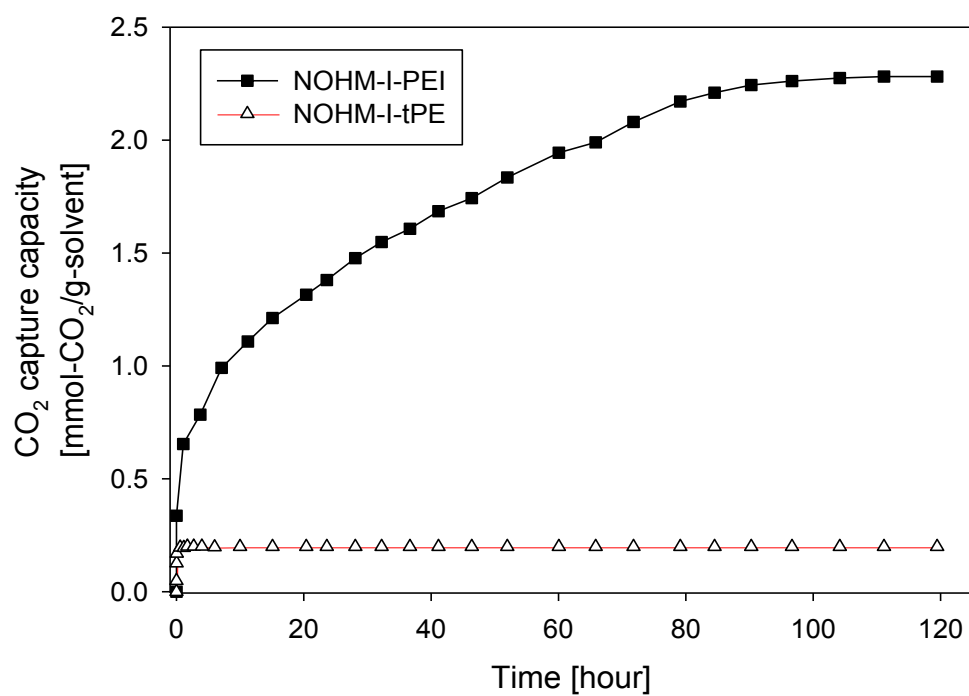


Figure 6-13 Effect of amine groups on CO₂ capture capacity of NOHMs ($P_{\text{CO}_2} = 0.34$ MPa and $T = 30$ °C)

Reference

- Bourlinos, A. B., Chowdhury, S. R., Herrera, R., Chalkias, N., Jiang, D. D., Zhang, Q., Archer, L. A., Giannelis, E. P. "Functionalized Nanostructures with Liquid-Like Behavior: Expanding the Gallery of Available Nanostructures" *Adv. Funct. Mater.* 15(8), 1285-1290, 2005.
- Bourlinos, A. B., Herrera, R., Chalkias, N., Jiang, D. D., Zhang, Q., Archer, L. A., Giannelis, E. P. "Surface-Functionalized Nanoparticles with Liquid-Like Behavior" *Adv. Mater.* 17, 234-237, 2005.
- Ghosal, K., R. T. Chen, et al. "Effects of basic substituents on gas sorption and permeation in polysulfone." *Macromolecules*, 29(12), 4360-4369, 1996.
- Lin, H. and B. D. Freeman "Gas solubility, diffusivity and permeability in poly(ethylene oxide)." *Journal of Membrane Science*, 239(1), 105-117, 2004.
- Lin, H. and B. D. Freeman "Gas and Vapor Solubility in Cross-Linked Poly(ethylene Glycol Diacrylate)" *Macromolecules*, 38(20), 8394-8407, 2005.
- Meeks, N. D., S. Rankin, et al., "Sulfur-Functionalization of Porous Silica Particles and Application to Mercury Vapor Sorption" *Industrial & Engineering Chemistry Research*, 49(10), 4687-4693, 2010.
- Qi, G., Y. Wang, et al., "High efficiency nanocomposite sorbents for CO₂ capture based on amine-functionalized mesoporous capsules" *Energy & Environmental Science* 4(2), 444-452, 2011.
- Rodriguez, R., Herrera, R., Archer, L. A., Giannelis, E. P. "Nanoscale Ionic Materials." *Adv. Mater.* 20, 4353-4358, 2008.

CHAPTER 7

EFFECT OF SO₂ ON CO₂ CAPTURE USING NOHMs

This chapter is based on the following manuscript in preparation:

K.-Y. A. Lin, C. Petit, and A.-H. A. Park "Effect of Sulfur Dioxide on Carbon Dioxide Capture using Liquid-like Nanoparticle Organic Hybrid Materials", 2012.

7.1 Introduction

Since NOHMs is proposed to be an alternative solvent for capturing CO₂ from the post combustion, a few aspects should be addressed to facilitate the implementation of this technology into a large scale. One of these aspects is the impact of sulfur dioxide (SO₂) in the flue gas stream from the post combustion. Generally, typical concentration of SO₂ of the flue gas stream from oil burners / boilers is about 180 – 220 ppm and 2000 ppm from burning poor quality coal. Although the concentration of SO₂ is low, it is important to investigate the effect of SO₂, a strong acidic gas, on CO₂ capture using NOHMs. In this chapter, the SO₂ capture capacity of NOHMs and the effect of SO₂ on CO₂ capture capacity were investigated. Beside CO₂ capture capacity, it is also necessary to explore the effect of SO₂ on CO₂-induced swelling in NOHMs. By measuring CO₂-induced swelling and packing behaviors using an ATR FT-IR, the effect of SO₂ on CO₂ sorption in NOHM can be observed at a molecular level. By bringing a better understanding of the effect of SO₂ on CO₂ capture using NOHMs, this chapter provides important information in order to facilitate the implementation of this technology.

7.2 Experimental

7.2.1 Preparation of NOHMs

Two NOHMs were synthesized for this study: NOHM-I-HPE and NOHM-C-HPE (Figure 7-1). NOHM-I-HPE was prepared via attaching a polyetheramine (Jeffamine M-2070 or HPE) to the functionalized nanoparticle by ionic bonding. The details of preparation can be found in previous literature. (Rodriguez 2008; Lin and Park 2011) NOHM-C-HPE was prepared by reacting HPE with a glycidyl ether silane via covalent bonding. 3 wt% of HPE in ethanol was prepared and a molar equivalence of (3-glycidyloxypropyl) trimethoxysilane was added to each solution. After

stirring for 12 hours at 45 °C, the silica suspension was added into the polyether-silane solution. The resulting mixture was stirred for 5 hours and dialyzed (MWCO 3.5k) against deionized water for 48 hours to remove excess polyether-silane. To obtain the final NOHMs products, solvents were removed under vacuum at 35 °C to yield liquid-like materials. The difference between NOHM-I-HPE and NOHM-C-HPE is that the primary amine in NOHM-I-HPE is in ionic bonding and not available for reacting with CO₂. As for NOHM-C-HPE, the primary amine is simply converted to a secondary amine which is then available to react with CO₂ chemically.

7.2.2 Characterization

Synthesized NOHMs samples were analyzed using the FT-IR spectroscopy to verify the reaction between the primary amines and the surface functional groups of the nanoparticle cores (i.e., ionic bonding with the sulfonate group for NOHM-I-HPE and covalent bonding with the glycidyl ether group for NOHM-C-HPE).

7.2.3 CO₂ Capture using NOHMs

A high pressure dual-chamber reactor was constructed with temperature control (shown in Figure 6-1) to measure capture capacity of various gases in NOHMs. The internal volume of each reactor was 15 ml and a sample holder was designed to hold about 0.15 g of a thin layer of a NOHMs sample. Each reactor was mounted with a high-accuracy pressure transducer. The loaded sample holder was placed into the second chamber. Before each sorption measurement, any air or gas in the loaded reactor was removed by applying vacuum. The pressure was monitored and recorded by the pressure transducers and a data acquisition system. A selected gas (N₂, pre-humidified N₂, SO₂ in N₂, and CO₂) was introduced into the first chamber at a desired

pressure and then valve between two chambers was opened to introduce the gas into the second chamber. Once the gas sorption reached equilibrium, capture capacity was calculated based on the pressure decay using the ideal gas law. N_2 , SO_2 in N_2 (200 ppm and 3010 ppm) and CO_2 were all ultra pure grade and certified gases. Pre-humidified N_2 was prepared by flowing N_2 through a bubble column for a relative humidity of 80% at 25 °C.

7.2.4 Breakthrough experiments of CO_2 and SO_2

A packed bed loaded with 250 μm (dia.) glass beads was used to measure the breakthrough curves of CO_2 and SO_2 . 2 g of NOHM-I-HPE was coated onto 28 g of glass beads and then packed in a quartz column. Since NOHM-I-HPE is slightly viscous, a thin layer of NOHM-I-HPE can cover the glass beads without any issues. Concentrations of CO_2 and SO_2 were introduced at 14% and 200 ppm with a total flow rate of 12.5 ml/min. The outlet of the gas stream was connected to a gas emission detector (Enerac Inc.) equipped with NDIR and SEM electrochemical sensors. The concentration was monitored by a computer with data acquisition software.

7.2.5 Attenuated Total Reflectance (ATR) FT-IR Spectroscopy

ATR FT-IR spectra of the synthesized materials were obtained using a Nicolet 6700 spectrometer (Thermo Fisher Scientific Inc.) equipped with an ATR cell consisting of a high-pressure cell (Golden GateTM Supercritical Fluids Analyzer, Specac Ltd). FTIR spectra were collected 16 times with a resolution of 4 cm^{-1} for the characterization of synthesized NOHMs. FT-IR spectroscopy was also used to determine the CO_2 capture capacity, CO_2 -induced swelling and packing behaviors of NOHMs under various pressures (from 0.13 to 0.68 MPa of pure CO_2

or CO₂/SO₂ mixture) at 25 °C. The details of using the ATR FT-IR for calculation of CO₂ capture capacity, CO₂-induced swelling and packing behaviors can be found in Section 5.2.2 and 5.3.4. For investigating the effect of SO₂ on CO₂ capture capacity, CO₂-induced swelling and packing behaviors, a mixture of CO₂/SO₂ (2000 ppm SO₂ in CO₂) was used to pressurize NOHMs at 0.1 MPa

7.3 Results and Discussion

7.3.1 Characterization of Synthesized NOHMs

Synthesized NOHM-I-HPE and NOHM-C-HPE were characterized by the FT-IR spectroscopy to verify the attachment of polymers onto the surface-functionalized nanoparticles, as shown in Figure 6-2. In case of NOHM-I-HPE, the attachment involved a reaction between the primary amines of HPE and the sulfonate group of the surface-functionalized nanoparticle. The resulting ionic bonding contained NH₃⁺ which was observed at 1530 cm⁻¹ ($\delta_s(\text{NH}_3^+)$) and at 1630 cm⁻¹ ($\delta_a(\text{NH}_3^+)$). In case of NOHM-C-HPE, the attachment involved a reaction between the primary of HPE and the glycidyl ether group. The formation of the polyether-silane was confirmed by the disappearance of a band at 3056 cm⁻¹ (ν_{C-H} epoxy) and the presence of the hydroxyl group at 3400~3600 cm⁻¹ (Lin and Park 2011).

7.3.2 Sorption of N₂, Pre-humidified N₂, SO₂ and CO₂ in NOHMs

After characterization, NOHMs samples were tested for the SO₂ capture capacity. In general, the concentration of SO₂ of the flue gas stream is about 180 – 220 ppm depending on the type and source of fossil fuels, and the balance of the flue gas stream predominantly is nitrogen (N₂). Before testing NOHMs with a N₂/SO₂ mixture, NOHMs was placed in pure N₂ environment to

determine the level of N_2 sorption in NOHMs. Figure 7-2 shows the sorption kinetic of N_2 in NOHM-I-HPE with almost no N_2 being captured by NOHM-I-HPE over time. Since N_2 is not soluble in NOHMs, 200 ppm SO_2 in N_2 was then introduced to the dual chamber reactor to measure sorption of SO_2 in NOHMs. The sorption of 200 ppm SO_2 in NOHMs is also shown in Figure 7-2. The amount of SO_2 captured in NOHMs was insignificant. When the concentration of SO_2 was increased to 3010 ppm, a significant amount of SO_2 was captured in NOHM-I-HPE. This suggests that NOHMs is capable of capturing SO_2 and is pronouncedly selective toward SO_2 over N_2 . Figure 7-2 also shows the sorption kinetic of pre-humidified N_2 in NOHMs. Although pure N_2 is not soluble in NOHM-I-HPE, a certain level of pre-humidified N_2 was captured in NOHM-I-HPE. This indicates that NOHMs was also capable of capturing water vapor which is also a component of a typical flue gas stream.

7.3.3 Effect of SO_2 Exposure on CO_2 Capture Capacity of NOHMs

NOHM-I-HPE consists of the primary amine and the sulfonate group. Exposure to SO_2 may result in the dissociation of ionic bonding because SO_2 may compete with the sulfonate group to react with the primary amine of the polyetheramine. If SO_2 replaces the sulfonate group, the polymer will be no longer attached to the nanoparticle. Random polymer chains have demonstrated different entropic effects from the tethered polymer chains in NOHMs on CO_2 capture (Park et al., 2011).

NOHM-I-HPE and NOHM-C-HPE were first exposed to 3010 ppm SO_2 in N_2 ($P = 0.1$ MPa) until the gas sorption equilibrium was reached. CO_2 ($P_{CO_2} = 0.2$ MPa) was then introduced to the reactor chamber to perform CO_2 capture. Figure 7-3 shows CO_2 capture capacity of NOHM-I-HPE with and without prior exposure to SO_2 . The CO_2 capture capacity of a SO_2 -exposed

NOHM-I-HPE was notably lower (about 10%) than the capture capacity of pristine NOHM-I-HPE. This decrease in capture capacity of the SO₂-exposed NOHM-I-HPE may be caused by fewer capture sites within NOHMs that are occupied by SO₂. Another possible explanation for the decrease may be due to the dissociation of the polymer. A less-ordered canopy from the dissociation of NOHMs eliminates some orderly pathways to facilitate CO₂ capture. Since tethered polymer chains of NOHMs can exhibit distinct thermal stability (enhanced thermal stability) in comparison with detached or unbound polymer chains, a thermogravimetric analysis (TGA) was conducted to verify this possibility. TGA was used to measure the weight change of NOHM-I-HPE after the SO₂ exposure as a function of temperature. Derivative weight change of NOHM-I-HPE (Figure 7-4) showed no noticeable variation in the thermal stability of NOHM-I-HPE after SO₂ exposure and CO₂ exposure. It was known that as NOHM-I-HPE exposed to CO₂, the dissociation of polymer chains is not expected (Lin and Park 2011). The comparison in Figure 7-4 suggests that no dissociation of NOHMs' canopy caused by the SO₂ exposure has occurred. Another approach for investigating whether the canopy dissociates is to probe the conformational order of NOHM-I-HPE. If the canopy dissociates due to the SO₂ exposure, the SO₂-exposed NOHMs may exhibit less conformational order than a pristine NOHM-I-HPE. In order to measure the conformational order, a Raman Spectroscopic technique was employed.

As mentioned in Section 5.3.2, Raman spectroscopy has been proposed to determine the conformational order of linear molecules (Larsson and Rand 1973; Orendorff et al., 2002). In the analysis of Raman spectra of polymers, some indicators can be used to correlate to the conformational change of linear molecules under various conditions and manipulations. Since the CH₂ group is the backbone unit of HPE, the intensity ratio of the $\nu_a(\text{CH}_2)$ band (asymmetric stretching mode, $\sim 2850\text{ cm}^{-1}$) to the $\nu_s(\text{CH}_2)$ band (symmetric stretching mode, $\sim 2885\text{ cm}^{-1}$) has

been proposed as an indicator to investigate the conformational order^(Orendorff et al., 2002) (shown in Figure 7-5). The ratio of $I[\nu_a(\text{CH}_2)]$ to $I[\nu_s(\text{CH}_2)]$ of NOHM-I-HPE after the SO_2 exposure (the ratio = 0.81) was compared with the ratio of a pristine NOHM-I-HPE (the ratio = 0.80). The comparison indicates that there is no significant difference between these two cases, and the dissociation of NOHM-I-HPE due to SO_2 was not observed. In case of NOHM-C-HPE, CO_2 capture capacity significantly decreased (about 30%) when NOHM-C-HPE exposed was to SO_2 first. Since NOHM-C-HPE was synthesized via covalent bonding, the dissociation of polymer from the surface-functionalized nanoparticle was not expected. Therefore, the loss in capture capacity in NOHM-C-HPE after the SO_2 exposure was attributed to the unavailability of secondary amine in pristine NOHM-C-HPE, which had reacted with SO_2 .

As NOHMs being developed as an alternative solvent for the post-combustion CO_2 capture, NOHMs was tested to remove CO_2 from a gas mixture stream which mimics the concentrations of N_2 , CO_2 and SO_2 in the flue gas stream. A mixture of 14 % CO_2 and 200 ppm of SO_2 in N_2 was prepared and introduced to a packed bed loaded with NOHM-I-HPE. After introduction of the mixture gas, CO_2 and SO_2 breakthrough curves were generated (Figure 7-6). The breakthrough of CO_2 occurred after about 400 seconds while the breakthrough of SO_2 occurred after about 500 seconds. This indicates that CO_2 and SO_2 can be removed simultaneously.

Although the concentration of SO_2 is merely 200 ppm, the breakthrough time for SO_2 was not less than that of CO_2 , suggesting that there is no significant preference towards SO_2 in NOHMs over CO_2 . With the same packed bed loaded with NOHM-I-HPE, a gas mixture of N_2 and CO_2 was also introduced. The breakthrough of CO_2 of the N_2/CO_2 stream was comparable to the breakthrough of CO_2 from the $\text{N}_2/\text{CO}_2/\text{SO}_2$ stream. This indicates that the presence of SO_2 did not considerably affect the CO_2 capture capacity in NOHM-I-HPE at the given concentration of

SO₂. The functional sites occupied by SO₂ could significantly be increased as the number of CO₂ capture cycles increases. Furthermore, the level of deactivation would be a function of SO₂ concentration in flue gas. Since SO₂ would strongly bind to NOHMs' functional groups such as amines compared to CO₂, SO₂-bound NOHMs should be regenerated at higher temperatures (e.g., 140 °C) (Huang et al., 2006) to regain the full CO₂ capture capacity of NOHMs. Another approach to maintain the CO₂ capture capacity of NOHMs during long term capture and regeneration cycles is to purge a small portion of SO₂-rich NOHMs and charge the system with fresh NOHMs after each capture cycle.

7.3.4 Effect of SO₂ on CO₂-induced Swelling and Packing Behaviors

The molecular observation of the effect of SO₂ on CO₂ sorption in NOHMs was also conducted by using ATR FT-IR. Per typical behavior of liquid-like materials, sorption of CO₂ in NOHMs can result in a volume change. Such a volume change is attributed to CO₂ bound to the polymer chain and enclosed between polymer chains. Therefore, CO₂ sorption and CO₂-induced swelling can provide information on how gas molecules respond to the configuration of polymer chains with NOHMs. In order to investigate the effect of SO₂ on CO₂-induced swelling behavior, NOHMs were pressurized with a mix of CO₂/SO₂ and the results were compared to those for the CO₂-induced swelling behaviors under pure CO₂ environment.

As shown in Figure 7-7(a), a higher degree of swelling is observed as CO₂ capture capacity is increased in NOHM-I-HPE pressurized with pure CO₂. The relationship between CO₂ capture capacity and swelling percentage is almost linear, suggesting that a certain amount of CO₂ occupies a specific volume with NOHMs. While NOHM-I-HPE was pressurized by the CO₂/SO₂ mixture, the swelling behavior was comparable with the swelling behavior of NOHM-I-HPE

under pure CO₂ at relatively low pressure. However, the swelling behaviors of the two cases deviated at relatively high pressures. NOHM-I-HPE swelled less under pressurization of CO₂/SO₂ than pure CO₂. The same trend was observed in the case of NOHM-C-HPE (Figure 7-7(b)). This suggests that the presence of SO₂ can affect how CO₂ is bound to polymer chain and encapsulated between polymer chains. To verify this speculation, the ATR FT-IR was again employed to investigate how CO₂ is packed within NOHMs. Since the interaction between CO₂ and ether groups of NOHMs was revealed as a Lewis acid-base interaction (Park et al., 2011). As CO₂ is captured in NOHMs, a bending mode of CO₂ (ν_2 CO₂) in the range of 630 – 680 cm⁻¹ can be observed. ν_2 CO₂ can further be deconvoluted to an in-plane bending mode and an out-plane bending mode CO₂. (Figure 7-8)

The area ratio between the in-plane bending mode of CO₂ ($\nu_{2 \text{ in-plane}}$ CO₂) and the out-plane bending mode of CO₂ ($\nu_{2 \text{ out-plane}}$ CO₂) can be associated with the packing pattern of CO₂ within NOHMs. (Park et al., 2011) The area ratio of $\nu_{2 \text{ in-plane}}$ CO₂ to $\nu_{2 \text{ out-plane}}$ CO₂ of NOHM-I-HPE and NOHM-C-HPE at various pressures of CO₂ and CO₂/SO₂ were plotted and shown in Figure 7-9. The area ratios in both cases increased from 2.0 to 3.0 as the P_{CO2} changed from 0.13 to 0.68 MPa. Recently, Petit et al. reported the area ratios of $\nu_{2 \text{ in-plane}}$ CO₂ to $\nu_{2 \text{ out-plane}}$ in NOHMs under a pure CO₂ condition with relatively high pressures, ranging from 0.7 to 5.5 MPa. At P_{CO2} = 0.7, the area ratio was reported to be about 3.0. This value is comparable to the area ratio seen in Figure 7-9 at a similar P_{CO2} (0.68 MPa). *ab initio* calculations revealed that the absorbance of in-plane mode of CO₂ is 3 times higher than the absorbance of out-of-plane mode for phosphorous containing compounds with similar Lewis acid-based interactions with CO₂ (YoonKook 2005). In Figure 7-9, as P_{CO2} was below 0.68MPa, the area ratio was decreased. Since the magnitude of the area ratio can be affected by the CO₂ pressure (Petit et al., 2011), the decrease in the area

ratio could be the effect of pressure. Another possibility leading to this decrease may be a decrease in the interaction of Lewis acid base with CO₂ and ether groups at the relatively low pressures.

The change in the area ratio suggests that CO₂ is packed differently as the pressure increases. It was reported that the CO₂ packing patterns could be altered if the entropy of the polymeric canopy of NOHMs was changed. The configurational change may improve accessibility of the capture sites such as ether groups in NOHMs (Park et al., 2011). Once NOHMs were pressurized with CO₂/SO₂, area ratios of $\nu_{2 \text{ in-plane CO}_2}$ to $\nu_{2 \text{ out-plane CO}_2}$ were also plotted in Figure 7-9 to compare with the area ratios in case of pressurization by pure CO₂. The comparison shows that the area ratio of $\nu_{2 \text{ in-plane CO}_2}$ to $\nu_{2 \text{ out-plane CO}_2}$ in NOHM-I-HPE was noticeably higher than the area ratio in the case of pressurization by pure CO₂. The same trend was observed in NOHM-C-HPE.

7.4 Conclusions

While no significant amount of SO₂ was captured by NOHMs at low SO₂ concentration (200 ppm in N₂), a considerable amount of SO₂ was captured at 3010 ppm SO₂ in N₂. As N₂ is almost insoluble in NOHMs, NOHMs showed a high selectivity toward SO₂ capture over N₂ capture. This behavior can enable NOHMs to be a potential candidate for removal of SO₂. For the effect of SO₂ on CO₂ capture capacity, NOHMs were exposed to SO₂ first, and then used for CO₂ capture. About 10% of CO₂ capture capacity was reduced after NOHM-I-HPE's exposure to SO₂. NOHM-C-HPE meanwhile demonstrated about 30% of CO₂ capture capacity reduction after the exposure to SO₂. The pronounced loss in NOHM-C-HPE may be owing to the absence of the secondary amines in NOHM-C-HPE, which were reacted with SO₂. The result of the

simultaneous removal of CO_2 and SO_2 showed that when at low SO_2 concentration, NOHMs did not exhibit a noticeable selectivity toward SO_2 over CO_2 . CO_2 capture capacity and CO_2 -induced swelling was also measured with a mixture of CO_2/SO_2 to investigate the effect of SO_2 on how CO_2 is captured within NOHMs. While the comparable swelling behaviors were observed in both cases of pressurization with CO_2/SO_2 and pure CO_2 at low pressures, the swelling behaviors of the two cases started to deviate from each other at higher pressure. This may be attributed to the distinct packing patterns in NOHMs between the pressurization with CO_2/SO_2 and pure CO_2 . NOHMs tested in this study were not task-specific functionalized NOHMs; thus, the existence of SO_2 did significantly affect CO_2 capture capacity of NOHMs, especially since the concentration of SO_2 in the flue gas stream is relatively low. However, once NOHMs are fully loaded with amines, the effect of SO_2 may become pronounced. This should be investigated further in the future.

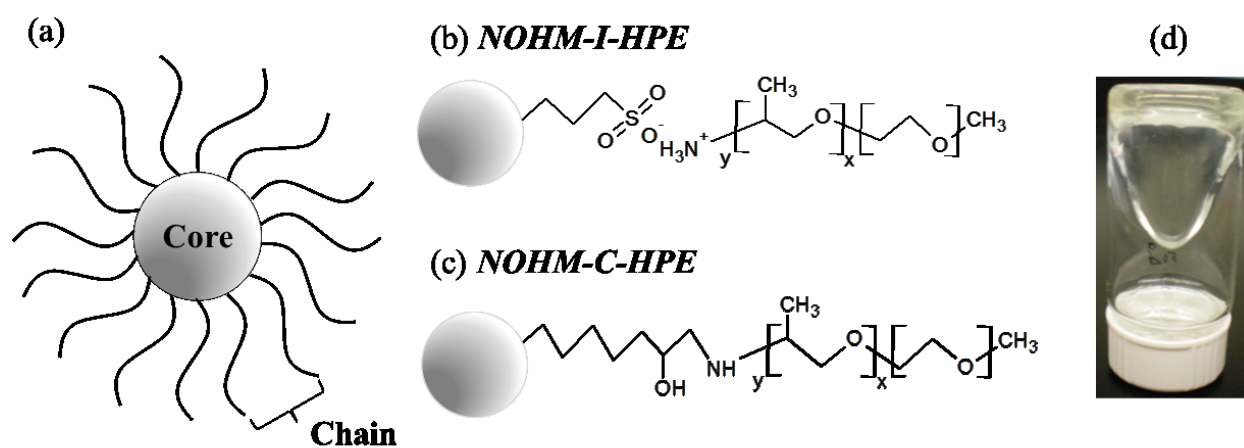


Figure 7-1 NOHMs' (a) configuration and two NOHMs examples: (b) NOHM-I-HPE, (c) NOHM-C-HPE and (d) NOHM-C-HPE photo.

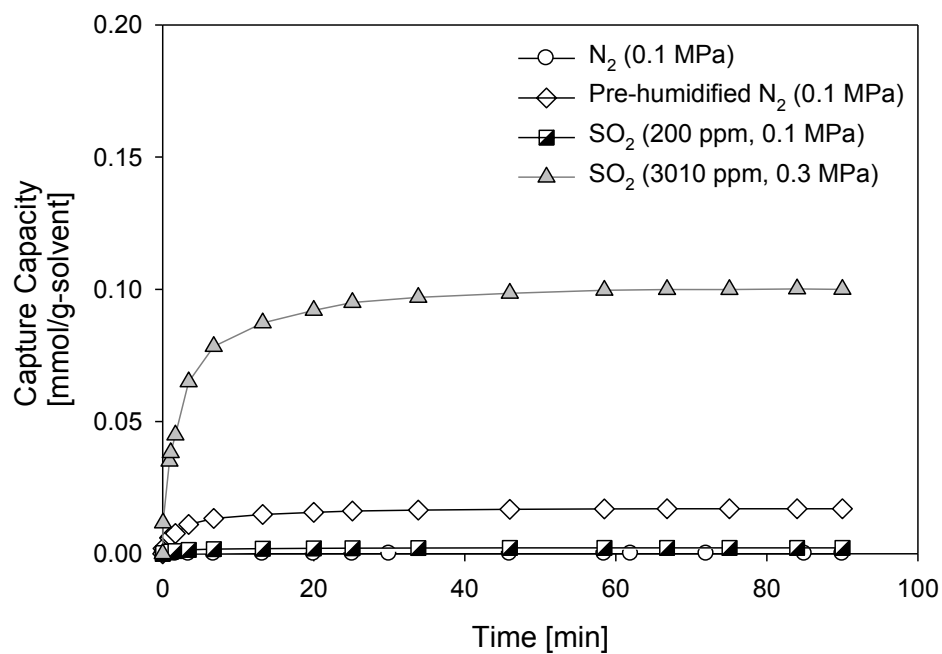


Figure 7-2 Absorption of N_2 ($P = 0.1$ MPa), pre-humidified N_2 ($P = 0.1$ MPa), 200 ppm SO_2 in N_2 ($P = 0.1$ MPa) and 3000 ppm SO_2 in N_2 ($P = 0.3$ MPa) in NOHM-I-HPE at 25 °C.

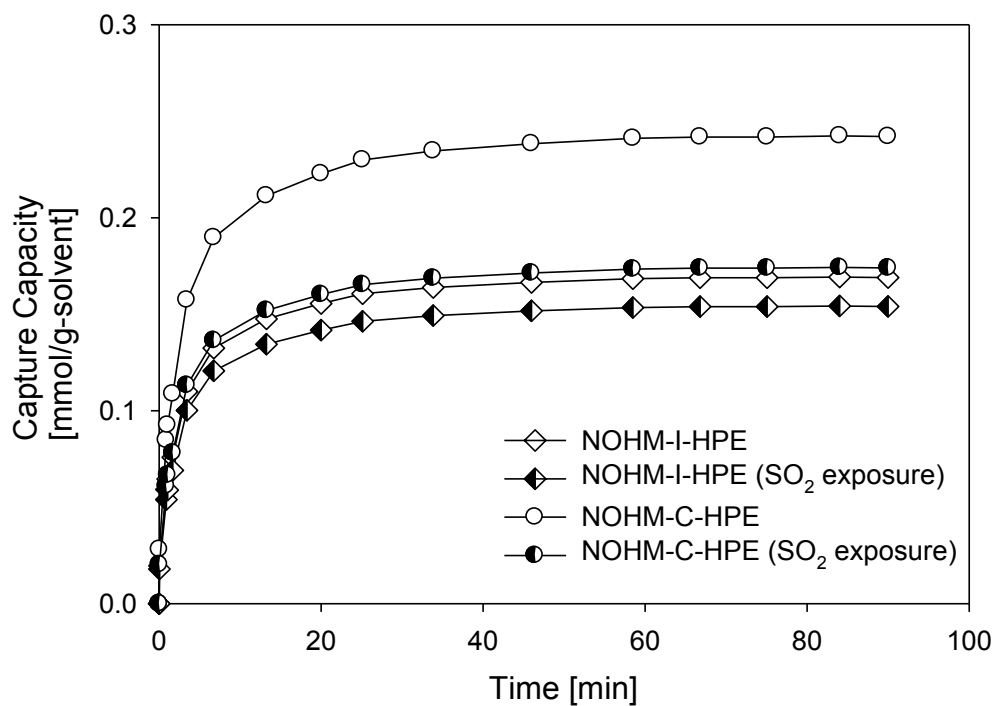


Figure 7-3 CO₂ capture capacities of SO₂-exposed and pristine NOHMs (NOHM-I-HPE and NOHM-C-HPE) at $P_{\text{CO}_2} = 0.2\text{MPa}$ and 25 °C.

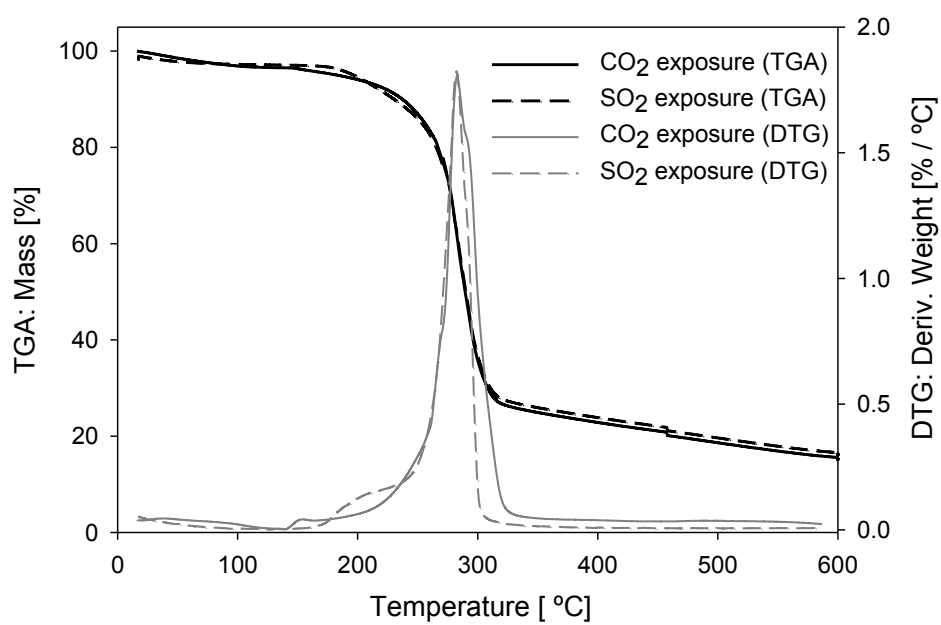


Figure 7-4 Derivative weight changes of NOHM-I-HPE after exposure to SO₂ and CO₂. (ramping rate: 5 °C/min in oxygen environment)

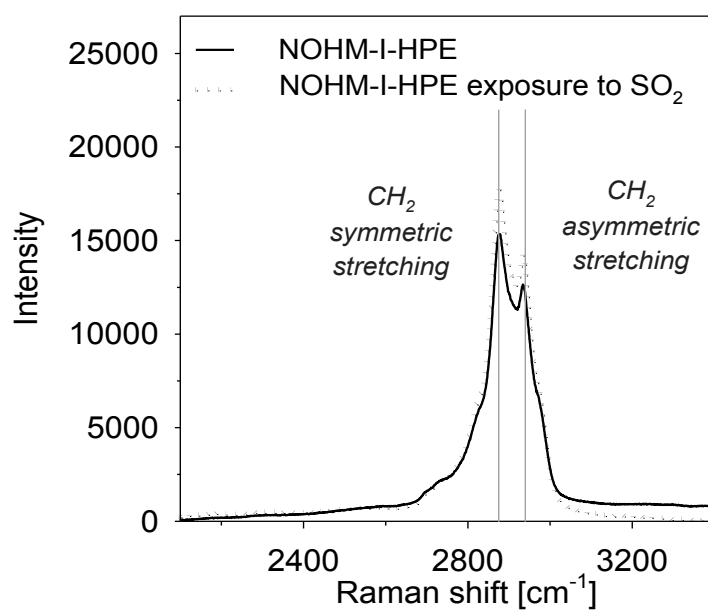


Figure 7-5 Raman spectra of NOHM-I-HPE before and after SO₂ exposure (P = 0.3 MPa) at 25 °C.

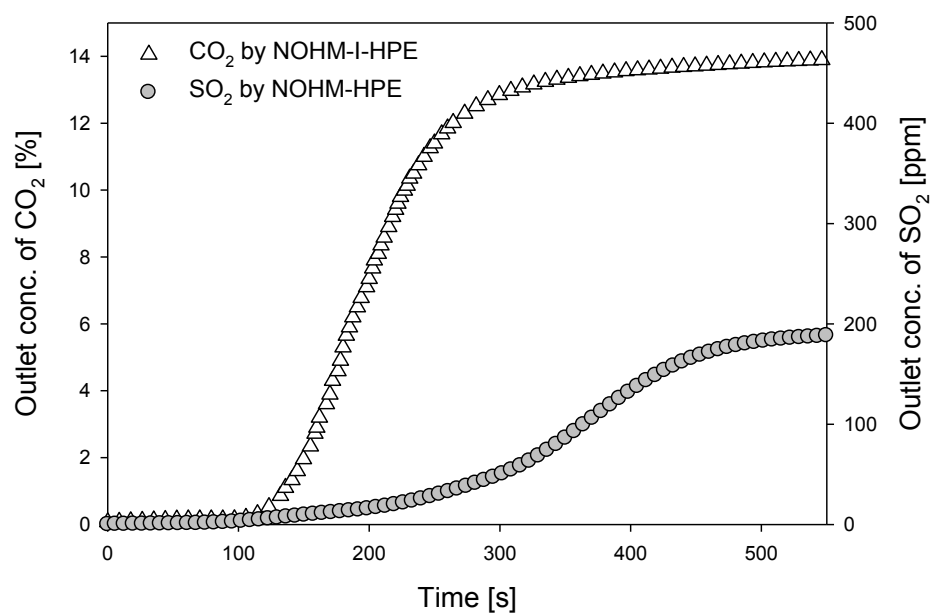


Figure 7-6 Breakthrough curves for the removal of CO₂ and SO₂ using NOHMs at 25 °C (CO₂ inlet = 14% and SO₂ inlet = 200 ppm in N₂)

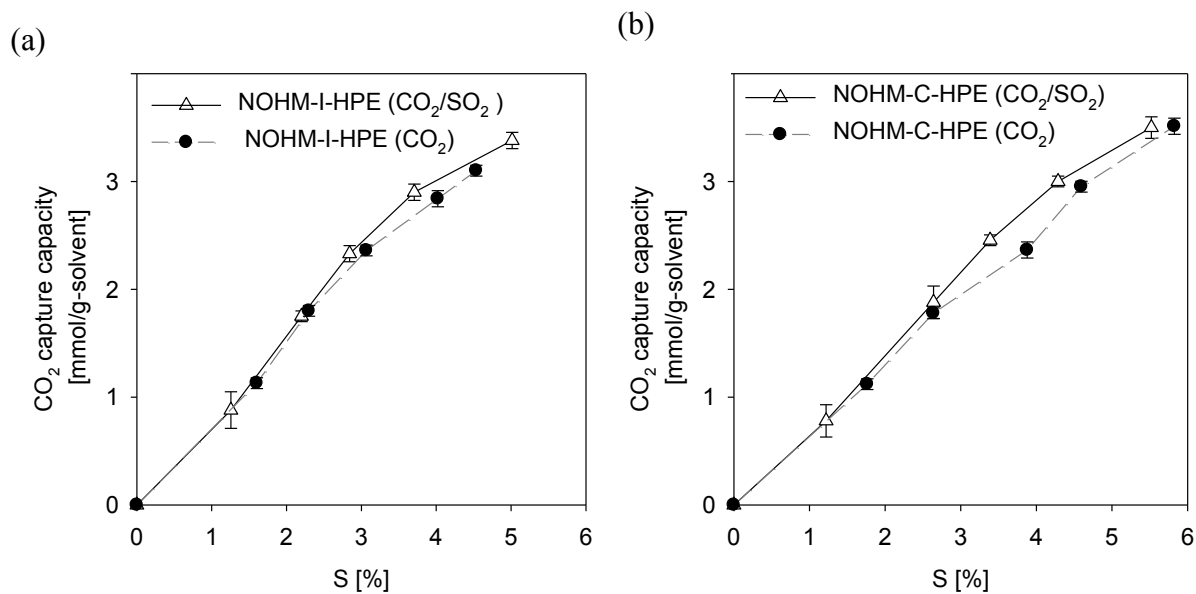


Figure 7-7 Effect of SO₂ on CO₂-induced swelling of (a) NOHM-I-HPE and (b) NOHM-C-HPE

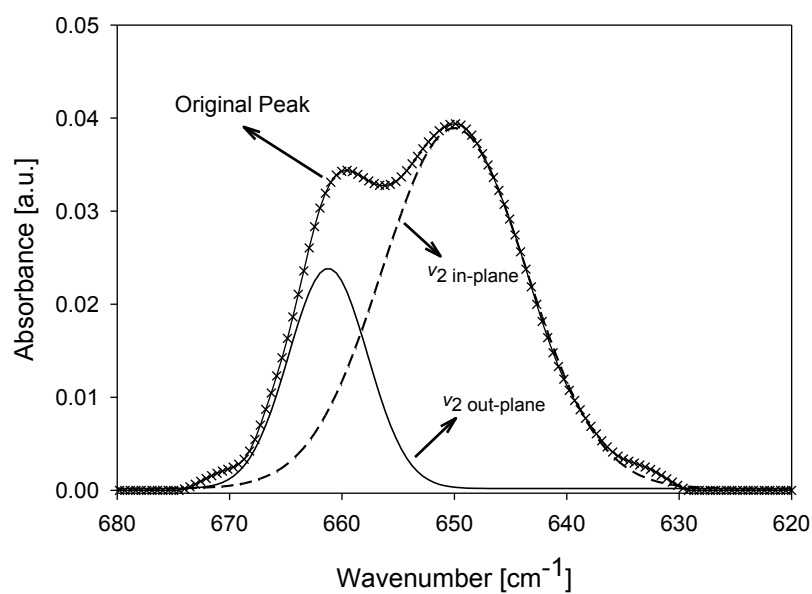
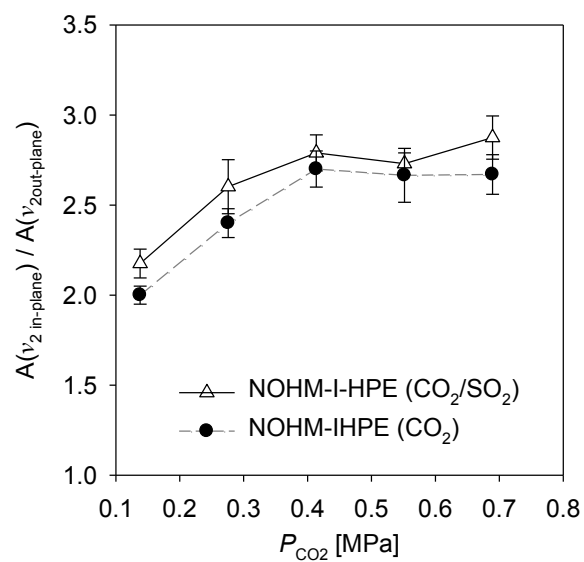


Figure 7-8 ATR FT-IR spectra of ν_2 bands of CO_2 and deconvoluted ν_2 bands of CO_2 absorbed in NOHM-I-HPE at 0.41 MPa of CO_2/SO_2 .

(a)



(b)

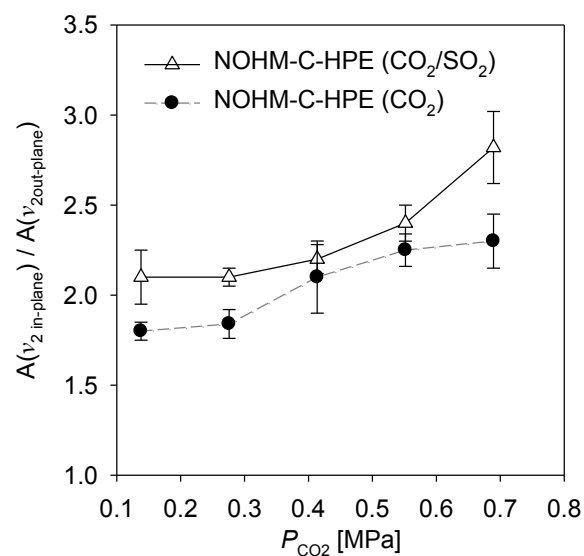


Figure 7-9 Effect of SO_2 on area ratios of in-plane ($\nu_{2,\text{in-plane}}$) to out-of-plane ($\nu_{2,\text{out-of-plane}}$) bending modes of CO_2 absorbed in (a) NOHM-I-HPE and (b) NOHM-C-HPE.

Reference

- Huang, J., Riisager, A. Wasserscheid, P. and Fehrmann, R., "Reversible physical absorption of SO₂ by ionic liquids", *Chem. Commun.*, 38, 4027-4029, 2006.
- Larsson, K. and Rand, R. P., "Detection of changes in the environment of hydrocarbon chains by raman spectroscopy and its application to lipid-protein systems", *Biochimica et Biophysica Acta (BBA) - Lipids and Lipid Metabolism*, 326, 245-255, 1973.
- Lin, K.-Y. A. and Park, A.-H. A., "Effects of Bonding Types and Functional Groups on CO₂ Capture using Novel Multiphase Systems of Liquid-like Nanoparticle Organic Hybrid Materials", *Environmental Science & Technology*, 45, 6633-6639, 2011.
- Orendorff, C. J., Ducey, M. W. and Pemberton, J. E., "Quantitative Correlation of Raman Spectral Indicators in Determining Conformational Order in Alkyl Chains", *The Journal of Physical Chemistry A*, 106, 6991-6998, 2002.
- Park, Y., Decatur, J., Lin, K.-Y. A. and Park, A.-H. A., "Investigation of CO₂ capture mechanisms of liquid-like nanoparticle organic hybrid materials via structural characterization", *Physical Chemistry Chemical Physics*, 13, 18115-18122, 2011.
- Petit, C., Park, Y., Lin, K.-Y. A. and Park, A.-H. A., "Spectroscopic Investigation of the Canopy Configurations in Nanoparticle Organic Hybrid Materials of Various Grafting Densities During CO₂ Capture", *The Journal of Physical Chemistry C*, 2011.
- Rodriguez, R. H., R.; Archer, L. A.; Giannelis, E. P., "Nanoscale Ionic Materials", *Adv. Mater.*, 20, 4353-4358, 2008.
- Park, Y., "Specific interactions between phosphorus compounds and carbon dioxide: Ab initio approach", *The Journal of Supercritical Fluids*, 36, 154-159, 2005.

CHAPTER 8

VISCOSITY AND CO₂ DIFFUSIVITY IN NOHMs AND POTENTIAL REACTOR DESIGN

This chapter is based on the following manuscript in preparation:

K.-Y. A. Lin, and A.-H. A. Park " Effects of Structural Parameters of Liquid Nanoparticle Organic Hybrid Materials on Their Viscosity and Carbon Dioxide Diffusivity using ATR FTIR ", 2012.

8.1 Introduction

Knowledge of the effect of NOHMs' viscosity on mass transfer rates is essential. In order to implement CO₂ capture using NOHMs at a large scale, viscosity and CO₂ diffusivity data are important information for designing an effective process for CO₂ capture using NOHMs.

The viscosity of NOHMs and CO₂ diffusivity in NOHMs were measured and reported in this chapter. Since NOHMs are tunable hybrid materials, structural parameters such as core size and core fraction are also varied to determine their relationship to the measured values. In particular, ionically tethered NOHMs were prepared and focused in this chapter, since there is no task-specific functional group. Therefore, the effects of structural parameters and temperature on CO₂ diffusivity can be explored. Additionally, the effect of temperature on CO₂ capture capacity was also investigated to obtain an optimal operation temperature.

8.2 Experimental

8.2.1 NOHMs Preparation

Ionically tethered NOHMs were synthesized according to previous procedures. (Rodriguez 2008; Lin and Park 2011) Colloidal silica suspensions of 7, 12 and 22 nm nanoparticles were used. When the sulfonic-acid functionalized nanoparticle suspension was prepared, polyetheramine (Jeffamine M-2070, HPE) was used. The diluted solution of the polyetheramine (10 wt%) was added dropwise into the suspension. The resulting solution was then dried under reduced pressure at 35 °C for 48 hours to yield the product as a yellowish liquid product. For NOHM-I-HPE with various core fractions, different amounts of the polyetheramine were added in the preparation and core fractions were determined by a thermogravimetric analyzer. According to

the classification of NOHMs, the resulting NOHM prepared in this chapter is named as “NOHM-I-HPE”.

An ionized HPE was prepared for the measurement of CO₂ diffusion without any nanoparticles. The preparation of the ionized HPE began by diluting HPE to 30 wt% solution and 3-(trihydroxysilyl)-1-propane sulfonic acid to 35 wt%. HPE solution was dropwise added to the solution of 3-(trihydroxysilyl)-1-propane sulfonic acid while monitoring pH. An equivalent point used to determine that HPE and 3-(trihydroxysilyl)-1-propane sulfonic acid was at a 1:1 mole ratio. The mixture then was placed under reduced pressure to remove solvents and yield the product, which appeared as a colorless oil.

8.2.2 Viscosity Measurement

The viscosity of NOHMs samples was measured using a Viscopro 2000 viscometer (Cambridge Viscosity) equipped with a water circulation system (Jalubo USA Inc.) to control the temperature. 1.5 mL of a liquid sample was loaded in the sample compartment and the viscosity was measured at various temperatures (from 40 to 90 °C) and ambient pressure.

8.2.3 CO₂ Diffusivity and CO₂ Capture Capacity using the ATR FT-IR

Attenuated total reflectance (ATR) Fourier-transformed infrared (FT-IR) spectrometry (shown in Figure 3-5) has been developed to characterize solute diffusion in thin films (Heinrich et al., 1990; Fieldson and Barbari 1993; Wurster et al., 1993; Buraphacheep et al., 1994; Farinas et al., 1994; Hellstern and Hoffmann 1995; Kazarian et al., 1996) thus, CO₂ diffusivity in NOHMs was measured by the ATR FT-IR spectrometer (Nicolet 6700, Thermo Fisher Scientific Inc.) with a data acquisition software. The FT-IR equipped with deuterated triglycine sulfate (DTGS)

detector was used to measure the CO₂ capture capacity and diffusivity of NOHMs. All spectra were obtained with a resolution of 4 cm⁻¹, and a spectrum range of 4000 cm⁻¹ – 525 cm⁻¹. Interferograms were multiplied by the Norton–Beer “medium” apodization function prior to Fourier transformation.

A high-pressure cell was equipped with the ATR FT-IR spectrometer (as shown in Figure 3-5). The infrared beam of the FT-IR was focused with ZnSe lenses. The specimen was positioned on top of the diamond crystal mounted on the heating plate connected with a PID temperature controller. The incident angle of infrared beam was 43° (±1°). The pressure cell was connected to a pressure cylinder (Swagelok) to introduce a desired pressure (0.1 MPa).

The samples were deposited onto the ATR crystal and the thickness of the sample layer was determined using a micrometer-screw caliper. Desired temperatures (25 °C – 80 °C) were maintained and the ATR cell was loaded onto the FT-IR and the first spectrum was recorded. CO₂ was then injected into the system at a pressure of 0.1 MPa and spectra was recorded every 4 seconds until equilibrium was reached. For the CO₂ capture capacity, details can be found in Section 5.2.2 and 5.3.4.

8.3 Results and Discussion

8.3.1 Characterization of NOHMs

Since NOHMs are tunable hybrid materials, their viscosity can be varied depending on their structural parameters. Thus, a series of NOHMs with different core sizes and core fractions were prepared. For NOHMs with different core sizes, NOHM-I-HPE of 7, 12, 22 nm core with a fixed core fraction, 15 wt%, were prepared. For NOHMs with different core fractions, NOHM-I-HPE of 7 nm core with 15, 20, 25, 30, and 40 wt% core fractions and NOHM-I-HPE of 12 nm core

with 15, 20, 30 wt% core fractions. Samples were analyzed using the FT-IR to verify the reaction between the primary amines and the surface functional groups of the nanoparticle cores (i.e., ionization with sulfonic acid). As shown in Figure 8-1, the primary amine of the counter ion was protonated by the sulfonic acid present on the surface of the core. The presence of the protonated amine (NH_3^+) is evidence for the polymeric counter ion tethered to the core. From the FT-IR, an absorption band of the protonated amine of ionic bonding between the polyetheramine and the sulfonic acid was observed at 1530 cm^{-1} ($\delta_s(\text{NH}_3^+)$), confirming the successful attachment of polymer chains to the surface-functionalized nanoparticle (Cook 1964; Park et al., 2011).

8.3.2 Effect of Core Size on Viscosity

After characterization of all NOHMs, viscosities of all NOHMs at various conditions were measured. In addition to NOHMs, it is also useful to know the viscosity of the virgin polyetheramine since all NOHMs were synthesized with the same polyetheramine. The viscosity of the polyetheramine at $40\text{ }^\circ\text{C}$ was $2\text{ Pa}\cdot\text{s}$. NOHM-I-HPE of 7, 12, and 22 nm core with a fixed core fraction 15 wt% were prepared with the same polyetheramine. The viscosity was measured and shown in Figure 8-2. At $40\text{ }^\circ\text{C}$, viscosities of three NOHM-I-HPE of 7, 12 and 22 nm core were around $10\text{ Pa}\cdot\text{s}$. Compared to the unbound polyetheramine, NOHMs exhibited significantly higher viscosities because of the addition of nanofillers (Song and Jin 2010). Three NOHMs with different core sizes all exhibited a lower viscosity at a higher temperature. Viscosity of NOHMs can be decreased by around 80% with a 50-degree increase in temperature. Although the core sizes between three NOHMs were considerably distinct (7 – 22 nm), the effect of core size on viscosity was insignificant. The NOHMs show comparable viscosities over the temperature

range, except a slightly higher viscosity seen in NOHM-I-HPE of 22 nm core at low temperatures.

8.3.3 Effect of Core Size on CO₂ Diffusivity

The CO₂ diffusivity, or diffusion coefficient (D_{CO_2}), in NOHMs was evaluated using the ATR FT-IR spectroscopy by monitoring the absorbance (A) of the CO₂ stretching band ($\sim 2330 \text{ cm}^{-1}$) (Park et al., 2011) as a function of time after introduction of CO₂ into the high pressure cell. The high pressure cell contained NOHMs deposited on the ATR crystal. As CO₂ diffuses into the materials, A increased until reaching an equilibrium (A_{eq}). The relationship between A , A_{eq} and D_{CO_2} can be expressed as:

$$\frac{A}{A_{eq}} = 1 - \frac{4}{\pi} \sum_k \left[\frac{(-1)^k}{2k+1} \right] \text{EXP} \left[\frac{-(2k+1)^2 \pi^2 D t}{4l^2} \right] \quad (8-1)$$

where t refers to the time and l refers to the sample thickness. At sufficiently large time ($t > 4l^2/\pi^2 D$), the first term in the summation of equation (8-1) dominates and A/A_{eq} can be expressed as (Farinas et al., 1994)

$$\frac{A}{A_{eq}} = 1 - \frac{4}{\pi} e^{-\frac{\pi^2 D_{CO_2} t}{4l^2}} \quad (8-2)$$

Consequently, by plotting $\ln \left[\frac{\pi}{4} \left(1 - \frac{A}{A_{eq}} \right) \right]$ as a function of t , and fitting the obtained curve with a linear regression, D_{CO_2} can be determined. The changes in A/A_{eq} of CO₂ in NOHM-I-HPE of 12 nm core with 15 wt% core fraction as a function of time at various temperatures were plotted in Figure 8-3. As the temperature was increased from 25 to 80 °C, the CO₂ sorption kinetics were accelerated, indicating a faster CO₂ diffusion in NOHMs.

CO₂ diffusivities in NOHM-I-HPE of 7, 12, and 22 nm core were plotted in Figure 8-4. CO₂ diffusivities of the three NOHM-I-HPE were all about 2.5×10^{-7} cm²/s at 25 °C. In comparison with CO₂ diffusivity in the polyetheramine, $3.0 (\pm 0.1) \times 10^{-7}$ cm²/s, CO₂ diffusivity in NOHM-I-HPE was smaller. Although the polyetheramine was 80% less viscous than NOHMs, the CO₂ diffusivity in the polyetheramine was not 5-fold more than NOHM-I-HPE. This may be attributed to the existence of primary amine in the polyetheramine. The primary amine has been shown to react with CO₂ to form carbamate which consequently slows CO₂ diffusion into the bulk of sample (Qi et al., 2011), lowering CO₂ diffusivity.

Besides the formation of carbamate, CO₂ diffusivity in HPE is inherently distinct from CO₂ diffusivity in NOHMs, because NOHMs contain silica nanoparticles which are not porous and permeable. CO₂ molecule only can diffuse through the canopy of NOHMs, which is HPE and the silane. Thus, CO₂ diffusivity in NOHMs is an effective diffusion coefficient which should consider the volume fraction of the canopy, tortuosity of NOHMs for CO₂ diffusion and a restrictive factor Kr_{CO_2} , as shown in Figure 8-5. The tortuosity is defined as the ratio of the length of CO₂ diffusion pathway to the thickness of a NOHMs sample. Kr_{CO_2} accounts for interfering collisions of CO₂ within the pathway wall of nanoparticles. According to Beck and Schultz (Beck and Schultz 1970), the modified restrictive factor can be expressed as

$$Kr_{CO_2} = \left[1 - \frac{d_m}{d_H}\right]^4 \quad [d_m/d_H] \leq 1 \quad (8-3)$$

where d_m is the diameter of CO₂ molecule and d_H is the hydrodynamic diameter of the canopy which is the medium allowing CO₂ to diffuse through. d_H can be obtained from dividing the

volume fraction of canopy by the total surface area of nanoparticles in NOHMs. The resulting effective CO₂ diffusivity can be expressed as (Seader et al., 2010)

$$D_{e,CO_2} = \frac{\epsilon D_{CO_2}}{\tau} K_{r,CO_2} \quad (8-4)$$

where D_{e,CO_2} is effective CO₂ diffusivity, ϵ , the volume fraction, τ , the tortuosity and K_{r,CO_2} , restrictive factor.

CO₂ diffusion in unbound HPE would involve the formation of carbamate which does not form in NOHM-I-HPE due to unavailability of amine functional group. Thus, an ionized HPE was prepared by ionizing HPE with the 3-(trihydroxysilyl)-1-propane sulfonic acid (THOPS) and D_{CO_2} of ionized HPE was experimentally measured. Next, the modified pore diffusion model that incorporates the volume fraction of the diffusion medium, the tortuosity and the restrictive factor was used to obtain the estimated D_{e,CO_2} denoted as ${}^eD_{e,CO_2}$. The ionized HPE exhibited a relatively higher diffusivity, $5.5 (\pm 0.2) \times 10^{-7} \text{ cm}^2/\text{s}$ than HPE, because the primary amine was used to form ionic bond, and unavailable to form carbamate which can slow the CO₂ diffusion. For the estimation of the volume fraction of the diffusion medium (i.e., polymeric canopy), ϵ , the core fraction (wt%) of NOHMs obtained from the thermogravimetric analysis was used. In order to fit the NOHMs into the modified pore diffusion model, a range of the tortuosity, τ , from 1.5 to 2.5 was selected. The minimum value of τ was chosen as 1.5 to represent a relatively straightforward CO₂ diffusion pathway inside NOHMs, while 2.5 was selected for τ to account for relatively complex CO₂ diffusion pathway inside NOHMs. For K_{r,CO_2} , molecular diameter of CO₂ was used as d_m . D_{CO_2} of the ionized HPE was then used to estimate ${}^eD_{e,CO_2}$ for NOHMs with

various structural parameters. The comparison of $^eD_{e,CO_2}$ and experimentally measured D_{e,CO_2} ($^mD_{e,CO_2}$) are listed in Table 8-1.

8.3.4 Effect of Core Fraction on Viscosity and CO₂ Diffusivity

Another structural parameter investigated was the core fraction. Viscosity of NOHMs with different core fractions was also measured and shown in Figures 8-6 and 8-7. Figure 8-6 shows the viscosity of NOHM-I-HPE of 7 nm core with respect to core fraction. The viscosity increased by 20% as the core fraction changed from 15 to 30 wt%, indicating the significant effect of core fraction on the viscosity. In Figure 8-7, NOHM-I-HPE of 12 nm core also showed higher viscosity at higher core fraction. The viscosity also increased by about 20% by raising the core fraction from 15 to 30 wt%.

The trend observed in both the 7 nm and 12 nm core samples suggests that an increase in viscosity is proportional to the change in core fraction and that the viscosity is mainly determined by the amount of polymer chains present in a NOHMs sample, instead of the core size. This behavior also agrees with the observation seen in the effect of core size on viscosity and CO₂ diffusivity.

For CO₂ diffusivity ($^mD_{e,CO_2}$), a significant effect of core fraction is also observed from Figure 8-6 and Figure 8-7. CO₂ diffusivity was pronouncedly decreased as the core fraction increasing. With a 7 nm core, CO₂ diffusivity in NOHM-I-HPE decreased from 2.58×10^{-7} cm²/s to 0.76×10^{-7} cm²/s as the core fraction increased from 15 to 40%. A similar trend was also observed in the case of NOHM-I-HPE of 12 nm core: CO₂ diffusivity decreased from 2.62×10^{-7} cm²/s to 1.9×10^{-7} cm²/s as the core fraction changed from 15 to 30 wt%.

As shown in Table 8-1, a change in the core fraction can result in different ε and also Kr_{CO_2} . As ε and also Kr_{CO_2} decrease (due to a higher silica core fraction), $^eD_{e,CO_2}$ is expected to be smaller. $^eD_{e,CO_2}$ of NOHM-I-HPE of 7 nm and 12 nm core are significantly decreased as the core fraction changes from 15 to 40 wt% and 30 wt% regardless of the value of τ . The trend also agrees with $^mD_{e,CO_2}$, measured by the ATR FT-IR. By comparing the ratio of $^eD_{e,CO_2}/^mD_{e,CO_2}$, it was noticed that the ratio becomes larger as the core fraction is higher. However the ratio can be closer to 1.0 as τ is changed from 1.5 to 2.5. This suggests that the actual tortuosity, τ , should be much higher than the assumption (i.e., 2.5) as the core fraction is higher. That is to say that an actual pathway for CO₂ diffusion becomes longer as more silica nanoparticles are incorporated in NOHMs. Based on this observation, a low core fraction in NOHMs is desired to reduce viscosity of NOHMs.

All $^eD_{e,CO_2}$ are less than D_{CO_2} because the volume fraction becomes less than 1.0 and $\tau \geq 1.0$ as nanoparticles are incorporated in HPE. Regardless the value of τ , when core size is increased, $^eD_{e,CO_2}$ has a tendency to increase, which agrees with the experimentally measured $^mD_{e,CO_2}$. Since NOHM-I-HPE of various core sizes have the same “ ε ”, this trend in $^mD_{e,CO_2}$ is mainly due to different K_{ri} in the three NOHM-I-HPE. NOHM-I-HPE of 22 nm core had a larger d_H and therefore a higher K_{ri} , which yielded a higher D_{e,CO_2} . Even though $^mD_{e,CO_2}$ and $^eD_{e,CO_2}$ are relatively high as core sizes increase, the effect of core size on D_{e,CO_2} (either $^eD_{e,CO_2}$ or $^mD_{e,CO_2}$) was not significant compared to the effect of core.

8.3.5 Effect of Temperature on CO₂ Diffusivity

In addition to investigating effects of structural parameters on viscosity and CO₂ diffusivity, the effect of temperature was also examined. Since NOHMs are proposed for the post-combustion

CO₂ capture, the effect of elevated temperatures on NOHMs' viscosity and especially CO₂ diffusivity is important. Figure 8-8 shows the CO₂ diffusivity in the NOHM-I-HPE of 12 nm core at various temperatures. At higher temperatures, CO₂ diffusivity was significantly improved and was attributed to lower viscosities at these temperatures. CO₂ diffusivity increased from $2.62 \times 10^{-7} \text{ cm}^2/\text{s}$ to $8.25 \times 10^{-7} \text{ cm}^2/\text{s}$ as the temperature as adjusted from 25 to 80 °C. Therefore, high-temperature condition can facilitate CO₂ diffusion during CO₂ capture.

The effect of temperature on CO₂ capture capacity was also measured via the ATR FT-IR. The CO₂ capture capacity at $P_{\text{CO}_2} = 0.1 \text{ MPa}$ versus various temperatures is shown in Figure 8-8. The CO₂ capture capacity was pronouncedly reduced as the temperature increased. As mentioned earlier, NOHM-I-HPE is a not task-specific functionalized NOHMs. Therefore CO₂ capture mechanism of NOHM-I-HPE is mainly physical sorption. According to Henry's Law, gas solubility in a solvent decreases at higher temperatures. Here it was observed that the CO₂ capture capacity of NOHM-I-HPE was lowered at the elevated temperatures. Since higher temperatures can boost CO₂ diffusivity but lower CO₂ capture capacity, the optimal temperature range for NOHM-I-HPE to capture CO₂ was determined to be 40 – 70 °C which is comparable to the operation temperature of the amine scrubbing. However, CO₂-rich NOHMs can be regenerated at 120 °C or higher temperatures without the loss of materials while the amine-based solvents would degrade and evaporate at these temperatures.

8.4 Potential Reactor Designs

NOHMs show promising CO₂ capture capacity, selectivity and recyclability. Several structural parameters can determine the viscosity of NOHMs and therefore impact CO₂ diffusivity. Depending on viscosity of NOHMs, a number of applications can be employed for CO₂ capture

and also other fields. For CO₂ capture, if the viscosity of NOHMs is appropriately lowered by manipulating core sizes and core fractions at an optimal operation temperature, NOHMs could be used in applications such as a spraying tower (shown in Figure 8-9).

Fluid NOHMs could be sprayed from the top of the tower to form droplets to increase contact area for CO₂ capture. CO₂-rich NOHMs then would then be transported to a stripper tower to regenerate and release CO₂. Since the vapor pressure of NOHMs is negligible, the stripper temperature can be operated at 120°C without evaporation of NOHMs. For relatively viscous and amine functionalized NOHMs (e.g. NOHM-I-HPE), a supported liquid membrane (Figure 8-10) can be employed. NOHMs could be coated on fibers or filled inside the membrane to increase the contact area.

Another advanced potential application is to use NOHMs to capture CO₂ and convert it into valuable products, like alcohols. It is well known that removal of CO₂ from the CO₂-loaded capture media (regeneration of the capture media) is one of the most energy-intensive steps. If the regeneration of CO₂ capture media and CO₂ conversion into other chemicals can be achieved simultaneously, a significantly amount of energy for the regeneration can be saved and valuable chemicals can add economical benefit. Since NOHMs are highly tunable hybrid materials, they can be designed to serve as a dual-purpose smart material for CO₂ capture and the photocatalytic conversion of CO₂ (Figure 8-11).

NOHMs can be manipulated to comprise photocatalytically active cores (e.g. titanium dioxide nanoparticles) tethered with a canopy, comprised of functional polymers. The canopy would contain task-specific functional groups to capture CO₂ with a goal of 90% efficiency. The CO₂ would then be photoelectrochemically converted, in the same reactor, into alcohols with the aid of electronically conductive functional groups. Thus, after the CO₂ is captured, the CO₂-rich

NOHMs will be used as both the source of CO₂ and electrolyte in the photoelectrochemical conversion step in a single reactor at slightly elevated temperatures. The CO₂-lean smart materials will then be used for the next sequence of CO₂ capture and conversion. Since the same reactor will be employed as a CO₂ capture and conversion unit, no additional energy consumption would be required to transport the capture media back and forth between each step. Therefore the operational complexity and cost will be significantly reduced.

8.5 Conclusions

The viscosity and CO₂ diffusivity in NOHMs with various structural parameters were measured. Effects of core size and core fraction on viscosity and CO₂ diffusivity were investigated and the pore diffusion model was employed to analyze these variables. Although core size changed from 7 to 22 nm in NOHMs, the effect of core size was not significant on viscosity and CO₂ diffusivity as the core fraction was fixed. In contrast, the effect of core fraction was notable. A higher core fraction in NOHMs significantly resulted in a higher viscosity and lower CO₂ diffusivity. The core fraction is considered as the most influential factor to determine the viscosity in NOHMs, because the core fraction is associated with the amount of polymer chains present in NOHMs. A change in core fraction may also result in different tortuosity of CO₂ diffusion which can significantly affect CO₂ diffusivity.

The effect of temperature also contributed to improve CO₂ diffusion in NOHM-I-HPE. However, a higher temperature can be negative to CO₂ capture capacity in NOHM-I-HPE. 40 – 70 °C can be the optimal operational temperature range to obtain an improved CO₂ diffusivity in NOHM-I-HPE for CO₂ capture. In addition to the operation temperature, NOHMs can also be designed to contain a low core fraction to improve viscosity and CO₂ diffusivity simultaneously.

In our ongoing work, a new type of NOHMs was prepared with a significantly smaller core which enables NOHMs to contain much less core fraction, therefore reducing viscosity. Updated results will be published in the near future.

Once the viscosity of NOHMs can be lowered by manipulating core sizes and core fractions at an optimal operation temperature, fluid NOHMs can be used in the spraying tower to capture CO₂. For relatively viscous NOHMs, such as amine functionalized NOHMs, the supported liquid membrane system can be used by coating or filling NOHMs inside the membrane to increase contact area.

For an advanced application, NOHMs also can be even functionalized to serve as a dual-purpose smart material for CO₂ capture and the photocatalytic conversion of CO₂ to alcohols. A significantly amount of energy for the regeneration can be saved; valuable chemicals can add economical benefits for the overall process.

Table 8-1 Comparison of estimated ${}^eD_{e,CO_2}$ and measured ${}^mD_{e,CO_2}$ of NOHMs with various structural parameters at 25 °C.

Core size (nm)	Core fraction (wt%)	ε	K_{rCO_2}	τ	${}^eD_{e,CO_2}$ ($\times 10^7$, cm ² /s)	${}^mD_{e,CO_2}$ ($\times 10^7$, cm ² /s)	${}^eD_{e,CO_2}/{}^mD_{e,CO_2}$
7	15	0.92	0.94	1.5 ~2.5	3.18~2.12	2.58	1.25~0.81
	20	0.89	0.90	1.5 ~2.5	2.96~1.97	2.48	1.23~0.80
	25	0.86	0.87	1.5 ~2.5	2.76~1.84	2.23	1.29~0.82
	30	0.82	0.84	1.5 ~2.5	2.55~1.70	1.60	1.69~1.06
	40	0.75	0.76	1.5 ~2.5	2.11~1.41	0.76	3.04~1.85
12	15	0.92	0.96	1.5 ~2.5	3.24~2.16	2.62	1.26~0.82
	20	0.89	0.94	1.5 ~2.5	3.08~2.05	2.28	1.39~0.90
	30	0.82	0.90	1.5 ~2.5	2.74~1.83	1.90	1.51~0.96
22	15	0.92	0.97	1.5 ~2.5	3.30~2.20	2.70	1.24~0.81

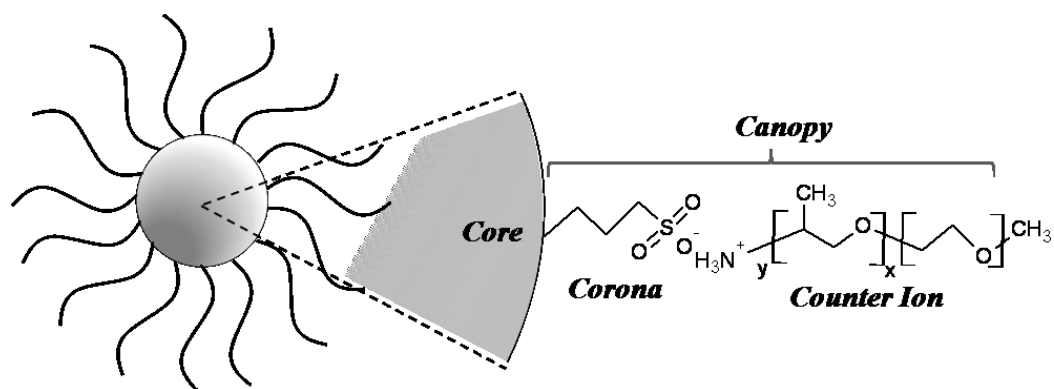


Figure 8-1 Schematic diagram of NOHM-I-HPE.

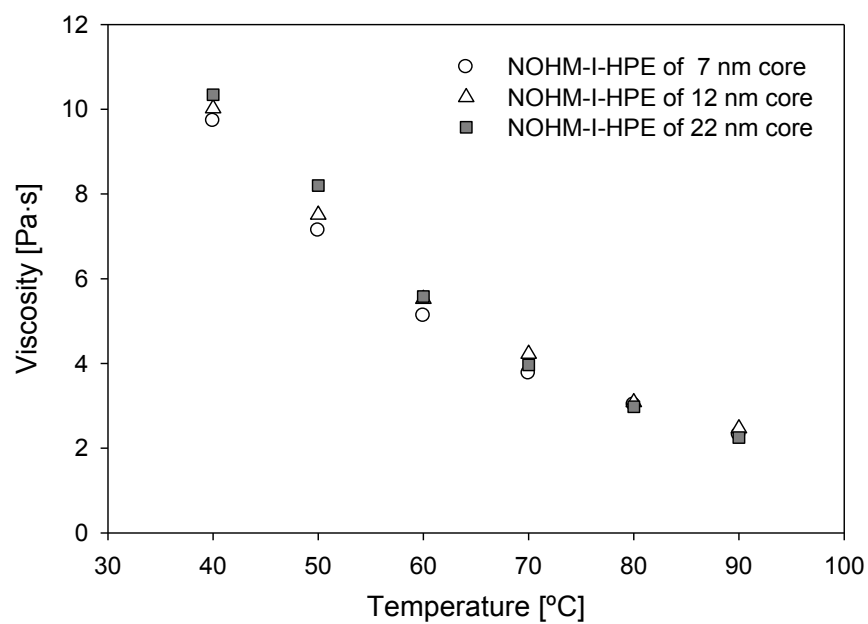


Figure 8-2 Viscosity of NOHM-I-HPE of 7, 12, and 22 core with a fixed core fraction 15 wt% at various temperatures.

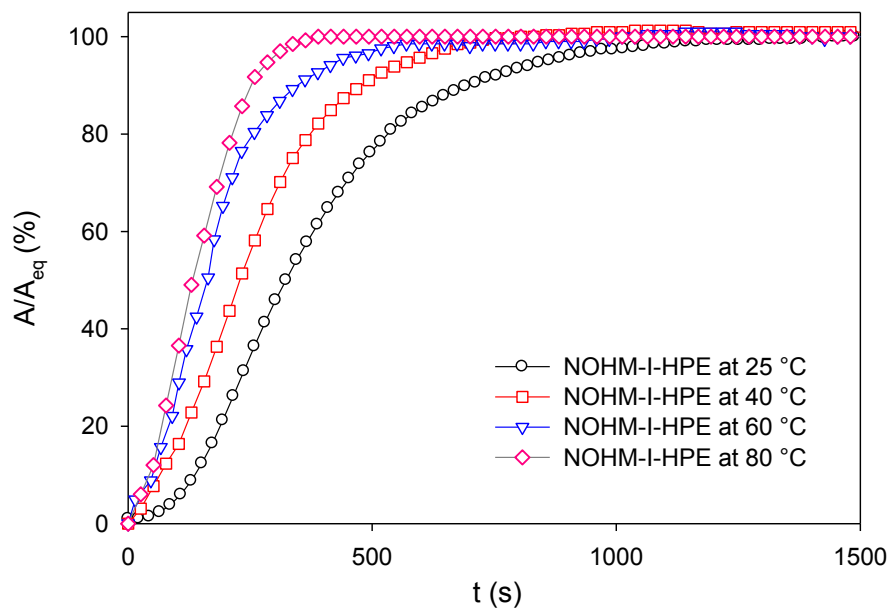


Figure 8-3 A/A_{eq} of CO_2 diffusion into NOHM-I-HPE as a function of time at various temperatures. ($P_{\text{CO}_2} = 0.1 \text{ MPa}$)

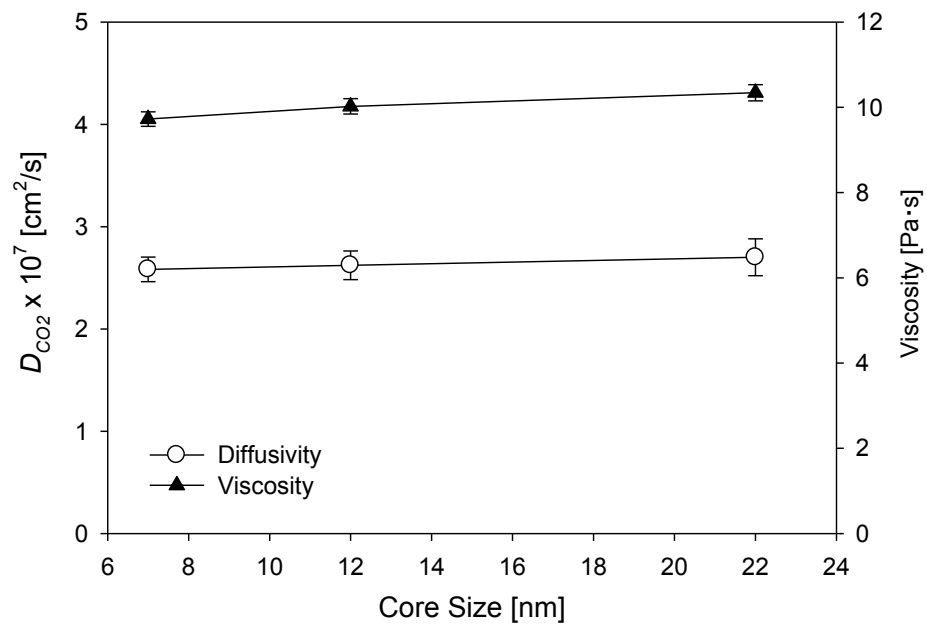


Figure 8-4 Effect of core size on viscosity at 40 °C and CO₂ diffusivity in NOHM-I-HPE of 7, 12 and 22 nm core with a fixed core fraction (15 wt%) at 25 °C

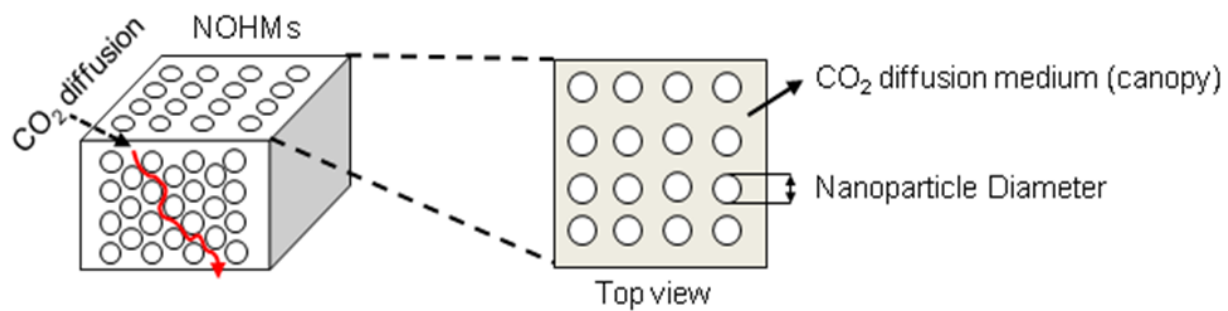


Figure 8-5 Scheme for CO₂ diffusion pathway in NOHMs and CO₂ diffusion pathway diameter

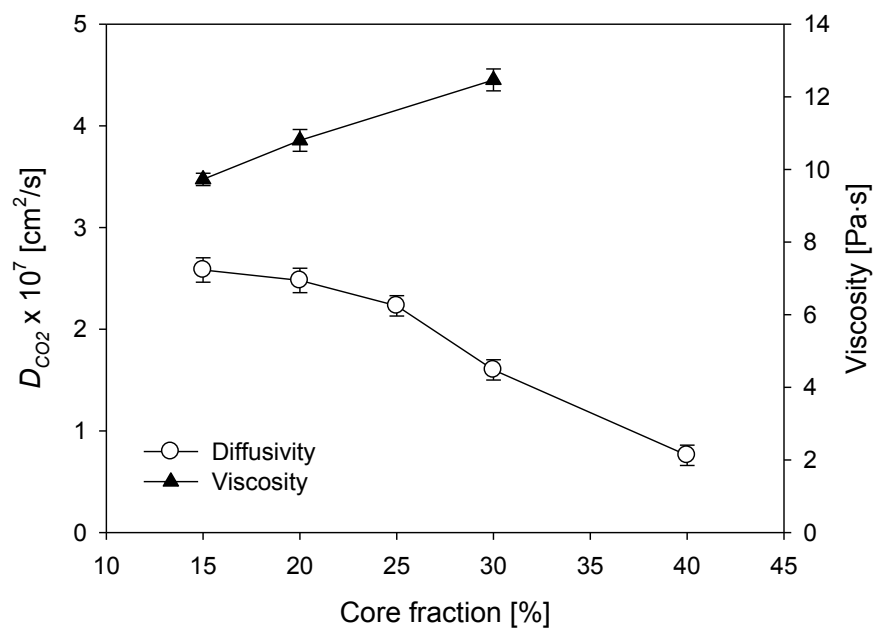


Figure 8-6 Effect of core fraction on viscosity at 40 °C and CO₂ diffusivity in NOHM-I-HPE of 7 nm core with core fraction 15, 20, 25, 30 and 40 wt% at 25 °C.

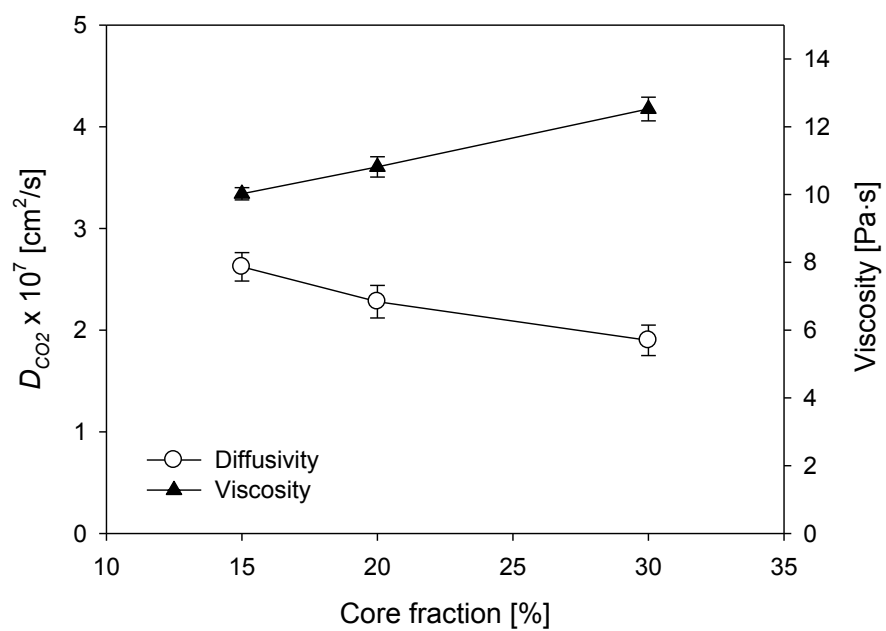


Figure 8-7 Effect of core fraction on viscosity at 40 °C and CO₂ diffusivity in NOHM-I-HPE of 12 nm core with core fraction 15, 20 and 30 wt% at 25 °C.

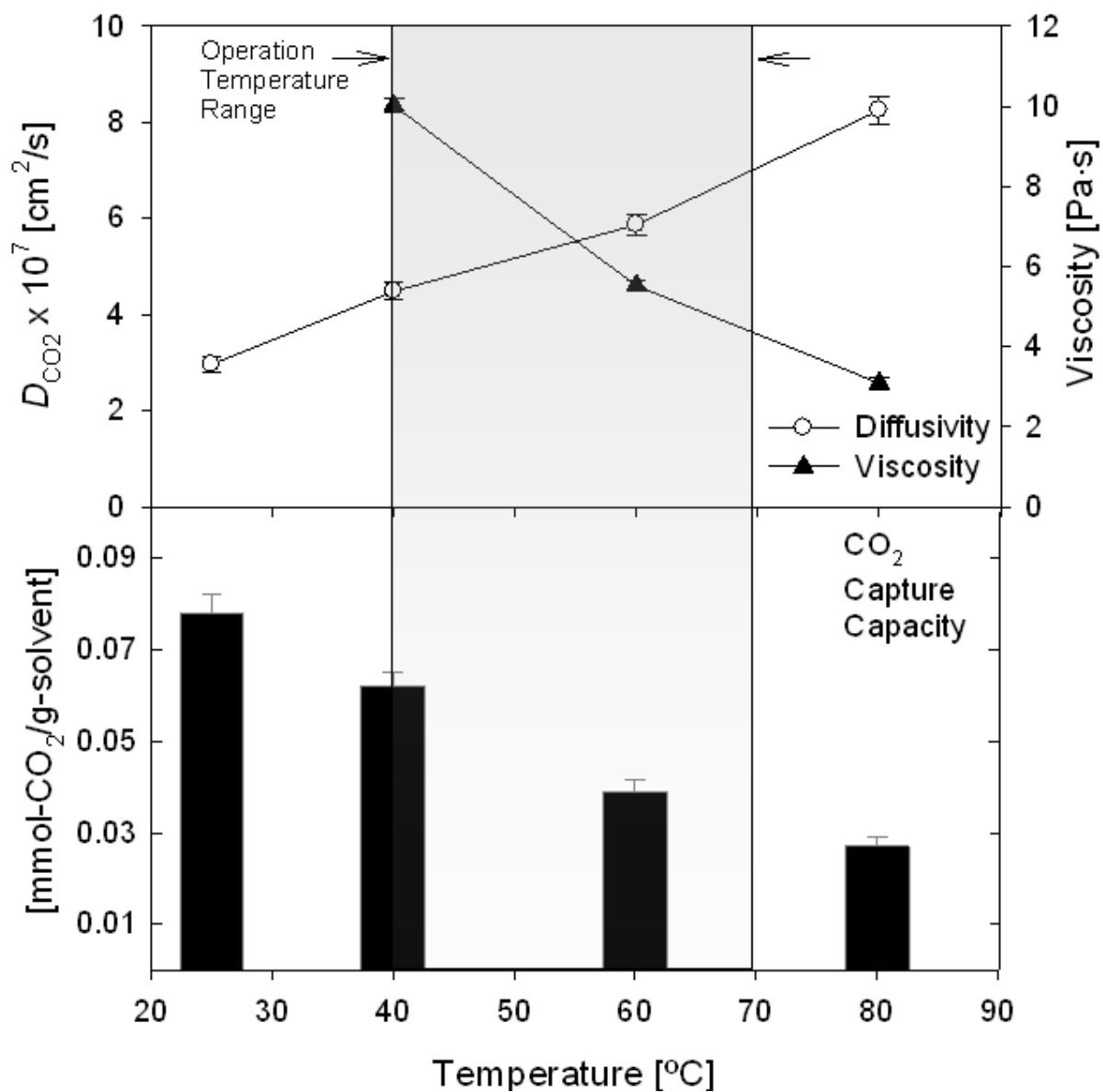


Figure 8-8 Viscosity and CO₂ diffusivity in NOHM-I-HPE with 12 core and core fraction 15 wt% at various temperatures.

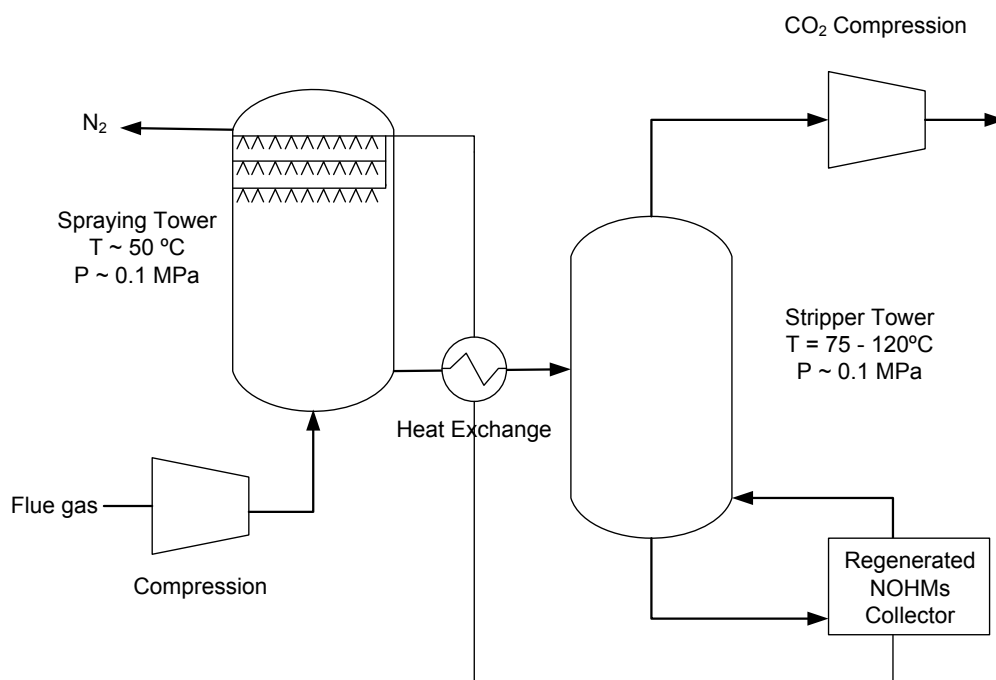


Figure 8-9 Schematic diagram of a spraying tower for CO₂ capture using Liquid-like NOHMs



Figure 8-10 Schematic diagram of a supported liquid membrane for NOHMs

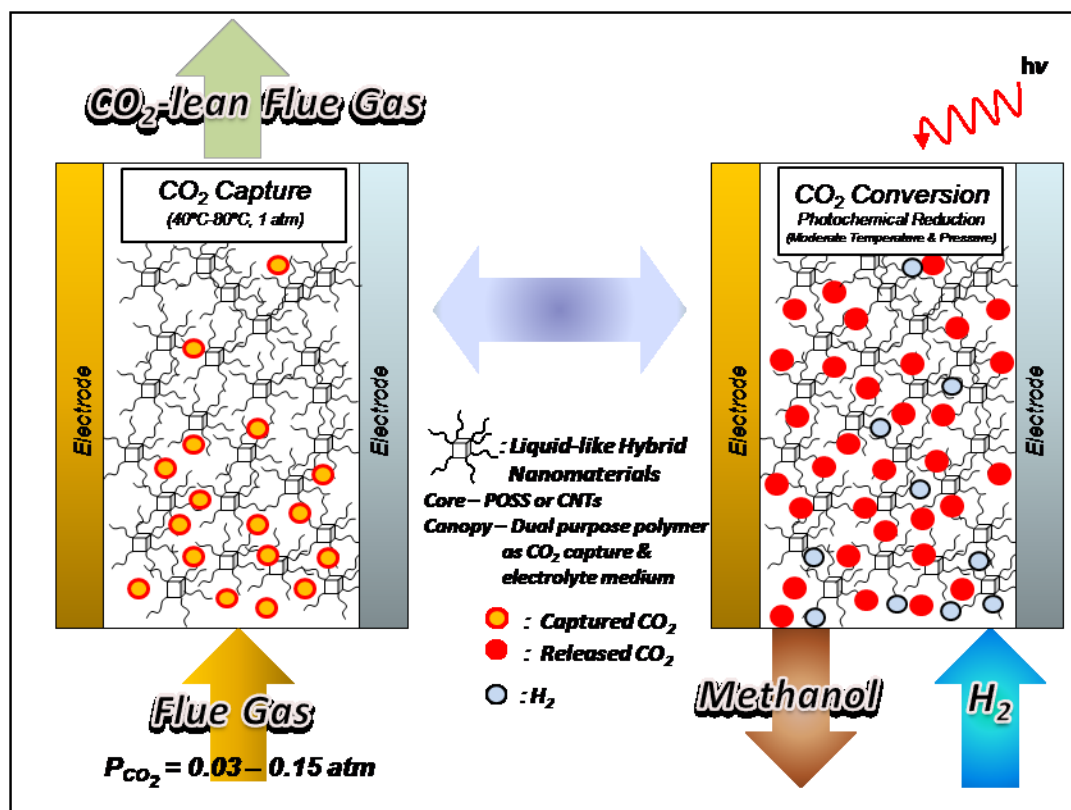


Figure 8-11 Schematic diagram of a combined technology for CO₂ capture and conversion to alcohols using photochemical NOHMs

Reference

- Beck, R. E. and Schultz, J. S., "Hindered Diffusion in Microporous Membranes with Known Pore Geometry", *Science*, 170, 1302-1305, 1970.
- Buraphacheep, V., Wurster, D. E. and Wurster, D. E., "The Use of Fourier Transform Infrared (FT-IR) Spectroscopy to Determine the Diffusion Coefficients of Alcohols in Polydimethylsiloxane", *Pharmaceutical Research*, 11, 561-565, 1994.
- Cook, D., "PROTONATION SITE IN ORGANIC BASES FROM INFRARED X—H DEFORMATION MODES", *Canadian Journal of Chemistry*, 42, 2292-2299, 1964.
- Farinas, K. C., Doh, L., Venkatraman, S. and Potts, R. O., "Characterization of Solute Diffusion in a Polymer Using ATR-FTIR Spectroscopy and Bulk Transport Techniques", *Macromolecules*, 27, 5220-5222, 1994.
- Fieldson, G. T. and Barbari, T. A., "The use of FTi.r.-a.t.r. spectroscopy to characterize penetrant diffusion in polymers", *Polymer*, 34, 1146-1153, 1993.
- Heinrich, P., Wyzgol, R., Schrader, B., Hatzilazaru, A. and Lübbers, D. W., "Determination of Organic Compounds by IR/ATR Spectroscopy with Polymer-Coated Internal Reflection Elements", *Appl. Spectrosc.*, 44, 1641-1646, 1990.
- Hellstern, U. and Hoffmann, V., "Diffusion in ultrathin films studied by time resolved FTIR-ATR spectroscopy", *Journal of Molecular Structure*, 349, 329-332, 1995.
- Kazarian, S. G., Vincent, M. F., Bright, F. V., Liotta, C. L. and Eckert, C. A., "Specific Intermolecular Interaction of Carbon Dioxide with Polymers", *Journal of the American Chemical Society*, 118, 1729-1736, 1996.
- Lin, K.-Y. A. and Park, A.-H. A., "Effects of Bonding Types and Functional Groups on CO₂ Capture using Novel Multiphase Systems of Liquid-like Nanoparticle Organic Hybrid Materials", *Environmental Science & Technology*, 45, 6633-6639, 2011.
- Park, Y., Decatur, J., Lin, K.-Y. A. and Park, A.-H. A., "Investigation of CO₂ capture mechanisms of liquid-like nanoparticle organic hybrid materials via structural characterization", *Physical Chemistry Chemical Physics*, 13, 18115-18122, 2011.
- Qi, G., Wang, Y., Estevez, L., Duan, X., Anako, N., Park, A.-H. A., Li, W., Jones, C. W. and Giannelis, E. P., "High efficiency nanocomposite sorbents for CO₂ capture based on amine-functionalized mesoporous capsules", *Energy & Environmental Science*, 4, 444-452, 2011.
- Rodriguez, R. H., R.; Archer, L. A.; Giannelis, E. P., "Nanoscale Ionic Materials", *Adv. Mater.*, 20, 4353-4358, 2008.
- Seader, J. D., Henley, E. J. and Roper, D. K., "Separation Process Principles: Chemical and Biochemical Operations", 2010.
- Song, M. and Jin, J., "Rheological Behavior of ", *Optimization of Polymer Nanocomposite Properties*, 94-121, 2010.
- Wurster, D. E., Buraphacheep, V. and Patel, J. M., "The Determination of Diffusion Coefficients in Semisolids by Fourier Transform Infrared (FT-IR) Spectroscopy", *Pharmaceutical Research*, 10, 616-620, 1993.
- Yu, H.-Y. and Koch, D. L., "Structure of Solvent-Free Nanoparticle–Organic Hybrid Materials", *Langmuir*, 26, 16801-16811, 2010.

CHAPTER 9

CONCLUSIONS AND RECOMMENDATIONS

The development of efficient CO₂ capture technologies is essential as fossil fuels will remain the dominant energy source in the foreseeable future. Currently, the amine scrubbing is the most widely employed approach to capture CO₂. However, high volatility and energy-intensive regeneration process inherently in the amine scrubbing delays its large-scale implementation. Thus, there is an urgent need to develop alternative CO₂ capture media that can be efficient and sustainable.

To achieve this goal, NOHMs have been formulated to expand the library of alternative solvents for CO₂ capture. A unit of NOHMs consists of a surface-functionalized nanoparticle that serves as a core to which polymers are tethered. The layer of polymers around the core is known as the “canopy.” Such a configuration prevents loss of polymers and enables NOHMs to exhibit near zero vapor pressure. As the canopy surrounds the core, CO₂ can be captured by not only the enthalpic effect via reactions with functional groups along the polymeric canopy but also by the entropic means via introduction of small gaseous molecules such as CO₂ to reduce the free energy of the frustrated canopy.

In this dissertation, NOHMs were designed, synthesized and evaluated for CO₂ capture properties. NOHMs were classified based on their representative phases and chemical and structural parameters. Characterization of NOHMs was conducted by employing various spectroscopic tools, such as ATR FT-IR, Raman and NMR, to confirm successful synthesis of NOHMs. Thermal stability and nanoscale configuration of NOHMs were measured using TGA and TEM, respectively. NOHMs with various chemical and structural parameters, including bonding types, functional groups, chain lengths, core sizes, and core fractions, were prepared. The effects of these parameters on CO₂ capture properties were explored in detail, including

thermal stability, thermally-induced swelling, CO₂-induced swelling and packing behavior and CO₂ capture capacity.

For thermal stability and thermally-induced swelling, in comparison to unbound polymers, NOHMs exhibited enhanced thermal stability. Such an enhancement allows NOHMs to be used in a wide-range of operational temperatures. While an unbound polymer degraded 80 wt% after a 100-cycle temperature swing, there was no significant loss in the corresponding NOHMs. Elevated temperatures also caused NOHMs to swell but the degree of thermally-induced swelling was less than that of the unbound polymers due to the restriction on the movement of the tethered polymer chains of NOHMs.

CO₂ capture capacity studies revealed that NOHMs can capture 0.1 – 0.4 mmol/g-solvent depending on partial pressure of CO₂ and temperature. The CO₂ capture mechanism was also revealed as a Lewis acid-base interaction between CO₂ and ether groups which were the most common functional groups of the polymers selected for the NOHMs synthesis (e.g. NOHM-I-HPE, NOHM-I-tPE and NOHM-I-PEG). The effect of functional groups on CO₂ capture was far more significant when amines were incorporated in NOHMs (e.g. 2.2 mmol/g-solvent in NOHM-I-PEI).

Although the enthalpic effect is pronounced, the entropic effect from NOHMs' unique structural nature, could allow CO₂ to be captured more effectively. In order to explore the entropic effect, NOHMs were synthesized to minimize the enthalpic effect for the most of structural studies, such as CO₂-induced swelling and CO₂ packing behaviors.

In comparison to the unbound polymers, NOHMs showed notably less swelling with a given CO₂ capture capacity. While NOHMs had shorter polymer chains, they showed even less swelling than NOHMs having longer polymer chains at a given CO₂ capture capacity. This may

be due to the conformational difference between NOHMs and unbound polymer, allowing more CO₂ molecules to pack within the polymer chains. For NOHMs with varied grafting densities, the differences (i.e., increased chain ordering and decreased intermolecular interactions in NOHMs compared to unbound polymer) were further pronounced by lowering the grafting density of NOHMs' canopy. These differences were attributed to the specific structural configuration of NOHMs' canopy in which polymer chains were tethered onto inorganic nanoparticle cores causing more "rigid" arrangements than that of the bulk polymer. This particular structural change in NOHMs resulted in different CO₂ packing and CO₂-induced swelling behaviors compared to those of the corresponding unbound polymer.

In order to facilitate the implementation of NOHMs for CO₂ capture, several aspects were also investigated, including impact of SO₂, viscosity of NOHMs and CO₂ diffusivity in NOHMs. For the effect of SO₂ on CO₂ capture using NOHMs, at low concentration (200 ppm SO₂ in N₂), no significant amount of SO₂ was captured in NOHMs while a considerable amount of SO₂ captured in NOHMs was observed at 3010 ppm SO₂ in N₂. As N₂ is almost insoluble in NOHMs, NOHMs showed a high selectivity toward SO₂ capture over N₂ capture. This can enable NOHMs to be a potential candidate for removal of SO₂. About 10% of CO₂ capture capacity was reduced after NOHM-I-HPE's exposure to SO₂ while in the case of NOHM-C-HPE, about 30 % of CO₂ capture capacity was reduced after the exposure to SO₂. The result of the simultaneous removal of CO₂ and SO₂ showed that when the concentration of SO₂ was low (200 ppm), NOHMs did not exhibit a noticeable selectivity toward SO₂ over CO₂. CO₂ capture capacity and CO₂-induced swelling was also measured with a mixture of CO₂/SO₂ to investigate the effect of SO₂ on CO₂ capture. While the comparable swelling behaviors were observed with a mixture CO₂/SO₂ and pure CO₂ at low pressures, the swelling behaviors of the two cases started to deviate from each

other at higher pressure. This may be attributed to the distinct packing patterns in NOHMs with the pressurization with CO₂/SO₂ compared to the pressurization with pure CO₂.

The viscosity and CO₂ diffusivity in NOHMs with various structural parameters were also measured. The effect of core size did not significantly affect viscosity and CO₂ diffusivity as the core fraction was fixed. In contrast, the effect of core fraction was notable. A higher core fraction in NOHMs significantly resulted in a higher viscosity and lower CO₂ diffusivity. The effect of raising temperature also improved CO₂ diffusion in NOHM-I-HPE. However, a higher temperature can be negative to CO₂ capture capacity in NOHM-I-HPE. To obtain an improved CO₂ diffusivity for CO₂ capture, the optimal operation temperature ranging from 40 to 70 °C was determined.

If the viscosity of NOHMs could be appropriately lowered by manipulating core sizes and core fractions at the optimal operation temperature, fluid NOHMs could be used in a spraying tower to capture CO₂. For relatively viscous NOHMs, such as amine functionalized NOHMs, the supported liquid membrane system could be used by coating or filling NOHMs inside the membrane to increase contact area. As an advanced application, NOHMs could even be functionalized to serve as a dual-purpose smart material for CO₂ capture and for photocatalytic conversion of CO₂ to alcohols. A significant amount of energy could be saved from solvent regeneration and the product would make the process economically beneficial.

This study was the first attempt to investigate CO₂ capture using NOHMs. Chemical and structural parameters of NOHMs on key factors affecting CO₂ capture were explored. The fundamental knowledge gained in this study serves as a basis for the optimal design of NOHMs for CO₂ capture as well as important information on designing nanoscale hybrid materials for other advanced environmental and energy technologies.

APPENDIX

Table A1. Abbreviations of selected cations in Ionic Liquids

Cation	Abbreviation
Butyl Nicotinate	[b ₂ Nic]
1-Butyl-2,3-Methylimidazolium	[bmmim]
1-Butyl-3-Methylimidazolium	[bmim]
1-Ethyl-2,3-Methylimidazolium	[emmim]
1-Ethyl-3-Methylimidazolium	[emim]
1-Hexyl-3-Methylimidazolium	[hmim]
1- <i>N</i> -Propylamine-3-Butylimidazolium	[pabim]
1-Octyl-3-Methylimidazolium	[omim]
N-Butylpyridinium	[Bupy]
Polyethoxylated Quaternary Ammonium	[Ecoeng500]
Tetrabutylaammonium	[N ₄₄₄₄]
Triethylbutylammonium	[N ₂₂₂₄]
Trihexyl(Tetradecyl)Phosphonium	[P ₆₆₆₁₄]

Table A2. Abbreviations of selected anions in Ionic Liquids

Anion	Abbreviation
Acetate	[CH ₃ COO]
Tetrafluoroborate	[BF ₄]
1-Butyl-3-Methylimidazolium Nitrate	[NO ₃]
Alante	[Ala]
Bis(2-Ethylhexyl)Sulfosuccinate	[Doc]
Bis(Trifluoromethylsulfonyl)Imide	[Tf ₂ N]
Clycinate	[Gly]
Dicyanamide	[DCA]
Ethyl Sulfate	[EtSO ₄]
Isoleucinate	[Ile]
Hexafluorophosphate	[PF ₆]
Leucinate	[Leu]
Methioninate	[Met]
Methyl Sulfate	[Meso4]
Prolinat	[Pro]
Sarcosinate	[Sar]
Trifluoromethanesulfonate	[Tfo]
Tris(Trifluoromethylsulfonyl)Methide	[Methide]
Valinate	[Val]